12-2015

# Spectral Properties of Squaraines and Their Aggregates, Targeted for Use in Bulk Hetero-junction Solar Cells

Chenyu Zheng
cxz9423@rit.edu

# Spectral Properties of Squaraines and Their Aggregates, Targeted for Use in Bulk Hetero-junction Solar Cells

Chenyu Zheng

B.E. Chemical Engineering, Beijing University of Chemical Technology (BUCT), Beijing, China, 2011

A thesis submitted in partial fulfillment of the
requirements for the degree of Master of Science in Chemistry in the
School of Chemistry and Materials Science,
College of Science
Rochester Institute of Technology

December 2015

Signature of the Author Chenyu Zheng

Accepted by Joseph Hornak
Director, M.S. Degree Program Date

SCHOOL OF CHEMISTRY AND MATERIALS SCIENCE

COLLEGE OF SCIENCE
ROCHESTER INSTITUTE OF TECHNOLOGY
ROCHESTER, NEW YORK

CERTIFICATE OF APPROVAL

---

M.S. DEGREE THESIS

---

The M.S. Degree Thesis of Chenyu Zheng has
been examined and approved by the thesis
committee as satisfactory for the thesis required for
the M.S. degree in Chemistry.

_____
Dr. Christopher J. Collison, *Thesis Advisor*

_____
Dr. Thomas W. Smith

_____
Dr. Jeremy A. Cody

_____
Dr. John-David Rocha

_____
Date

# ACKNOWLEDGMENTS

I am using this opportunity to express my sincere gratitude to my advisor Prof. Christopher Collison for his continuous intellectual as well as financial support throughout my master's study and research. You showed me a great patience when I first knocked on your door. The inspiration and enthusiasm you showed me during my research makes me love what I am doing and encouraged me to keep this researching in the future for my PhD.

I also thank Prof. Jeremy Cody, Prof. Thomas Smith and Prof. John-David Rocha for being my committee member and always having an open door for me to discuss my research. You are all very generous with your time and effort in directing me toward the completion of my master's thesis.

Thanks to my group member: Anirudh Raju Penmetcha, Guy Wolfe II, Patrick Cost, James Sinka, Bi Zhu, Victor Mercia, Darina Vassileva, who all kept good works in this research group. I must thank Dr. Susan Spencer, a former PhD student in our group, who during her PhD basically set up the base ground of this research.

I thank my mom Rongping Han and my dad Qi Zheng for their tremendous supports and the spiritual guidance. Your endless love, care and encouragement give me strength that I carry out in very step that I make in my life.

Last but not the least, I thank my wife, simply the most beautiful women that I've ever met, Jingjing Shu. Your love, patience, kindness, and wisdom have warmed my heart and lightened my path. I consider myself to be the luckiest man in the world to meet you, to love you and to marry you.

# ABSTRACT

While Organic photovoltaics (OPV) offer great promise as a low-cost renewable energy source, the relative low efficiency still challenges its commercialization potential. This challenge can be addressed with squaraine (SQ) molecules through unique material design. Advantages of SQ over other materials, such as conjugate polymers, include its high extinction coefficients ($>10^5$), decent photo-stability, good synthetic reproducibility, and tunable molecular structure. The chemical properties of SQ dyes make them very suitable to form two pronounced aggregates in film: H- and J-aggregates. With small chemical modifications, the squaraines can have substantial impact on photophysical properties and aggregation pattern, and thus on operational OPV efficiency. In this work we comprehensively assign the spectral features of two squaraines: a dihydroxy squaraine, 2,4-bis-(4-dibutylamino-2,6-dihydroxyphenyl) cyclobutane-1,3-dione ($DBSQ(OH)_2$) and a corresponding deshydroxy squaraine, 2,4-bis-(4-dibutylamino-phenyl)cyclobutane-1,3-dione (DBSQ) as the squaraines interact with each other in a range of different environments spanning dilute liquid solution with completely isolated molecules, concentrated solid solutions by working with polymethylmethacrylate films, and neat and blended films analogous to active layers for OPV devices. We then verified these assignments with materials characterization and testing of associated OPV devices. In general, the data follows a trend seen for many squaraines synthesized in our group that the presence (absence) of the OH groups. The superior performance of $DBSQ(OH)_2$-based OPV devices suggests the benefit of incorporating OH groups into SQ molecule for OPV application.

# TABLE OF CONTENTS

# TABLE OF FIGURES

# Chapter 1 INTRODUCTION

## 1.1 Organic Photovoltaic Technology

Considering the conflict between the limited quantity of natural fossil fuels and the fast-growing energy consumption rate, the government, public and scientists are now questioning the use of these non-renewables as our main energy sources and looking for sustainable counterparts[1]. Huge attentions are now paid to solar energy, since it represents the largest energy flow on the earth. The energy from the sun is reliable, renewable and enormous, which corresponds to almost 6,000 fold the currently global energy consumption[2]. Thus, it has the potential to become our main energy source in the future.

Since the 1946, when the first practical photovoltaic cell was demonstrated in Bell Laboratories[3], the photovoltaic technology has been developed at an unprecedented rate. For the last two decades, the photovoltaic technologies had an increasing market, having the potential to replace the conventional power generating methods. Nevertheless, the global generation of energy from photovoltaic technology is still small compared to the conventional non-renewable energy sources. The main reason is the relative high cost of conventional solar panels impedes its commercialization by the public. Among numerous photovoltaic technologies, the organic solar cell, with a usage of cheaper organic materials and simple fabrication protocols, represents a new, lost-cost and versatile solar conversion method[4]. The ease of processibility and tunability of the organic materials promise the advantages to increase the power conversion efficiency and lower the manufacturing cost at the same time[5–7].

### 1.1.1 The architecture of organic bulk-heterojunction photovoltaics

Among the other structures, such as bi-layer structure and tandem structure, the bulk-heterojunction (BHJ) structure is popularly studied in OPV research[8]. It provides, at the same time, the sufficient interfacial area for charge separation and effective pathways for electron transfer. This type of device is relatively easy to make and can be processed in solution. The architecture of the BHJ solar cell is in a "sandwich" geometry as depicted in Figure 1.1.

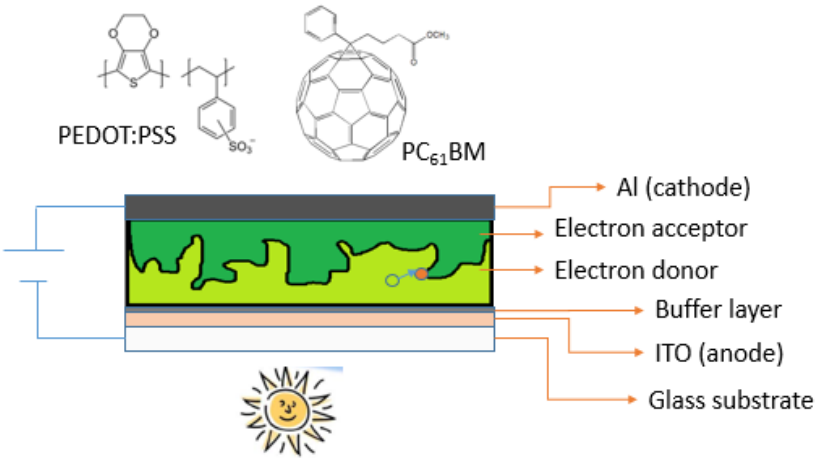


**Figure 0.1** Architecture of BHJ-OPV devices.

The bottom layer is commonly the glass or transparent plastic substrate. On top of the substrate, there is a conducting layer, typically Indium Tin Oxide (ITO), acting as an anode for the solar cell. The transparency of ITO allows the solar radiation to be transmitted to the active layer. A thin film of poly(3,4-ethylenedioxythiophene) polystyrene sulfonate (PEDOT:PSS, top left in Figure 1.1) is a commonly used buffer layer coated on top of the ITO anode. The effect of PEDOT:PSS is to physically smooth the surface of the ITO, to prepare for the deposition of a uniform active layer. The PEDOT:PSS also acts as an electron blocking layer, which therefore promotes a unidirectional transport of specific charge carriers for what thus becomes a diode.

The active layer comprises of a blend of electron donor and acceptor materials. [6,6]-phenyl-C61-butyric acid methyl ester ($PC_{61}BM$ or PCBM, top right in Figure 1.1) is one of the most successful electron accepting materials have ever been applied in organic photovoltaics[8–10]. It was synthesized by Wudl et al by adding the solubilizing butyric methyl ester group to the Buckminsterfullerene $C_{60}$.[11] It can be reduced reversibly with up to six electrons.[12] This strong electron-deficiency imparts an extraordinary ability to stabilize with the uptake of an additional electron. In addition, its solubility in most organic solvents makes it almost the most suitable acceptor material for solution processed organic solar cells. For electron donating materials, polymers, such as poly (3-hexylthiophene-2,5 diyl) (P3HT)[13–15] and poly[N- 9'-heptadecanyl-2,7-carbazole-alt-5,5-(4,7-di-2-thienyl-2,1,3-benzothiadiazole] (PCDTBT),[16,17] are commonly used in conjunction with PCBM. However, compared to their small molecular counterparts such as p-DTS$(FBTTh_2)_2$[6] and squaraine (SQ)[7,18–23], these polymers suffer from difficulties in synthetic and purification procedures.[24] The polydispersity and regioregularity of these semiconducting polymers pose problems to the reproducibility of the solar cell devices based on same materials.[25,26] Small molecules has well defined molecular structures, easy synthesis and purification protocols and excellent semiconducting properties, such as charge carrier mobilities.[27–30] With such awareness, our group intend to develop functional, soluble small molecules as donor candidates in organic solar cells. In particular, we are interested in a family of anilino SQ dyes.

### 1.1.2 Photon-to-electron conversion mechanism in BHJ-OPV devices

The photoinduced charge generation (or photon-to-electron conversion) process in a BHJ-OPV device can be broken down into 5 main steps: 1) absorption; 2) exciton diffusion; 3) exciton dissociation (electron-hole pair separation; 4) charge transport; 5) charge collection.

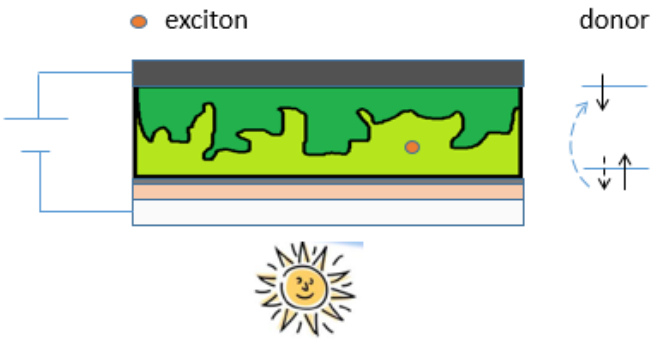


**Figure 0.2** Architecture of BHJ-OPV devices.

The absorption process is the initial step for the photoinduced-charge generation (Figure 1.2). One photon emitted from the sun is absorbed by the electron donor molecule in the active layer. This absorbed energy can excite one electron of the donor molecule from its highest occupied molecular orbital (HOMO) up to the lowest unoccupied molecular orbital (LUMO), as simply depicted in Figure 1.2 (right). This excited molecule, shown as an orange circle in the Figure 1.2, is referred to as an exciton. The exciton is an "umbrella" term that simply means that an electron is bound to the hole left behind in that HOMO without it being confined to a particular molecule. In fact the exciton can extend in space beyond the molecule of origin.

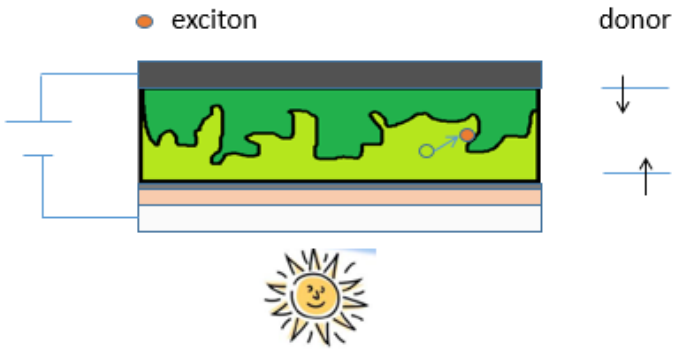


**Figure 0.3** Step 2 – Exciton diffusion.

Once the exciton is generated, it can move a short distance (typically 10 nm[31]) through an energy transfer process. The exciton needs to diffuse to the interface between donor and acceptor in the BHJ active layer, so that subsequent electron hole separation can occur.

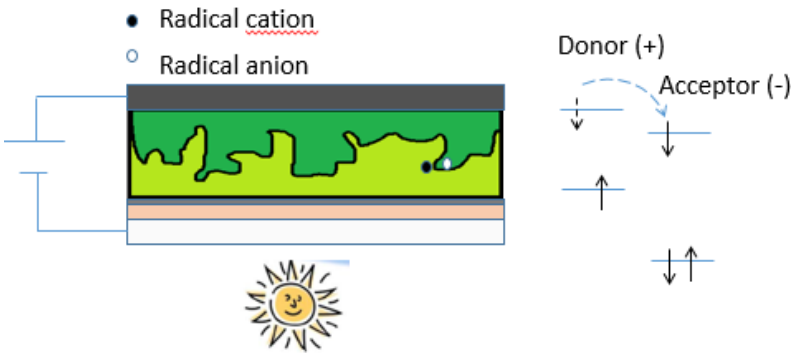


**Figure 0.4** Step 3 – Charge-hole separation.

At that interface, because the LUMO energy level of the acceptor is lower than that of the donor (figure 1.4 right), the electron at the LUMO of the donor is thermodynamically driven to hop over to the acceptor molecule. It is obvious that the electron can hop back from the LUMO of acceptor to HOMO of the donor. However, this is energetically unfavorable due to the large energy offset between these two levels, according to Marcus theory.[32] The energy offset defines the theoretical maximum open-circuit voltage of this OPV device since it represents the driving force for the electrons return to the molecule it came from.

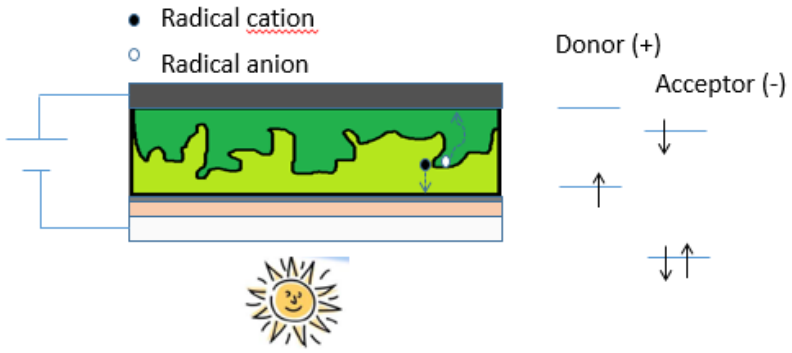


**Figure 0.5** Step 4 and Step 5 – Charge transport and collection.

In the final step, the separated electron and hole will transport through donor and acceptor domains to the respective electrodes and are collected (figure 1.5).

As described above, the main steps of photoinduced-charge generation processes occur within the bulk heterojunction active layer, which consists of donor and acceptor materials. Therefore, the choice of donor materials and the control of the active layer morphology are both crucial to improve the efficiency of the OPV devices.

### 1.1.3 Performance of organic photovoltaic cells

The solar cell technology is designed to convert sun light into electric power. So, the performance of a solar cell is defined as how well the solar cell converts emitted photons into electrons driven through an external circuit. All five main steps of the charge photo-generation process discussed above represent five critical influential factors for solar cell efficiency, expanded mathematically to be:[27]

$$\eta_{OPV} = \eta_{Abs} \cdot \eta_{ED} \cdot \eta_{E-H} \cdot \eta_{CT} \cdot \eta_{CC} \tag{1.1}$$

where $\eta_{OPV}$ is the power conversion efficiency (PCE) of the solar cell, $\eta_{Abs}$, $\eta_{ED}$, $\eta_{E-H}$, $\eta_{CT}$ and $\eta_{CC}$ represent the efficiencies of absorbance, exciton diffusion, electron-hole separation, charge transport and charge collection, respectively.

From an absorbance point of view ($\eta_{Abs}$), the ideal photo-active materials should have both an intense absorptivity and a broad absorption range, which covers the photon flux spectrum of solar radiation as much as possible. The spectrum of photon flux of the solar radiation is shown in Figure 1.6.[5] For organic solar cells, high absorptivity is a particularly important factor for developing efficient photoactive materials. It is because the fact of the low charge carrier mobility in organic semiconductors, as compared to inorganic materials, requires the photovoltaic active layer to be thin, typically less than 200 nm. In order to absorb most of the photons by employing

such a thin film, a high extinction coefficient of $10^4 – 10^5$ $cm^{-1}$ is required for the potential OPV material candidates.

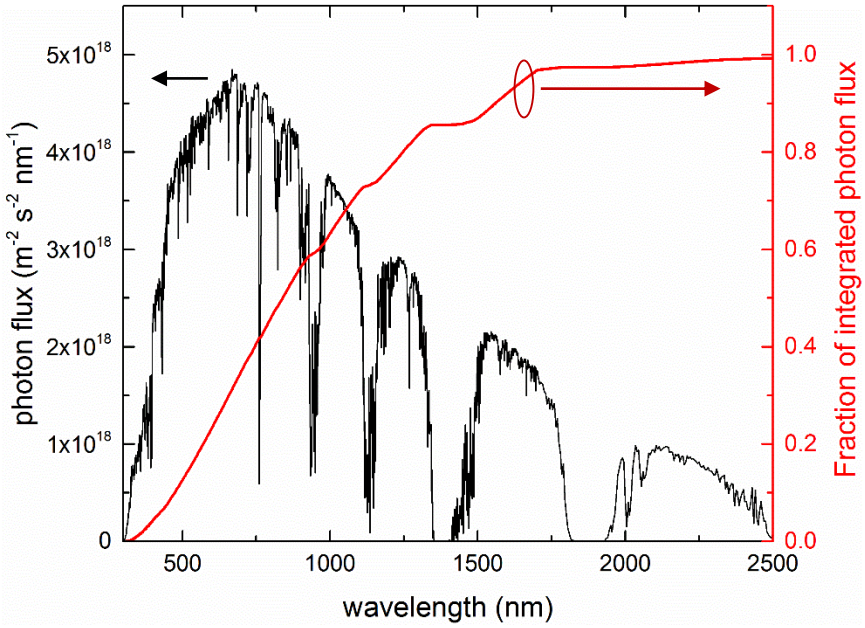


**Figure 0.6** Photon flux of the solar radiation as a function of wavelength (black spectrum), and the integrated photon flux covering from 300nm (red spectrum) where "1" represents all the light that can possibly absorbed over all wavelengths shown.

$\eta_{ED}$, the efficiency of exciton diffusion in the OPV active layer, is considered to be rooted in the Förster Resonance Energy Transfer (FRET) mechanism.[33,34] FRET is a non-radiative energy transfer that interacts through long range dipole-dipole interaction. The strength of this interaction is strongly influenced by the overlapping integral of the absorbance and fluorescence spectrum:

$$R_0 = 9.78 \times 10^2 \left[\frac{\kappa^2 Q_0}{n^4} \int F_D(\lambda)\varepsilon_A(\lambda)\lambda^4 d\lambda\right]^{\frac{1}{6}} \quad (1.2)$$

This equation calculates the Förster radius, which is the intermolecular distance where the FRET has 50% efficiency. κ is the dipole orientation factor, represents the crystallinity of the film morphology; $Q_0$ is the fluorescence quantum yield of donor materials. The integral calculates the spectral overlap between absorption and fluorescence.

The electron-hole separation step ($\eta_{E-H}$) is the true step for photon-to-electron conversion process. In OPV devices, the charge separation is driven by the LUMO-LUMO energy offset between the donor and acceptor materials. Therefore, a large interface area between donor and acceptor domains with an optimal LUMO-LUMO energy offset are beneficial for the electron-hole separation.

In order to compare the performance of organic photovoltaic devices fabricated in different research labs with a variety of materials, two standard testing methods are used in labs. One way to test solar cell efficiency is through the use of a solar simulator -- a device that provides luminescence approximating the sunlight,[5] which enables an indoor test for solar cell devices. Another way to measure the specific spectral response of a solar cell is the external quantum efficiency (EQE) test, also called the spectral response test. EQE is a measurement of the ratio of the amount of current generated from a device to the amount of photons shining on this device per nm:

$$EQE = \frac{number\ of\ electrons\ coming\ out\ from\ devices\ per\ second\ per\ area}{number\ of\ photons\ hitting\ the\ devices\ per\ second\ per\ area} \quad (1.3)$$

A monochromator is used to select photons at a particular wavelength from a given light source to provide incident light, and then the current flow out from the solar cell devices is measured. It is a powerful tool when incorporating the absorbance measurements of the active layer

materials, since it reveals the contribution of each material species on the photon-to-electron conversion efficiency. This is especially important since the aggregates of squaraine dyes in the OPV devices are spectroscopically different from the monomers.

According to the Shockley-Queisser limit, the maximum PCE that single junction solar cells can reach is 33.7%.[35] This limit is commonly used in inorganic photovoltaic research. There are many publications regarding PCE limits for OPV devices,[36–39] but there is still no definite conclusion for the PCE limit because the charge photogeneration mechanism of the OPV is much more complex than that for inorganic PV. For example, it requires an acceptor in order to successfully separate the tightly bound exciton. Currently, the state-of-the-art OPV device by Mitsubishi Chemicals demonstrated a PCE of ~ 11.1%, while the record PCE for thin film crystallized silicon solar cell is ~21.2%.[40]

## 1.2 Photophysics of organic photoactive materials

### 1.2.1 Jablonski diagram

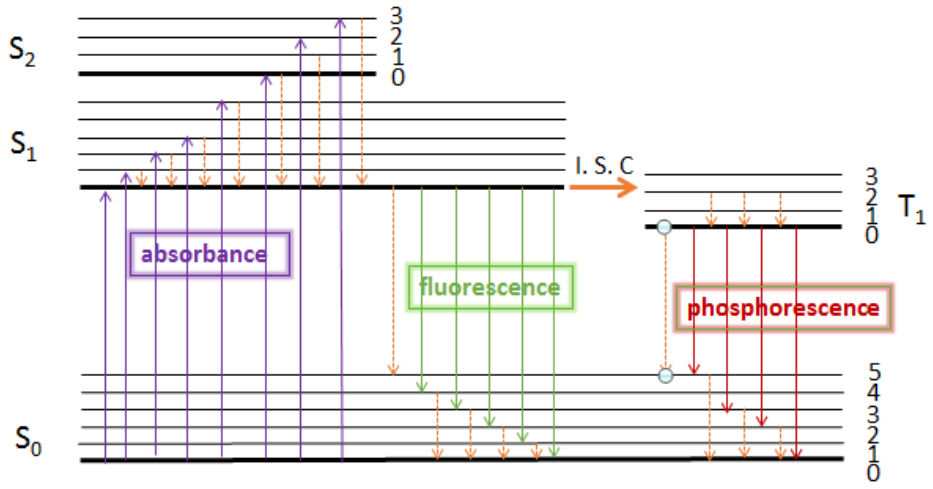


**Figure 0.7** Photophysics of organic molecules illustrated by a Jablonski diagram.

The Jablonski diagram is an energy level diagram denoting the electronic transition in an organic molecule, resulting from an interaction with light (Figure 1.7). Each horizontal line represents the electronic energy level of a molecule, or the eigenstates for the electrons in a molecule. The bold horizontal lines are denoted as the vibrational ground states for each electronic state: ground state ($S_0$), first excited singlet state ($S_1$), second excited singlet state ($S_2$) and first excited triplet state ($T_1$). The lines between each electronic state are the multiple vibronic energy levels (denoted as 0, 1, 2…). Nevertheless, there are enormous numbers of vibrational levels within the electronic states, only a portion of them are presented in the Jablonski diagram. These vibrational levels always have higher energy than their corresponding electronic states because these vibrations exist on top of a particular electronic distribution associated with a set of bonds for the molecule in that electronic state. Each vibrational level can be further divided into massive numbers of rotational sub-energy-levels. However, a typical Jablonski diagram and photophysical study would omit such intense levels of details.

a. Absorbance

The first transition in the Jablonski diagram is absorbance, which is represented by the arrows pointing up in Figure 1.7. Absorbance is an electron transition from lower ground states to higher excited energy levels (exciton) by the interaction of the electrons with photons. Because of the discontinuity of the energy levels, only certain wavelengths of photons that have energies that correspond to the energy difference between two eigenstates can be absorbed. The probability of each transition is proportional to the electronic eigenstates coupling (Fermi's Golden Rule).[41]

b. Vibrational relaxation and internal conversion

Once excited into a vibrational level of the excited state (i.e. v=2, $S_1$), the electrons can relax very quickly to its vibrationless excited states (v=0, $S_1$). This relaxation is indicated by a

dashed arrow in the Jablonski diagram and called vibrational relaxation. Since it is very fast (often in $10^{-14}$~$10^{-11}$ s),[42] it is extremely likely to occur immediately after absorbance. Therefore, the dominant excited states of a molecule are generally referred to the vibrationless excites states. The vibrational relaxation is a non-radiative decay; the energy has been dissipated in a form of heat or transferred to adjacent molecules.

After the molecule (electron) has relaxed to its vibrationless excited state, another non-radiative pathway for electron transition can occur – internal conversion. It happens if the vibrational levels of a lower energy state strongly overlap and couple with the vibrationless excited states. After the electron is transferred to one of the vibrational levels of the ground energy state, it quickly decays to the ground state $S_0$ through vibrational relaxation.

c. Fluorescence

After an excited electron has relaxed to its first excited state ($S_1$), it can decay to the ground sate ($S_0$) by emitting a photon. This radiative decay pathway is called fluorescence, and is denoted by arrows pointing straight down. Nevertheless it is a reverse pathway to absorbance; the emitted photon typically has less energy than the absorbed photon, because of the loss of energy during the vibrational relaxation. Fluorescence is an important property of organic molecules, since it provides us a way to monitor the molecular excited states.

d. Intersystem crossing and phosphorescence

The electron can transfer from one excited state (i.e. first singlet excited state) to a parallel excited state (i.e. first triplet excited state) through intersystem crossing, another horizontal transition. It leads to phosphorescence, which is several magnitudes slower than fluorescence because the change in electron spin multiplicity upon relaxing to the singlet ground state makes the transition quantum mechanically forbidden. After the electron intersystem crosses to an excited

vibrational level of the first triplet state, it quickly goes through vibrational relaxation to the vibrationless energy level. Then, it can radiatively decay from the excited triplet state to the singlet ground state by emitting a photon; the slow process is called phosphorescence. This electron can also back transfer from the triplet-excited state to singlet-excited state if it can be thermally excited, leading to emission of a photon through "delayed" fluorescence.

### 1.2.2 Photophysics of materials in OPV

Photophysical properties are extremely important for understanding the functionality of materials in OPV devices. As shown above, power conversion processes in OPV can be subdivided into 5 main steps. The final device efficiency is determined by multiplying the individual efficiencies of those 5 steps. If any step yields a low efficiency, the final power conversion efficiency (PCE) will suffer. Therefore, the photophysical properties of photo-active materials, such as absorbance, exciton diffusion rate or exciton dissociation rate at the heterojunction-interface, are all crucial to judge the performance of these materials in OPV devices. In this study, our goal is to develop a connection between molecular structure and photophysical properties, and a connection between photophysical properties and device performance, thus helping us to design better functional squaraine dye molecules for OPV application.

Absorbance is very important, since it represents how efficiently the photo-active materials are interacting with light. The more photons that are absorbed, the more excited states (excitons) will be generated. In order to absorb as many photons as possible, the materials should have high molar absorptivity and a panchromatic absorption spectrum that matches well with the solar irradiation spectrum.

Fluorescence quantum yield (QY) is also a valuable photophysical indicator. The fluorescence QY value is the ratio of "number of photons emitted" to "number of photons absorbed". It

indicates how susceptible the excited states are to fast non-radiative decay mechanisms versus radiative decay mechanisms. Coupled with fluorescence lifetime data it can tell us how long-lived a particular excited state is. In relation to device operation, if a large population of excited states is quickly dissipated through internal conversion, it is unlikely for the excitons to diffuse to the interface and dissociate into charges and holes. Thus, a low quantum yield may be indicative of a low device efficiency.

Fluorescence lifetime is an important parameter of the kinetics associated with organic molecular excited states. Time correlated single photon counting techniques allow the measure of the lifetime of an excited state before it decays to the ground state through fluorescence and other pathways. The longer the excited state lifetime, the longer the distance that the excitons can possibly travel through the material bulk to the interface.

The exciton diffusion length ($L_D$) is defined as the distance that an exciton can travel before it decays back to the ground state. If the diffusion length is short, it means that the exciton won't be able to travel a long distance and successfully reach the heterojunction-interface. $L_D$ depends on excited state lifetime (or fluorescence lifetime) and the exciton diffusion rate (FRET), which depends on the morphology of the material bulk. It is considered that excitons can travel further in a crystalline domain than an amorphous domain in the material bulk, because the dipole orientation factor, $\kappa$ (Equation 1.2), is large in a highly ordered crystal, and is small in a randomly oriented material.

In summary, the desired material properties for OPV application include: broad absorption spectrum, large extinction coefficient, high fluorescence quantum yield, long fluorescence lifetime, and strong ability to crystallize. We should also note that the photophysical properties of the material in the solid state are very different from those in solution, due to a stronger inter-molecular interaction in the solid state. Other than that, the properties are also going to change as the material starts to crystallize.[43] For example, it has been reported that the band gap (i.e. HOMO-

LUMO energy gap) will decrease as the P3HT polymer starts to crystallize. This crystallization of the material is typically obtained by annealing treatments (such as thermal annealing or solvent annealing).[44–46] In this work, we will study the crystallization of squaraine molecules in thin film (i.e. aggregation), and the property changes due to this crystallization.

## 1.3 Squaraine dyes

Squaraine (SQ) dye molecules are π conjugated organic chromophores synthesized based on the squaric acid.[47–49] SQ dyes are particularly interesting due to their unique non-linear spectral response and intense absorption and fluorescence in the red region of the spectrum.[50] Recently, SQs have been greatly investigated as potential donor materials in organic photovoltaic applications,[7,18–23] since they are considered to have higher functionalities exceeding commonly used polymers. They possess strong light harvesting abilities and their photoactivity, to visible and near-Infrared light (600 nm – 850 nm), matches well with the solar irradiation spectrum (Figure 1.6). Other advantages of using SQs in OPV include: excellent photo- and thermal-stability enabling long operation lifetime of the OPV devices;[51] they are relatively easy to synthesize and purify, offering low-cost for large scale manufacturing;[47] ability to aggregate into crystalline and semi-crystalline domains, favoring exciton diffusion and charge transport.[44,46]

There are two types of SQs separated by symmetry. Symmetric SQs have the same structure of donor moieties on both sides of a central four-membered ring acceptor. While asymmetric SQ have two different donor groups, resulting in a directional electron transfer from the donor to the ring acceptor moiety. Asymmetric SQs are synthesized for their directional chemical binding property, which can improve structural order of the active layer in a dye-sensitized solar cell (DSSC).[7,52–55] The asymmetric SQs typically have larger band gap (i.e. blue-shifted absorption) and higher radiationless decay rate (i.e. lower quantum yield and short excited state lifetime) as compared to the symmetric SQs with similar structure. In this work, symmetrical squaraines are

of particular interest because they typically have a longer excited state lifetime and the directionality of the charge transfer in bulk heterojunction (BHJ) is not as important as DSSC.[56]

The symmetric SQs that were investigated in this study are two aniline-based SQs with n-butyl chains on the molecular arm. DBSQ refers to di-butyl SQ with no hydroxyl substituent on the aniline (or des-hydroxy SQ); $DBSQ(OH)_2$ refers to the same butyl groups on two sides with di-hydroxyl substituents on the aniline (Figure 1.8).

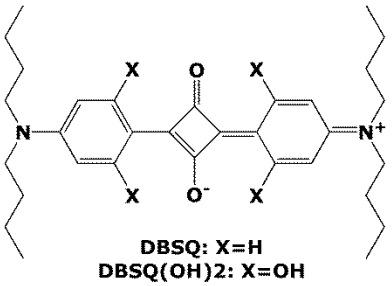


**Figure 0.8** Molecular structure of DBSQ and $DBSQ(OH)_2$.

We intended to compare the spectroscopic results of these two SQs in solutions and in solid states to uncover the influence of the OH electron-releasing groups on absorption, fluorescence and aggregation properties of the aniline SQ molecules. We also compare the OPV efficiency of devices made from these two materials.

### 1.3.1 Charge transfer character

Charge transfer (CT) character refers to the strong intermolecular or intramolecular electronic interaction between an electron donor and an electron acceptor.[57] For large molecules with electron donor and acceptor moieties linked with a π conjugated bridge, charges can be resonant in this entire molecule through the π conjugation. This charge resonance is considered responsible

for the low excitation energy with large transition dipole moment. Therefore, molecules with intramolecular CT characters would generally have a high extinction coefficient and their absorbance typically falls in the visible or near-infrared region in the spectrum.[56]

The structure of the SQ shows a D-A-D (donor-acceptor-donor) structure, the central squarylium ring houses two carbonyls which are electron poor while two aniline systems on opposite sides are electron rich. The charge resonance between electron-donor and –acceptor moieties determines that the zwitterionic states exist in both ground and excited states of the SQ dye molecules. The zwitterionic states of SQ molecules thus refer to the electron transfer to the oxygen molecules on the squarylium ring (figure 1.7). It implies an electron rearrangement, resulting in changes in the bond order and molecular geometry.

Painelli and coworkers have successfully quantified the quadrupolar characters (or zwitterionic characters) in the electronic states of squaraine dyes by using an essential state model.[58,59] They concluded that the quadrupolar characters exist in both ground and excited states of squaraine-based dyes. In particular, the ground state has remarkable high quadrupolar characters compared to other types of dyes.[59] Their conclusion supports our hypothesis that the CT is significant in squaraine molecules and this charge delocalization is expected to benefit the OPV devices in which the charge mobility strongly affect the device performance.[13,20,37]

### 1.3.2 Influence of hydroxyl groups and side chains

For $DBSQ(OH)_2$, the four hydroxyl groups attached on an aromatic ring is in close proximity to the oxygen atoms on the squarylium ring (figure 1.7), suggesting a probability of forming intramolecular hydrogen bonds (H-bonds). The intramolecular H-bond is likely to increase the planarity and thus the conjugation of the squaraine molecule, and therefore a red shift in absorption of $DBSQ(OH)_2$ compared to DBSQ is expected. In addition, a higher fluorescence quantum yield would be expected for di-hydroxyl SQs due to their more rigid planar structure (with fewer

intramolecular vibrational and rotational motions, compared to des-hydroxy SQs) allowing more excited electrons to relax through fluorescence instead of vibrational relaxation. In this study, SQs were investigated and compared to each other in chloroform solutions. Their photophysical properties, including absorbance, fluorescence, fluorescence quantum yield and fluorescence life-time were characterized and used in this comparison.

Side chains attached to the nitrogen atom located on each molecular arm also affect the molecular packing; i.e. longer or branched chains will favor a longer intermolecular distance. However, the effect of side chains on CT features of SQ molecules remains a controversy. Longer alkyl chains on two sides are regarded as electron donating groups to the π conjugated phenol or benzyl rings, while increasing the electron density of the donor groups in the SQ molecules.[56] The donor groups with higher electron density are able to further stabilize the intramolecular CT states or charge resonance, leading to lower excitation energy or red-shifted absorbance. On the other hand, given that the N-alkyl group is far away from the squarylium ring, the correlation between the length of side groups and absorbance shifts would not likely provide a clear trend. Again, it should be noted that the N-alkyl chain is not a conjugated system; the electron delocalization character of these saturated carbon chains is negligible. In summary, we assume that the N-alkyl molecular arms only influence the molecular packing in the solid state, while having little impact on the electronic character of the squaraine molecule. The side chain will not be a compared parameter in this work, given that the two SQs investigated here have same molecular side chain.

By this study, we hope to get a general idea of how hydroxyl groups affect the electronic transitions and excited states of the SQ molecules. This correlation of photophysics to molecular structure will provide guidance for a better material design for OPV or other potential applications.

## 1.4 Squaraine aggregation

In dye chemistry, self-association of dyes in the solid state is a common phenomenon that results from the high intermolecular Van der Waals-like attractive forces. The aggregation generally causes a distinct absorption change due to the shifting of aggregate bands away from the monomeric bands.[60–62] Various aggregation interactions lead to two different spectral changes: aggregates with a bathochromic (red) shift are defined as J-aggregates; while aggregates with a hypsochromic (blue) shift are considered H-aggregates. Although the bathochromic shift and the hypsochromic shift are often informally referred to as "red-shift" and "blue-shift" in the literature, it has no relation to Doppler shift or other pure physical or optical shifts. The electronic states in H- and J-aggregates have been explained by exciton theory.[60]

### 1.4.1 Exciton theory

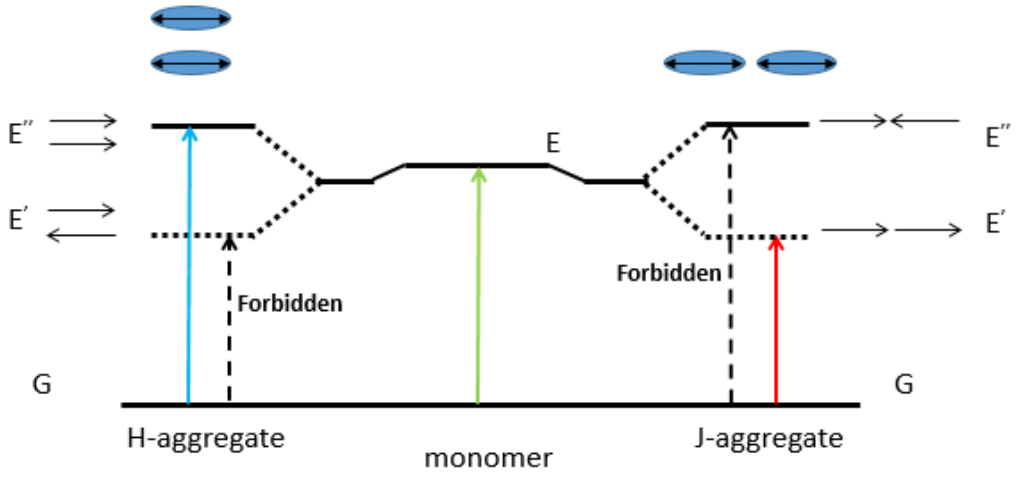


**Figure 0.9** A schematic diagram of the energy level of aggregates and monomer.

In exciton theory, the dye molecule is regarded as a point dipole, and the electronic states split into two levels due to the interaction of dipoles. The molecules aggregate with a face-to-face (or plane-to-plane) packing to form H-aggregates, or with a head-to-tail structure to form J-aggre-

gates (as depicted in Figure 1.8). In the case of a face-to-face dimer (or H-aggregate), a lower energy is associated with the oppositely oriented dipoles, while the parallel dipoles has a higher energy due to the electrostatic force felt by the adjacent dipoles. It is the opposite case for a head-to-tail dimer (or J-aggregate). Transitions from ground state to excited state are only allowed if the sum of the dipoles is not zero. As a result, the electronic transition from ground states to upper excited states (E'') in H-aggregates is allowed, but to lower excited states (E') is forbidden. It is the opposite case for J-aggregates. The transitions to the upper level in H-aggregates typically require higher energy than in its monomeric form, thus leading to a "blue-shift" in its absorbance. The transition with lower excitation energy in J-aggregates would cause a corresponding "red-shift" in the absorbance.

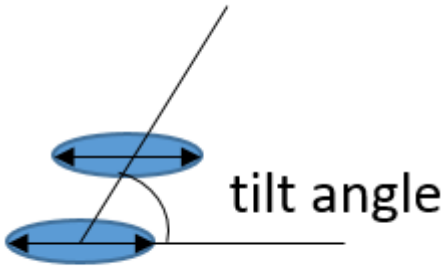


**Figure 0.10** The tilt angle in a dimer.

This energy level splitting is the main reason for the absorbance broadening of SQ in the solid state compared to in solutions. Dimer structures of both H- and J-packing are drawn in the top of Figure 1.8. The angle between the line crossing the molecular centers and the long axis of one of the molecules is called "tilt angle", as shown in figure 1.9. According to Emerson et al, the spectral shift is a function of the tilt angle at a constant molecular center separation.[63] When tilt angle is equal to 90$^{o}$, the spectrum exhibits a large hypsochromic shift and the H-aggregate is formed; when the tilt angle approaches 0$^{o}$, the spectrum exhibits a large bathochromic shift as it

forms the J-aggregate. In the real world, the tilt angles are distributed in over certain range rather than being exactly the same. Therefore, the absorbance of aggregates is broadened over a certain range in the spectrum instead of just a peak shift.

Aggregation is an extremely important property of SQ dyes. Not only does it change the energy levels, electronic transition dipole moments and other photophysical and electronic properties, but it also is linked to and is a function of the morphology of the active layer in the OPV devices that governs the exciton diffusion, dissociation and charge transport in the semi-crystalline domains. The formation of aggregates in organic photovoltaic films induces changes in all the device performances: open-circuit voltage, short-circuit current and fill factor, and thus the overall device efficiency.

### 1.4.2 Influence of hydroxyl groups and side chains on aggregation

The aggregation is determined by packing geometry, which is strongly influenced by molecular structure. Therefore, we believe that the side chains and hydroxyl groups will strongly affect the aggregation properties of the SQs. It is known in the literature that SQ aggregation strongly affects the OPV device performance.[18,22,64] It is vital to fundamentally understand the relationship between molecular structure and aggregation patterns in the solid state.

Side chains affect the molecular packing by inducing the steric hindrance. In principle, the side chains may induce strong steric hindrance between two planar SQ molecular backbones, and therefore impede the aggregation. This can be understood straightforwardly with branched side chains. However, for linear chains, there is a tradeoff between London dispersion forces (attraction force) and the steric hindrance (repulsion force) induced by the side chains. A previous study has found that the sublimation ability of the SQ molecules increased and then decreased with increasing the length of the linear alkyl side chains, reaching a maximum with propyl N-al-

kyl side groups.[65] The sublimation ability depends on the intermolecular forces between SQ molecules in the solid state. The results are consistent with the explanation that the steric hindrance dominates the intermolecular force when the number of carbons in the side chain is smaller than three; while the attraction force (London dispersion force) dominates when the SQ have longer side chains.

Hydroxyl groups enable the intramolecular H-bond, and thus enhance the planarity and the π-conjugation of the molecular backbone. The intramolecular H-bonds act to "lock" the benzene ring at the same plane as the squarylium, and thus enhance the aromatic-aromatic interaction (i.e. π-π stacking) between two molecules in the aggregate. Therefore, we hypothesize that the $DBSQ(OH)_2$, which possesses four hydroxyl groups are more prone to form a well-defined aggregate structure than DBSQ, the des-hydroxy SQ.

# Chapter 2 EXPERIMENTAL METHODS

## 2.1 Material preparation

SQs were synthesized in Dr. Jeremy Cody's research group at Department of Chemistry and Material Science, the products were certified using $^{1}H$ NMR and $^{13}C$ NMR. SQs were used as received in the Collison group and thus the synthesizing process will not be discussed in detail here. Phenyl-C61-butyric acid methyl ester (PCBM) was purchased from American Dye Source Inc. (catalog number ADS61BFA) and used as received. Reagent grade solvents (chloroform and dimethyl sulfoxide) were used as purchased from Sigma Aldrich without further purification. Deionized water is obtained from a Barnstead E-Pure Ultrapure Water Purification System.

The squaraine and PCBM materials were kept in a $N_2$-filled MBraun glove box with $O_2 \leq$ 50ppm and $H_2O \leq 0.1$ppm. All solutions were prepared in pre-cleaned 20 mL scintillation vials. The vial was parafilmed after chloroform was added to prevent evaporation, which might results in concentration change. Sonication (in VWR bath sonicator-model 750) was applied for all SQ stock solutions and active layer solutions (SQ+PCBM) in order to fully dissolve all materials.

The films were spin coated from SQ stock solution or active layer solution by using a Chemat spin coater (model KW-4A) at a spin speed of 800 RPM. The detailed procedures can be found in appendix-A. VWR microscope slides were used as substrates for absorbance measurements. ITO coated glass substrates were used as substrates for device making.

## 2.2 Photoluminescence quantum yield

The photoluminescence quantum yield (PLQY) was measured on a HORIBA FluoroMax fluorometer with a Quanta-φ integrating sphere (Figure 2.1). In a HORIBA FluoroMax fluorometer, the light is provided by a xenon source, and then focused on the entrance slit of the excitation monochromator with an elliptical mirror. After the excitation monochromator, the light is then incident on the entrance of the integration sphere. A detailed introduction of the instrument and procedures of measurement can be found in the "A Guide to Recording Fluorescence Quantum Yields".[66]

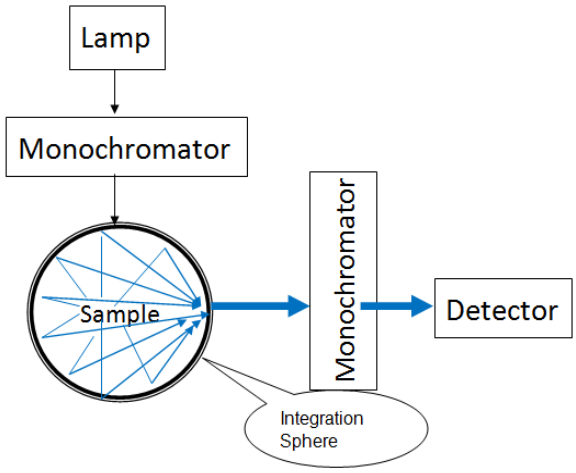


**Figure 0.1** Instrumental set up for PLQY measurement.

In the integration sphere, the light that is not absorbed by the sample and fluorescent light will all be reflected to the detector. By controlling the emission monochromator, we can selectively scan either incident light or fluorescent light. The signal from the detector is then conveyed to a computer linked to the HORIBA FluoroMax fluorometer, and then different scan spectra are obtained for the PLQY measurement. The data was then pasted into a "PLQY calculator" spreadsheet, and the basic calculation is illustrated below.

The PLQY is the ratio of "number of photons emitted" to "number of photons absorbed". The number of photons absorbed is calculated by monitoring the scattered light intensity– firstly with a blank, and secondly with the sample solution in the sphere. The difference in peak intensity between these two measurements is caused by squaraine's absorption. The number of emitted photons is calculated from the acquired emission spectrum. The formula of quantum yield calculation is:

$$\Phi_F = \frac{E_C - E_A}{L_A - L_C} \tag{2.1}$$

$E_C$=fluorescence of sample in the sphere

$E_A$=fluorescence of blank in the sphere

$L_A$=scatter of blank in the sphere

$L_C$=scatter of sample in the sphere

## 2.3 Fluorescence lifetime

The fluorescence lifetime was measured on a Time Correlated Single Photon Counting (TCSPC) system (Figure 2.2). A detailed introduction of TCSPC can be found in the "Time-Correlated Single Photon Counting" manual.[67]

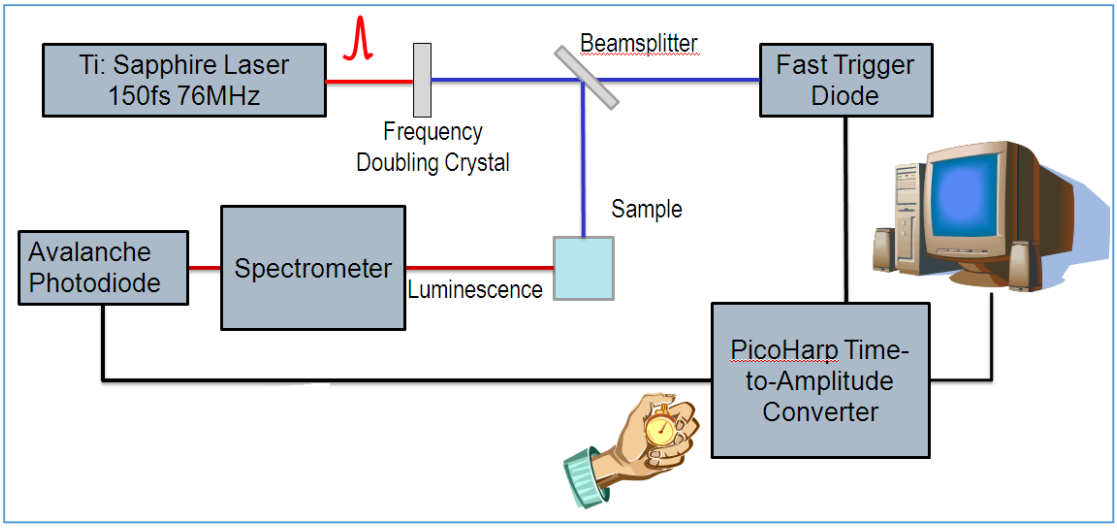


**Figure 0.2** A schematic diagram for TCSPC instrumental set up.

In the TCSPC system, a femtosecond pulsed laser beam is provided by a Newport Ti:Sapphire laser at a frequency of 76 MHz (150 fs per pulse of laser beam). This pumps an optical parametric oscillator (OPO) that allows the pump beam to be tuned to the target wavelength between 620-640nm. Before exciting the sample, the pulsed incident laser is split into two beams. One beam goes to a Fast Trigger Diode to initiate the Picoharp 300 picosecond timer, while the other goes to the sample. The Picoharp 300 timer is an ultrafast stopwatch with resolution of 4 pico-seconds. As soon as the fluorescent photon is detected by an Avalanche Photodiode, the Picoharp timer immediately stops the counting and records the start-stop-time as illustrated in Figure 2.3. A spectrometer is placed in between the Avalanche Photodiode and sample. This spectrometer is acting as a monochromator to filter the fluorescent light, which allows selection of the emission wavelength.

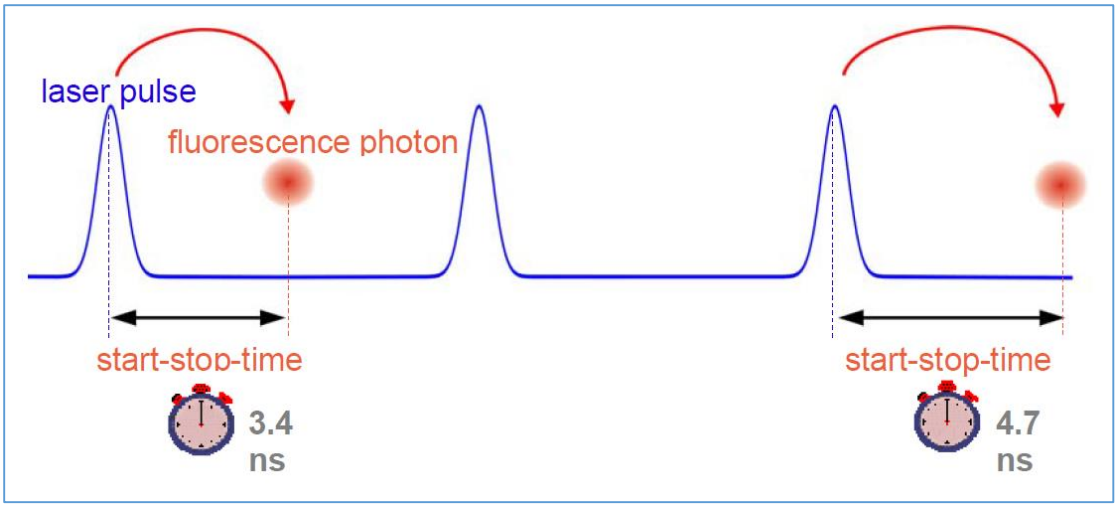


**Figure 0.3** A schematic diagram for Picoharp 300 picosecond timing system.

## 2.4 External quantum efficiency

The external quantum efficiency (EQE) is defined by the equation below:

$$EQE = \frac{\#\ of\ electrons\ generated\ from\ devices\ per\ wavelength\ per\ area}{\#\ of\ photons\ hitting\ the\ devices\ per\ wavelength\ per\ area} \quad (2.2)$$

The detailed introduction for this technique can be found in ref [68]. Experimentally, the OPV device is activated by shining light upon it at a specific wavelength, and the current was extracted from the electrodes of the device. Then the current is converted to number of electrons per second by dividing by the electric charge ($1.602\times10^{-19}$ coulombs per electron). The number of photons can be calculated by using the power of incident light and the associated energy of photons at that wavelength (i.e. $hc/\lambda$). The ratio of electrons to photons is known as the EQE value at that wavelength. So the desired EQE is 1, over as broad a wavelength range as possible. For example, when "EQE equals to 1 at 600nm", this means that every incident photon (at 600nm) on the device will be absorbed by the material to generate excitons, then all these excitons will successfully diffuse to the heterojunction-interface and undergo charge dissociation and finally all the dissociated free carriers will be collected, without loss, by the electrodes of the devices. It is obvious that the EQE

is never going to be unity due to multiple losses during charge photo-generation. Typically, the EQE spectrum will mimic the absorption spectra of donor and acceptor blends.[5,16,33]

The EQE was measured using spectral response based on an Optronic Laboratories 750 spectroradiometric system (Figure 2.4).

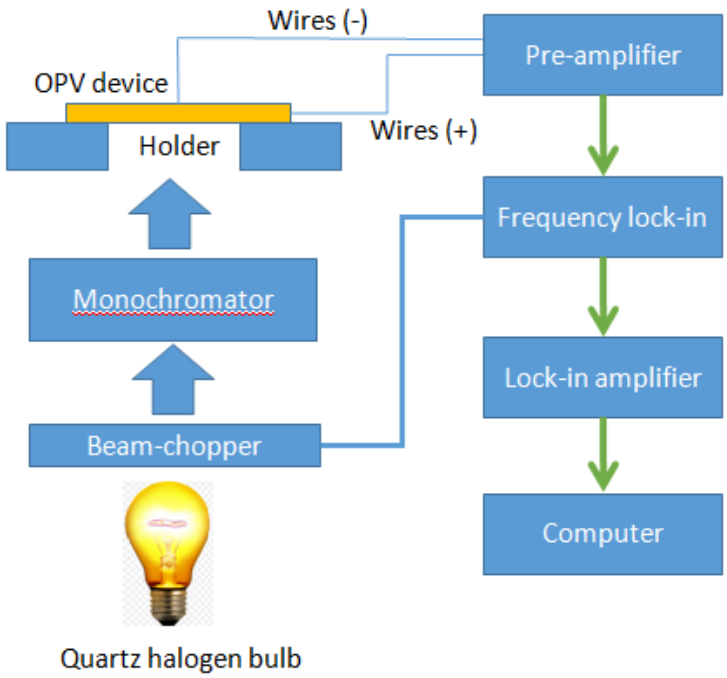


**Figure 0.4** A schematic diagram for Laboratories 750 Spectral Response set up.

In the Laboratories 750 spectral response system, the incident light is produced by a quartz halogen bulb (~94W). The light is filtered by a beam chopper, whose frequency is corresponding to the frequency lock-in, and then passes through a monochromator to select its wavelength. The pulsed incident light at specific frequency and at specific wavelength was then used to excite the OPV devices. Due to the special sandwich structure of OPV devices (Figure 1.1), the device must be placed with the aluminum side pointing up when testing it. So, the incident light must be shining through the bottom of the device. The device was placed on a plastic holder with a hole in the center where the light passes without any loss or attenuation. The out-flow current (photo-generated current of the OPV device) was measured with two probes attached on each

electrode; the probes were connected to a pre-amplifier set-up. The signal generated from the pre-amplifier was converted from current (I) to volts (V), and then conveyed to the frequency lock-in, whose frequency is set according to the beam chopper. It is a "phase-sensitive detection" technique that the amplifier only responds to the signals which oscillate at the same frequency as the reference input.[68] This allows the instrument to accurately select the target signal that would otherwise be overwhelmed by the noise, therefore significantly increase the S/N ratio. The signal coming out from the lock-in amplifier is then recorded by the computer and analyzed to get the spectral response of the devices.

The EQE spectrum gives information on the spectral response of the OPV devices. This spectral response is directly related to material absorption. In other words, the device only responds to the light that the photoactive material can absorb. Therefore, it is extremely useful to characterize the photophysical properties of the materials, such as aggregation, since the squaraine aggregates absorb differently compared to the squaraine monomer (the absorption spectra will be provided and discussed in chapter 3 and chapter 4). By combining the EQE and the absorption spectrum, we can confirm the formation of squaraine aggregates in the film and evaluate the functionalities of these aggregates compared to the squaraine monomer or other donor states.

## 2.5 J-V measurement

The current density-voltage measurement (J-V measurement) is the basic characterization method for photovoltaic device. It yields three evaluating metrics for OPV devices: open-circuit voltage ($V_{OC}$), short-circuit current ($J_{SC}$), and fill factor (FF).

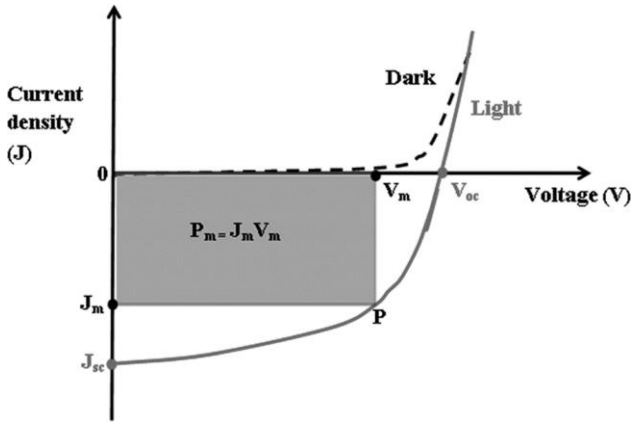


**Figure 0.5** J-V curve of a typical photovoltaic device.

The J-V curve can be viewed as the diode curve[69] shifted downwards (to negative current) as shown in Figure 2.5. The $V_{OC}$ is the voltage of the solar cell when the device is at the open-circuit condition (infinite resistance and thus maximum voltage). The $J_{SC}$ is the current density when there is no out bias applied to the device (and hence zero resistance). If we consider the solar cell as a battery, the $V_{OC}$ is the maximum operation voltage and $J_{SC}$ is maximum current that we can obtain for the load(s) in the circuit. But we should note that the current density under $V_{OC}$ condition and the voltage under $J_{SC}$ condition are both 0, and the output power per area equals voltage multiplied by current density; thus the output power is actually 0 at these two extreme conditions. The maximum output power is denoted as the dark region, $P_m = J_m \times V_m$. The FF is the factor that links the maximum output power and the $V_{OC}$ and $J_{SC}$:

$$FF = \frac{P_m}{V_{OC} \times J_{SC}} \tag{2.3}$$

While the overall power conversion efficiency (PCE) can be calculated as:

$$PCE = \frac{V_{OC} J_{SC} FF}{P_{IN}} = \frac{P_m}{P_{IN}} \tag{2.4}$$

where the $P_{IN}$ is the power of incident light. PCE is the universal parameter to judge the performance of a solar cell, and widely used in research.

The J-V curve of the OPV device is obtained by using a Newport 91159 Full Spectrum solar simulator with a power density of 100 mW/cm$^2$. The xenon lamp in the solar simulator is calibrated with a round-robin InGaAs photovoltaic cell fabricated at NASA. The standard InGaAs photovoltaic cell was certified by NASA before the shipment. The SQ based OPV devices are tested immediately after fabrication to eliminate cell deterioration due to the material degradation, which is a contributing factor towards inaccurate measurements given that the cells are not encapsulated and the testing of the devices must be operated in ambient conditions.

The devices were measured by using a 4-point probe technique with a Keithley 2400 Sourcemeter. The probes are brought into light contact with the two electrodes (ITO as the anode and aluminum as the cathode). It should be noted that too deep a probe-contact can penetrate and short-circuit the device. The data were collected and analyzed using an internally-developed LabView program. The film is placed in the same location on the testing surface every time in an effort to minimize errors.

# Chapter 3 PHOTOPHYSICAL PROPERTIES OF SQUARAINES IN SOLUTIONS

## 3.1 Introduction

The photophysical properties of DBSQ and $DBSQ(OH)_2$ are characterized by steady-state and time-resolved spectroscopic methodologies. The SQ molecule is considered completely dissolved in the chloroform solution without any interaction between other SQs. Therefore, the photophysical properties, i.e. excited state dynamics and lifetimes, are considered to belong to the individual SQ molecule or monomer. These photophysical properties are regarded part of a standard characterization for the SQ molecule to compare with SQ in thin films and in OPV devices.

## 3.2 Experiments

**Chloroform solution**. The solution sample was prepared in a 20 mL pre-cleaned glass scintillation vial. A stock solution was first made and sonicated for 5 minutes in a VWR bath sonicator (model 750) at power level 9, and then diluted to different concentrations ($\leq 1\times10^{5}$ mol $L^{-1}$). Once the solutions were prepared, they were tightly capped and sealed with parafilm to prevent solvent evaporation.

**Absorbance spectra**. The absorption measurements of SQs in chloroform solutions were taken using a Shimadzu UV-2100PC spectrophotometer. The instrument was set to scan from 900 nm to 300 nm. A medium scan speed, 0.5 nm increments and 2 nm slit width were applied when taking the measurements. A "control" solution, which only contained pure chloroform solvent, was first scanned to baseline the spectrum to account for the light scattering of the solvent and the cuvette.

**Fluorescence**. The fluorescence emission and excitation measurements of SQs in chloroform solutions were taken using a HORIBA FluoroMax fluorometer. The sample with least concentration ($1\times10^{6}$ mol $L^{-1}$) was used for fluorescence measurement to rule out the inner filter effect.[70,71]

A quartz cuvette (type 23/Q/10) with a path length of 1 cm was used for determining absorbance and fluorescence spectra of each SQ in chloroform solution. The cuvette was cleaned using the solvent when each solution measurement was finished, and was dried using nitrogen gas.

**Photoluminescence Quantum Yield**. The photoluminescence quantum yield (PLQY) was measured in the HORIBA FluoroMax fluorometer by using a Quanta-φ integrating sphere. The data are recorded directly into the FluorESSENCE software, and the quantum yield calculation is accomplished by "PLQY calculator" spreadsheet. To prevent saturation of the PMT detector it is necessary to use ND filter when measuring $L_A$ and $L_C$, which scans through the very intense scattered excitation peaks.

When taking an emission scan, the excitation wavelength is set to $\lambda_{EX}$ = (absorbance maximum – 30 nm). The emission of the sample was scanned by a detector from ($\lambda_{EX}$ + 4 nm) to 800 nm. When taking an excitation scan, the detector was set to $\lambda_{EM}$ = (absorbance maximum + 30 nm), and the incident light was scanned from 450 nm to ($\lambda_{EM}$ – 4 nm). Both excitation and emission slit widths were set to 1 nm.

The sample prepared for quantum yield measurement was the most dilute solution for $DBSQ(OH)_2$ and DBSQ ($1\times10^{-6}$ mol/L).

**Fluorescence lifetime**. The fluorescence lifetime was measured using a time-correlated single photon counting (TCSPC) system. A femtosecond (fs) pulsed laser beam is provided by a

Newport Ti:Sapphire laser at a frequency of 76 MHz (150 fs per pulse of laser beam). The chloroform solutions of SQs was made at the concentration of 0.188 μg $mL^{-1}$ (=$3.4\times10^{-7}$ mol/L), which has the optical density below 0.1, to rule out the inner filter effect on lifetime measurements. The excitation wavelength were varied with an optical parametric amplifier system and are listed with the associated data.

## 3.3 Results and discussion

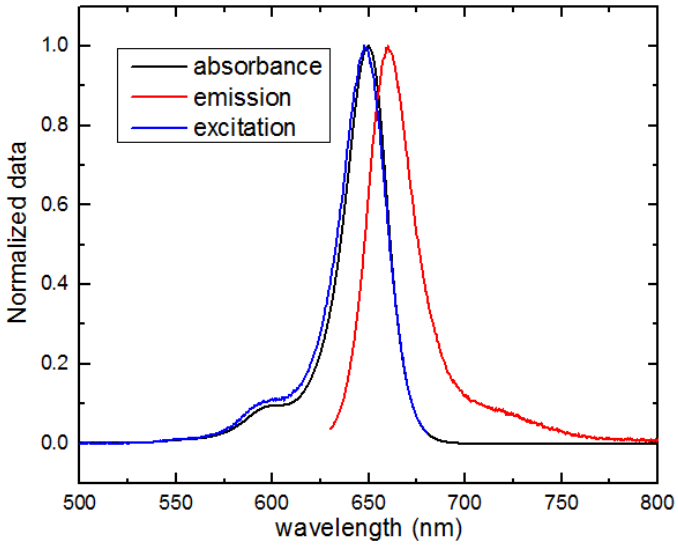


**Figure 0.1** Absorbance, fluorescence emission and excitation spectra of DBSQ(OH)2 in chloroform solution ($1\times10^{-6}$ mol/L).

The absorption, fluorescence emission and fluorescence excitation spectra of $DBSQ(OH)_2$ in dilute chloroform solution are presented in Figure 3.1. $DBSQ(OH)_2$ has an absorbance peak at 650 nm and an emission maximum at 660 nm in chloroform solution. The extinction coefficient at 650 nm is equal to $(2.97 \pm 0.15) \times 10^5$ L $mol^{-1}$ $cm^{-1}$. An identifiable absorption shoulder appears at ~590 nm, blue-shifted from the main peak. The Stokes' shift between absorption and fluorescence maximum is 10 nm. The detailed data are summarized in table 3.1.

The pleasing match of fluorescence excitation spectra and absorption spectra indicates that there is only one fluorophore species in the chloroform solution, which is believed to be SQ monomer. This also tells that the fluorescence quantum yield is constant over the range of absorption.

Another distinct spectral character of this SQ is the absorption shoulder (or vibronic progression) in the blue edge of the absorption band (~590nm). The main absorption peak at 650 nm is considered as the 0-0 transition from the ground state to excited state. The excitation is dominated by 0-0 transition, and the vibronic progression peak is relatively weak.

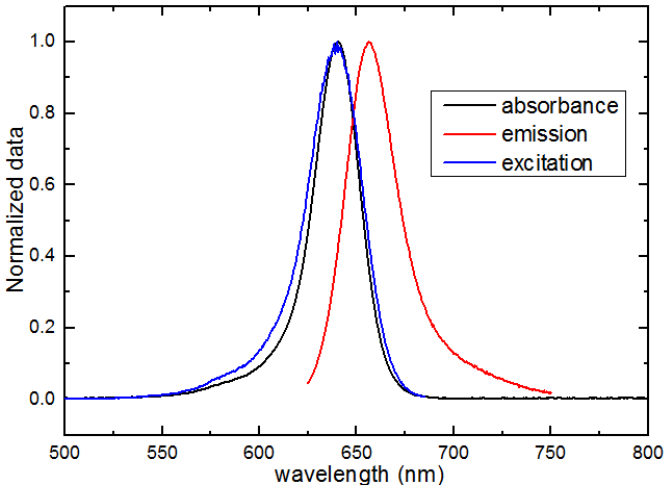


**Figure 0.2** Normalized absorbance, fluorescence emission and excitation spectra of DBSQ in chloroform solution (1×106 M).

The normalized absorption, fluorescence emission and excitation spectra of DBSQ in dilute chloroform solution are shown in Figure 3.2. The absorbance peak is at 640 nm, while the fluorescence emission peak is at 656 nm. Thus, the Stokes' shift is 15 nm. The extinction coefficient of DBSQ in chloroform solution is $(2.27 \pm 0.11) \times 10^5$ L mol$^{-1}$ cm$^{-1}$. The absorbance shoulder can hardly be distinguished. Similar to DBSQ(OH)$_2$, the fluorescence excitation matches well with the absorption spectrum, indicating it is the SQ monomer absorbing and emitting the light.

On the other hand, it is different from $DBSQ(OH)_2$ in that the absorbance shoulder is almost disappeared in the spectrum.

This shoulder peak is associated with the vibrations which couples to the electronic transition (i.e. vibronic coupling), given that its peak position shifts 0.16 eV from the main peak, consistent with the energy of the typical vinyl stretching mode.[61,62,72] Thus, the prominent shoulder peak in $DBSQ(OH)_2$ solution spectra suggests a strong vibronic coupling in the dihydroxy SQ, which is related to the planar structure locked by the intramolecular H-bonds.

**Table 0.1** Summary of absorption and fluorescence data for $DBSQ(OH)_2$ and DBSQ in dilute chloroform solution.

| Squaraine | Absorbance $\lambda_{max}$ (nm) | $\varepsilon_{max}$ ($M^{-1}\cdot cm^{-1}$) | emission $\lambda_{max}$ (nm) | Fluorescence Quantum yield |
|---|---|---|---|---|
| $DBSQ(OH)_2$ | 650 ± 0.5 | $(2.97 \pm 0.15) \times 10^5$ | 660 ± 0.5 | 0.845 ± 0.1 |
| DBSQ | 641 ± 0.5 | $(2.27 \pm 0.11) \times 10^5$ | 656 ± 0.5 | 0.822 ± 0.1 |

The spectral data of $DBSQ(OH)_2$ and DBSQ in chloroform solution were summarized in table 3.1. The comparison of the data between these two squaraine will yield the effect of di-hydroxyl groups on the molecular photophysical properties.

The absorption maximum of $DBSQ(OH)_2$ is red shifted by 9 nm compared to the DBSQ. This is consistent with the hypothesis that the π-conjugation is enhanced by the intermolecular H-bonds.[35,36] The higher extinction coefficient of $DBSQ(OH)_2$ indicates the OH-group increases the coupling between ground and excited state (CT state) of the SQ molecule. This increasing in coupling is also illustrated by the higher PLQY and the smaller Stokes' shift of $DBSQ(OH)_2$ than DBSQ.

The higher PLQY of $DBSQ(OH)_2$ is attributed to the high planarity and rigidity of this SQ due to the intramolecular H-bond between OH groups and C−O in the central squarylium

ring. The high planarity of the molecule restricts the molecular vibration and thus reduces the non-radiative relaxation, increasing the PL.

## 3.3 Summary

In a comparison, $DBSQ(OH)_2$ exhibits a higher PLQY, red-shifted absorbance and higher extinction coefficient than DBSQ in chloroform. These properties are beneficial for OPV. The higher PLQY of $DBSQ(OH)_2$ indicates that the excitons generated from excitation tend to fluoresce ($k_r$) rather than relax non-radiatively ($k_{nr}$):

$$\Phi_F = \frac{k_r}{k_r + k_{nr}} \tag{3.1}$$

$\Phi_F$ represents the PLQY, $k_r$ is the radiative decay (i.e. fluorescence) rate, $k_{nr}$ is the non-radiative decay rate. When ∅ is high, it implies the $k_{nr}$ is small. The non-radiative decay will reduce the lifetime of the excited states.[70] A longer excited state lifetime will extend the exciton diffusion length with the assumption that the exciton diffusion rate is the same for all SQ materials. Any limitation on non-radiative coupling between the excited state and ground state will aid in terms of the exciton diffusion length. In OPV devices, this is very critical for the exciton transport and exciton dissociation steps introduced in chapter 1.1.

In addition, the extinction coefficient of $DBSQ(OH)_2$ is higher than that of DBSQ, which means that di-hydroxyl $DBSQ(OH)_2$ can absorb more photons than des-hydroxy DBSQ.

However, these photophysical properties are characterized in chloroform solution, while the bulk-heterojunction OPV devices are made from materials spin coated as thin films (different from the liquid dye-sensitized solar cell). We also know that the properties of SQs in solid state are far different from in solutions, due to aggregation. Thus, characterizing the properties of SQ thin films is also critical to realize their potential for application in OPV.

# Chapter 4 ABSORBANCE OF SQUARAINES IN NEAT AND BLEND FILMS

## 4.1 Introduction

In OPV devices, the SQs are blended with PCBM as thin films, so it is necessary and crucial to study the photophysical properties of those same solid states. The morphology of these films determines the extent and type of aggregation of the SQs in the solid state. The aggregation is an interesting and important property of SQs, which not only dramatically changes the photophysical properties but is also a reflection of the morphology of the active layer. The OPV active layer morphology (i.e. the morphology of the blended films) and the material energy levels affect the exciton diffusion and exciton dissociation in the device. The SQ excited state is that state from which the free charges originate. Therefore, it is valuable to understand the excited states of these molecules and aggregates in the solid state.

In the former solution study, there is no evidence of SQ aggregation in the chloroform solution, an expected result since individual SQ molecules would be surrounded by solvent molecules. In the solid state, the SQs aggregate very readily after spin casting from solution. By studying neat SQ films and blended films with PCBM, we hope to assign the absorbance features to J- and H-aggregates, and monomers. We hope to interpret spectral changes in terms of any disruption of aggregate structure forced through the presence of the PCBM.

The blended film is also made by spin coating from chloroform solution. As chloroform quickly evaporates, the materials are precipitated from the solution, and then are “frozen” in the solid state. The SQs and PCBM are completely dissolved in the chloroform solution before soni-

cation. Due to the fast spin coating process (~1-2 seconds before chloroform completely evaporated), the entropy of the system will dominate the processes, and favors the mixing of SQs and PCBM. However, due to the surface energy difference of SQ and PCBM, the mixing of SQs and PCBM is not in thermal equilibrium. By providing thermal energy (for example, applying thermal annealing), the SQ and PCBM tend to aggregate into pure phases and domains, leading to a phase separation. Significant intermixing of SQ and PCBM leads to a large heterojunction-interface that would favor exciton dissociation. On the other hand, the phase separation of SQ and PCBM is beneficial for longer exciton diffusion lengths and more effective charge transport, if we consider that phase separation implies improved crystallinity and furthermore improves the wavefunction overlap between adjacent molecules.

In this chapter, we will see a total disruption of aggregation induced by PCBM, and a recovery of aggregation by the thermal annealing treatment of the blended films. Therefore, we think annealing will encourage the SQ aggregate formation in the solid neat films and induce phase separation between SQ and PCBM in the solid blend films. As will be shown in this chapter, the absorption spectra of pristine SQ-PCBM blend films are significantly different to those spectra of neat films for each SQ. The absorption spectrum can thus be used to monitor the interaction between SQ and PCBM. Upon annealing, the change in packing geometry of SQ and PCBM leads to a significant change in the spectral properties of the blend films. By tracing the absorption spectra change, one can thus infer the molecular packing changes during this thermal annealing process (such as whether SQ tends to form an aggregate or mix with PCBM). More importantly, one can successfully control the relative population of aggregates and monomers of each SQ in the thin films based on the interpretation of the absorption changes during thermal annealing. This is extremely helpful for understanding how each SQ species (H-aggregate, J-aggregate and monomer) contributes in the OPV devices. It also allows an assessment of control over the morphology of the SQ blends so that device efficiency might ultimately be improved.

## 4.2 Experiments

**Thin films**. ITO coated glass substrates were cleaned, respectively, in ultrasonic baths of acetone and isopropyl alcohol for 30 minutes. The PEDOT:PSS solution was diluted and filtered to remove any unwanted polymer agglomerates, before being spin cast onto the cleaned substrates at a spin speed of 5,000 RPM. Chloroform solutions of SQs at 8 mg $mL^{-1}$ concentration were made and sonicated for 10 minutes, as well as the SQ:PCBM solutions (the concentration of SQ was also 8 mg $mL^{-1}$, SQ:PCBM = 1:1, w/w). The SQ thin films were made by spin-coating the SQ or the SQ:PCBM solution onto PEDOT:PSS coated ITO glass substrates at a 800 RPM spin speed. The final layer structure of the films was: SQ(or SQ:PCBM)/PEDOT:PSS/ITO/Glass. Here in this chapter, the pure SQ film is called neat film, while the SQ:PCBM film is called blended film.

Three films were made for each SQ or SQ:PCBM blend. All of them were used for absorption characterization. After the absorption measurements, a thermal annealing approach was applied to these three films for each squaraine (SQ:PCBM blend) under different temperatures: 80 $^0$C, 120 $^0$C and 150 $^0$C, one film per temperature. The thermal annealing process was conducted using a VWR Professional Hot Plate (model number 97042-730) under nitrogen atmosphere to prevent materials degradation caused by ambient water and $O_2$.

**Absorbance**. A Shimadzu UV-2401 spectrophotometer was used for absorption characterization. Medium scan speed, 0.5 nm increments and 2 nm slit width were applied when taking the measurements. A blank with PEDOT:PSS coated ITO glass was used to baseline the spectrum to account for scattering and absorption of substrates. Three measurements were taken for each film by changing the film position in the light path to account for any heterogeneity in the films.

## 4.3 Results and discussion

### 4.3.1 Neat film absorbance

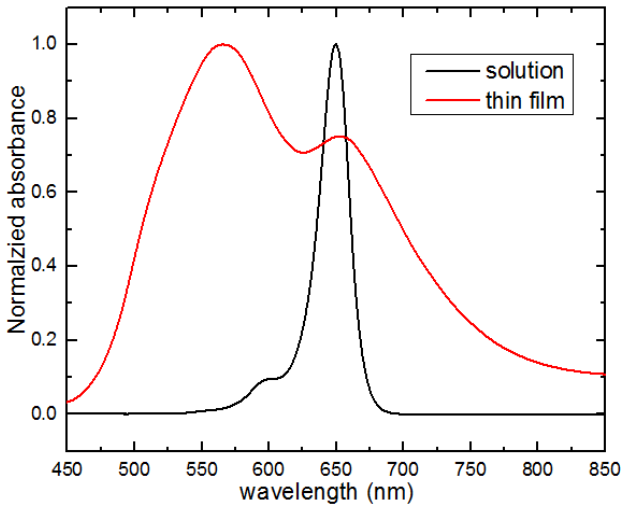


**Figure 0.1** Normalized UV-Vis absorption spectra of DBSQ(OH)2 in dilute solution and as a thin film (solid) spin coated from solution.

Figure 4.1 shows the absorption spectrum of $DBSQ(OH)_2$ in dilute chloroform solution ($\leq 1\times10^{5}$ M) and as a thin film spin-coated from chloroform solution (SQ concentration is 8 mg $mL^{-1}$). A sharp and intense peak of the chloroform solution is found at 650 nm. There are two absorbing peaks in the thin film spectrum: a higher peak at 565 nm (2.19 eV) and a lower one at 652 nm (1.90 eV).

The major peak at 565 nm is assigned to H-aggregate absorption, since it is blue shifted 85 nm (0.29 eV) from the chloroform solution absorption peak (i.e. monomer peak) at 650 nm. The peak at 652 nm is generally considered to be the monomer absorption[42], given that the peak position is very close to that of the chloroform solution at 650 nm. But we should notice that this peak is a lot broader than the solution absorption peak. On the other hand, another explanation would be to assign this peak as the Davydov splitting peak of $DBSQ(OH)_2$ aggregate, given that its aggregation structure may be "herringbone," which typically leads to both H- and J-character

(Figure 4-3). With intermolecular interactions of a thin film, it is possible that, along with the dipole-dipole coupling that would lead to J-aggregation or Davydov splitting, there may also be an intermolecular charge transfer contribution, although we will later describe how this is unlikely for a vertically stacked H-aggregate. With further data presented in this paper, we hope to conclude with universal assignments for these materials that are consistent for all environments. For example we can consider how much the ratio of optical density at 565 nm to that at 652 nm changes. If this ratio does not change then in fact it would be likely that these two peaks come from the same species, and thus Davydov splitting will be the most reasonable explanation.

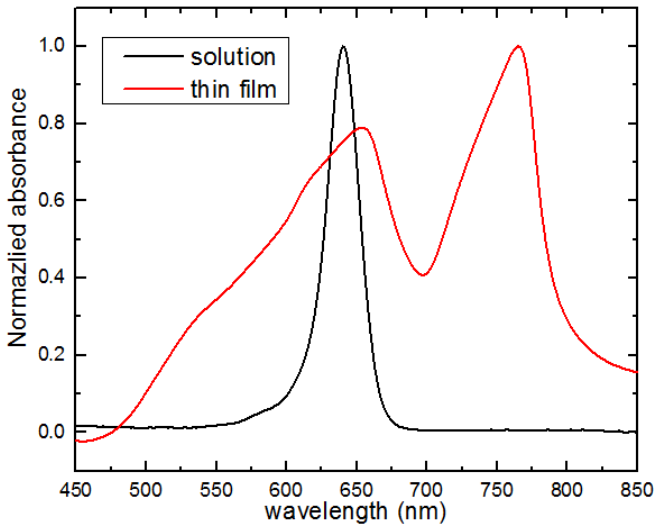


**Figure 0.2** Normalized UV-Vis absorption spectra of DBSQ in dilute solution and as a thin film (solid) spin coated from chloroform solution.

The absorption spectra of DBSQ in dilute chloroform solution and as a thin film are shown in Figure 4.2. The neat film also has two peaks (black spectrum): one broad peak at 653 nm (1.902 eV), one narrow peak at 765 nm (1.6235 eV). Both peaks are broad and unsymmetrical, because of what looks like a progression of vibronic structure. Progression one represents peaks at 653 nm (1.902 eV) with shoulders at 610 nm (2.036 eV) and 540 nm (2.300 eV) with separations of 0.134 eV and 0.264 eV respectively. It may be that another shoulder in between

these two shoulders exists (2.170 eV or 572 nm) given that the separations of the first two observed shoulders are 1×0.134 eV and 3×0.134 eV from the primary peak. Progression two represents the peak at 765 nm (1.6235) eV and a second feature at 730 nm (1.70 eV) separated by 0.0765 eV.

The low-energy peak at 765 nm is tentatively interpreted to be the J-aggregate absorbance, which is red-shifted 125 nm from the absorption peak of chloroform solution. The assignment of the 653 nm peak is unclear – there is a strong vibrational character, which does not exist in solution and, coupled with a very small gas to crystal shift (0.009 eV), an assignment to a monomer transition is therefore unlikely. It too may originate from an intermolecular interaction, excitonic or H-aggregate in nature.

The peak broadening and peak "asymmetry" may also be interpreted to be originated from a small amount of H-aggregate-structures formed during the spin coating, as evidenced by the absorption shoulder at 540nm (blue-shifted 100nm from the absorption of chloroform solution). But we consider that the H-aggregate formation is not the sole reason for the broadening. Here, we use a herringbone aggregate description to explain the "monomer" absorbance in DBSQ and $DBSQ(OH)_2$ neat films.

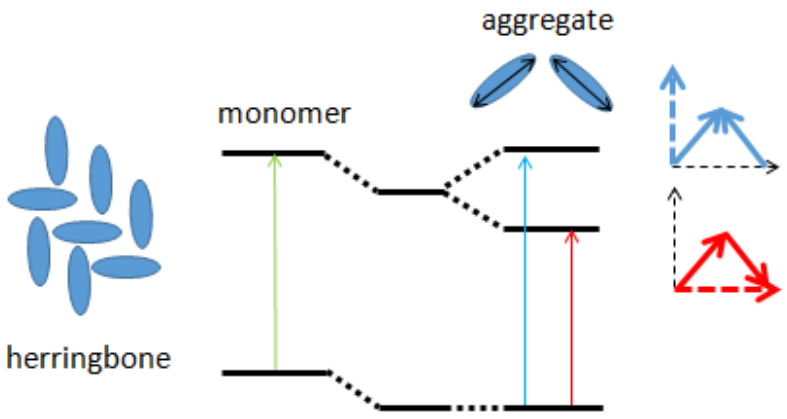


**Figure 0.3** Schematic herringbone structure and two allowed excited states transition of herringbone aggregate.

Figure 4.3 shows the herringbone structure proposed for $DBSQ(OH)_2$ and DBSQ aggregates. In herringbone packing, the transition dipole moment as shown in Figure 4.3 indicates both vertical (H-aggregate character) and horizontal (J-aggregate character). This herringbone packing structure allows the excitation from the HOMO ground state to both H-excited and J-excited states. Therefore, in the absorption spectrum, there are two peaks in the films, which are known as Davydov splitting peaks. Due to the different angle between the two dipoles, the H- or J-transition will be correspondingly dominant in the excitation process, leading to different relative absorption intensities. For example, a transition from the ground state to the H-excited state might be favored in $DBSQ(OH)_2$ neat films because the relative dipole angle is small, and the packing tends more towards a face-to-face geometry.

Let's then address the broadening of the absorption peak in films compared to solution. We know that there are three causes of line broadening in absorption spectra: Doppler broadening, natural broadening and collisonal broadening. The natural broadening is all spectral broadening caused by the Heisenberg uncertainty principle, and thus cannot be reduced or eliminated. But it is very important to note that the magnitude of this broadening is very small. Collisonal broadening results from atoms or molecules that are absorbing light colliding into one another. Energy from the collisions is coupled to the transition energy. It is not likely happened in thin film, but it can happen in solution. The Doppler broadening is caused by vibrations induced by small molecular or atomic thermal motion towards or away from the beam. For molecules, the situation is different from atoms, in that both the atoms composing the molecule experience thermal vibrations, as well as the molecule itself. In UV-Vis absorbance, Doppler broadening is the main source of broadening and sets the limit of resolution. When we move from one molecule to an aggregate, the thermal vibrations become very complicated as far more intermolecular forces appear in the aggregate than in the individual molecule, such as intermolecular vibrations, intermolecular

charge transfer, etc. All these forces will be impacted by intermolecular distance and relative dipole orientations of the SQ molecule in solid state. Therefore the Doppler broadening will increase significantly as the system becomes chaotic.

In comparing the absorption spectra between the DBSQ film and the $DBSQ(OH)_2$ film, we clearly see that $DBSQ(OH)_2$ forms predominately the H-aggregate in the film, while DBSQ forms a J-aggregate. This can be explained in that the enhanced planarity of the $DBSQ(OH)_2$ increases the $\pi$ stacking of the molecular backbone, and thus favors face-to-face packing in the solid state. Without H-bonds, the steric hindrance induced by alkyl molecular arms is large, leading to a head-to-tail packing. In addition, the irregular absorption spectrum of DBSQ indicates the aggregation formation is less confined to one species, so that both absorption signatures of H- and J-aggregates can be identified in the spectrum. We think that this presence of both H- and J-aggregates is due to DBSQ lacking a strong intermolecular interactions. It should be stated here that these interpretations represent a hypothesis that will be confirmed or rejected by future XRD and single crystal structure studies in this group.

In order to verify the herringbone aggregate hypothesis, annealing was conducted for each SQ neat film. Thermal annealing favors the aggregate, a thermodynamically stable state, forming in the neat films. If any peaks are from monomer absorption, then we expect to see a decrease in those peaks (even a disappearance) and an increase in the contribution of aggregate peaks after annealing.

### 4.3.2 Neat film absorbance upon annealing

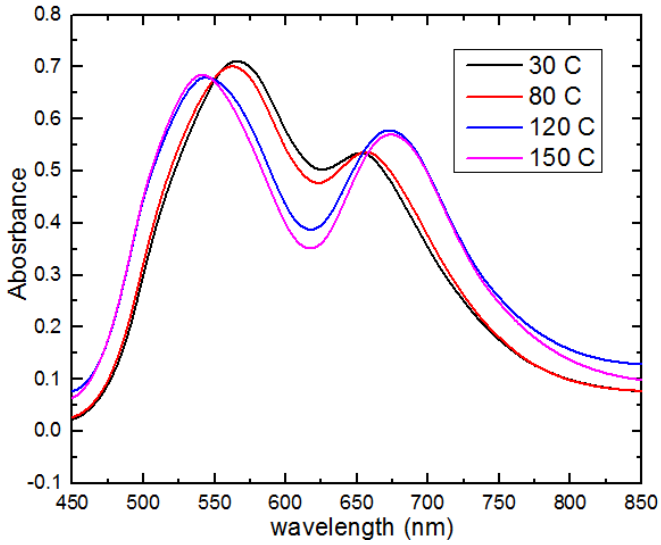


**Figure 0.4** UV-Vis absorption spectra of DBSQ(OH)2 neat thin films before and after annealing.

The absorption spectra of $DBSQ(OH)_2$ thin films under different annealing temperatures are shown in Figure 4.4. As stated previously, the pristine (30 $^0$C-spectra in Figure 4-4) film has two absorption peaks at 565 nm and 652 nm. Upon annealing, two peaks become more separate and there is a decrease in absorbance at 620 nm. After 150 $^0$C annealing, both peaks shift ~23 nm from 565 nm to 541 nm and from 652 nm to 674 nm. In addition, the higher-energy peak decreases by about 4% in intensity while the lower-energy peak increases by about 7%, for the same film after annealing.

The further splitting and shifting of the peak suggests that a more orderly packing is obtained upon annealing. In the event that the interplanar spacing of the molecules decreases, we would see a larger Davydov splitting. If the peak assigned to the monomer represents the amorphous domain, we would expect this peak to decrease after annealing. However, the absorption peak at 652 nm increases from an optical density of 0.75 to 0.83 instead, indicating this peak does not belong to SQ monomer excitation. In addition, this peak also red shifts to 674 nm, suggesting it is a Davydov splitting peak.

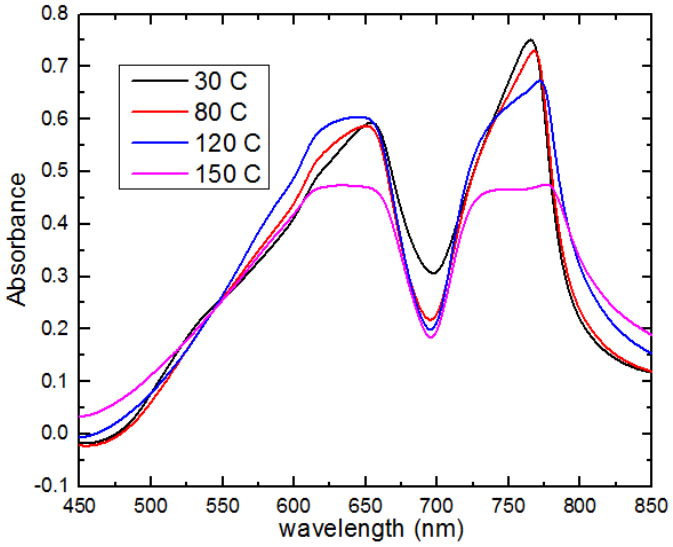


**Figure 0.5** UV-Vis absorption spectra of DBSQ neat thin films before and after annealing.

The raw absorption spectra of the DBSQ neat film before and after annealing are shown in Figure 4.5. It is noted that the two "sharp-top" peaks turned into "flat-top" peaks under the 120 $^0$C anneal. The absorption in the trough at ~700 nm decreases immediately upon annealing. The peak at 765 nm from the pristine film (30 $^0$C) is slightly red-shifted to 776 nm in the 150 $^0$C-annealed films. Compare to the 120 $^0$C-annealed films, there is an absorption decrease for both peaks in the 150 $^0$C-annealed films.

The absorption spectra of the annealed films verifies the sub-absorption band hypothesis (the composite absorption of the unannealed films are made of multiple sub peaks). Upon annealing, the 610 nm sub-band of the higher-energy peak and the 730 nm sub-band of the lower-energy peak is populated. These populated sub-bands result in a "flattening" of absorption peaks. The absorption decrease from 120 $^0$C-annealed films to 150 $^0$C-annealed films is perhaps due to the degradation of the material, since this SQ is known to have poor stability. The spectra are inconsistent with the the peak at 653 nm being associated with the monomer peak. The reason is that we expected the monomer to be depopulated through annealing, but the absorption intensity at 653 nm remains as the same.

When comparing DBSQ and DBSQ(OH)2 films upon annealing, we should note one similar phenomenon: the two main peaks for each SQ film further split apart. This peak shifting suggests a decreased intermolecular distance. Interestingly, there is no relative peak height change during the annealing process, indicating that no significant H- or J-aggregate change takes place during annealing. Aggregate formation is nearly completed after spin coating we infer. We also notice that the "monomer" peak in the solid state retains the same intensity after annealing, which supports the herringbone aggregate hypothesis. Therefore, we cannot hastily assign this peak to monomer absorbance. Further investigation is necessary in order to visualize the "real" monomer absorption peak in the solid state.

On the other hand, we notice that the absorption spectra of annealed des-hydroxy DBSQ films are highly unsymmetrical, indicating multi-types of aggregation. This is interpreted to be that the molecular packing is less confined without strong intermolecular force. Therefore, multiple aggregate structures appear in the DBSQ neat film, leading to different absorption bands appears in the films.

### 4.3.3 Blend film absorbance upon annealing

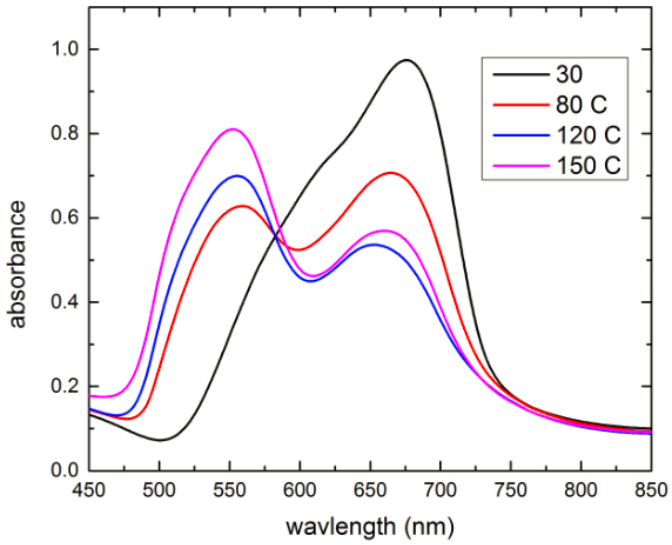


**Figure 0.6** UV-Vis absorption spectra of DBSQ(OH)2:PCBM blend films before and after annealing.

The absorption spectra of $DBSQ(OH)_2$:PCBM blend thin films (1:1 w/w, spin coated from chloroform solution) are shown in Figure 4.6. The pristine blend film has the absorption maxima at 676 nm and a shoulder at ~620 nm. After annealing, the absorption decreases at the absorption maxima, and a peak grows at ~540 nm.

These new absorption peaks growing in at ~540 nm for annealed films are close to the absorption peak of the H-aggregate in neat films, and thus are assigned to the H-aggregate of $DBSQ(OH)_2$. There is very little absorption of H-aggregates in the pristine blend film, but a high absorbance at 650-700 nm, suggests that the PCBM almost totally disrupts the H-aggregation of SQ. This disruption is caused by the substantial mixing of PCBM bulky-balls and SQs in the film. Thereafter, the peak of pristine film at 676 nm is attributed to the SQ monomer absorption. However, this absorbance peak has red-shifted ~26 nm and is much broader when compared to the absorption peak in the chloroform solution.

H-aggregates are continuously generated during annealing, as can be monitored by spectra changes. The increasing (decreasing) absorption at 540 nm (676 nm), along with an isosbestic point at ~583 nm, illustrate a transition from disrupted molecules to ordered H-aggregates during annealing. This also suggests a phase separation between SQ and PCBM in the solid blend.

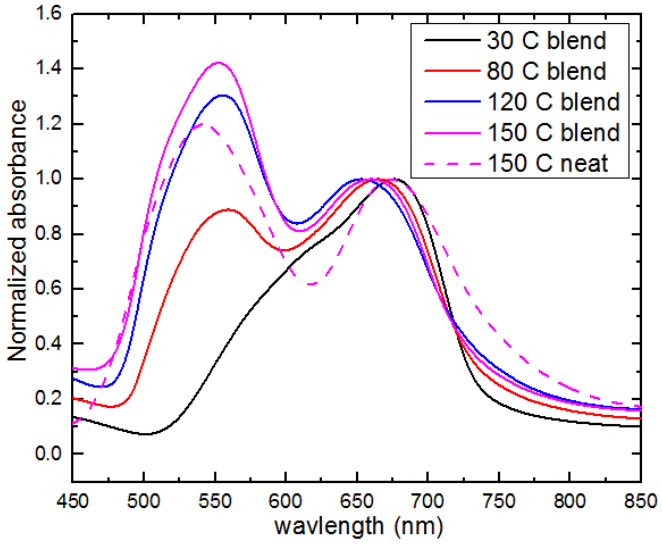


**Figure 0.7** Solid line: UV-Vis absorption spectra of DBSQ(OH)2:PCBM blend films normalized to the absorption maxima in 600nm-850nm; pink dashed line: UV-Vis absorption of DBSQ(OH)2 neat 150 0C-annealed film.

The absorption spectra of $DBSQ(OH)_2$:PCBM annealed blend film are normalized to their lower-energy peak and are shown in Figure 4.7. The 150 $^0$C-annealed *pure* SQ film are also shown in figure 4.7 for comparison. The normalized peaks are blue-shifted from 676 nm to 660 nm as we move from the pristine blend film to the 120 $^0$C-annealed blend film (the 150 $^0$C-annealed pure SQ film has this absorption peak at 674 nm). The H-aggregate peaks also blue-shift slightly from 559 nm to 552 nm (the 150 $^0$C-annealed pure SQ film has this absorption peaks at 542 nm). So after annealing, the absorption spectra of SQ:PCBM blended films mimic the absorption spectra of SQ neat films, which is consistent with our interpretation that the $DBSQ(OH)_2$ forms H-aggregates upon annealing.

From normalized spectra in Figure 4.7, we clearly see the peak shifting at ~650 nm. This peak becomes the Davydov peak in the annealed films. This further proves the formation of H-aggregate and the phase separation during annealing. We assign the lower energy peak to a Davydov split J-state in these annealing films. This further supports the formation of the H-aggregate as a results of phase separation during annealing. Comparing the blended films to the neat films in this figure, the higher energy of the ~650 nm peaks and the higher blue to red peak ratio suggests that the presence of PCBM may favor the formation of H-aggregates upon annealing.

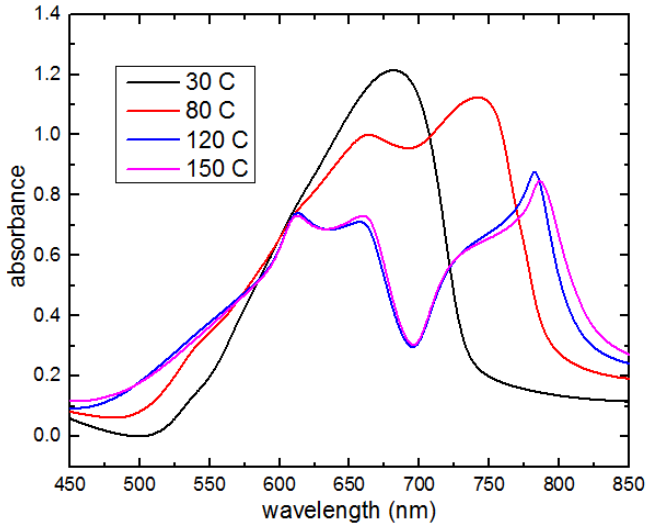


**Figure 0.8** UV-Vis absorption spectra of DBSQ:PCBM blend films before and after annealing.

The absorption spectra of DBSQ:PCBM blend thin films (1:1 w/w, spin coated from chloroform solution) are shown in figure 4.8. The pristine film has a broad and unsymmetrical absorption with maxima at 681 nm. After annealing, the broad absorption splits into two peaks, at 693 nm and 741 nm. It further splits into four absorption peaks at: 613 nm, 658 nm, 740 nm and 786 nm with a high temperature anneal. The whole absorption shifts towards the NIR after annealing.

The peak at 786 nm is close to the J-aggregate absorption assigned in the DBSQ annealed neat film spectrum, and we similarly assign it to the J-aggregate here. Similar to $DBSQ(OH)_2$, the

pristine SQ:PCBM blend film has very little aggregate absorption. This is also attributed to the disruption of SQ aggregation induced by the PCBM. The annealing treatment of the films "brings back" the J-aggregates. In comparison to the annealed neat films with two flat absorption peaks (Figure 4.5), the annealed blended films show four distinct absorption peaks.

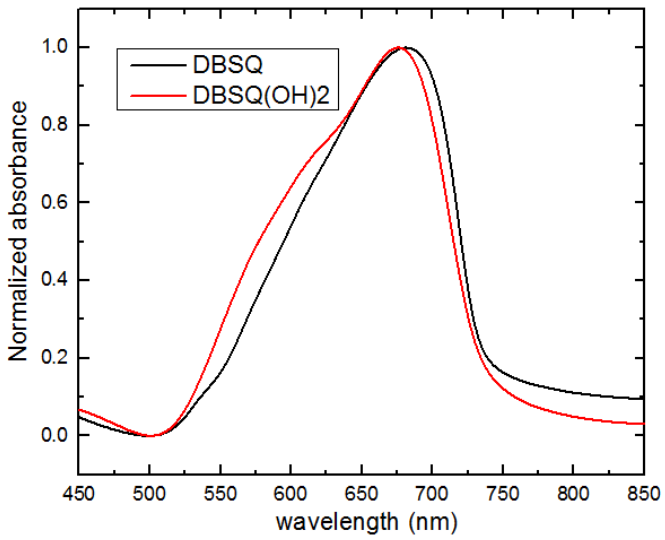


**Figure 0.9** Normalized absorption spectra of pristine DBSQ:PCBM and DBSQ(OH)2:PCBM blend films.

The DBSQ and DBSQ(OH)$_2$ blend films share some similar features in their absorption spectra; the PCBM disrupts the aggregate formation in the pristine films, but contributes to pronounced phase separation after annealing. The absorption spectra of the pristine blended films normalized to the peak for the two SQs are very similar as shown in Figure 4.9. The absorption maxima of DBSQ and DBSQ(OH)$_2$ films are at 681 nm and 676 nm respectively. This similarity is observed despite them forming different aggregates after annealing, and is attributed to the similar molecular back bones (D-A-D) and molecular arms (butyl chains in both cases). This is thought to lead to a similar interaction between the SQ and PCBM molecules. In pristine blended films, both SQs are considered to be interacting with PCBM as individual monomers. This interaction is also interpreted to be the main reason for spectral broadening as compared to the

squaraine monomer in chloroform solution. In other words, this broadening may represent a range of different environments with a range of different dielectric constants, given that the molecules are relatively frozen in space when compared to the solutions.

## 4.3 Summary

The absorbance of neat and blended SQ films is presented and discussed in this chapter. The neat films results show that different types of aggregates are presented in the $DBSQ(OH)_2$ and DBSQ films respectively. This are interpreted in that the enhanced planarity and conjugation due to the intramolecular H-bond induced by hydroxyl groups lead to a H-aggregate formation in the $DBSQ(OH)_2$ films. H-aggregates formed by $DBSQ(OH)_2$ has a well-defined absorption spectra with two absorption peaks perhaps because the strong aromatic-aromatic π-π stacking force. This is consistent with the face-to-face stacking geometry of typical H-aggregates. However, for DBSQ without the intramolecular H-bond, J-aggregates are formed with a less-defined absorption profile (figure 4.8). We infer that the less rigid molecular backbones of DBSQ that has not been "locked" by the intramolecular H-bonds weaken the aromatic-aromatic interaction between adjacent molecules, and thus a head-to-tail arrangement (J-aggregate) is obtained in the DBSQ films.

The existence of PCBM (in 1:1 w/w ratio) disrupts SQ's aggregation, supported by the observation that SQs in pristine (unannealed) films behave like monomers, rather than aggregates. Nevertheless, annealing recovered the aggregation in the active layer. The disruption and recovery of aggregation through spin-casting and annealing processes offer an excellent opportunity to individually investigate monomer-PCBM active layers and aggregate-PCBM active layers for SQ-based OPV devices.

From the absorbance of SQ neat films and blended films, we acknowledge that the DBSQ absorbs more towards the NIR in the solar spectrum (due to its J-aggregate), while $DBSQ(OH)_2$

absorbs more in the visible region (due to its H-aggregate). Given the larger number if NIR photons in the solar spectrum, DBSQ is seemed to be better as an absorber material in the OPV devices. However, we should also consider that the ordered π-π stacking of $DBSQ(OH)_2$ will likely build a strong connection between each molecule. This closer packing will likely enhance the exciton diffusion and charge transport steps (chapter 1.1.2). The irregularity of DBSQ absorbance may reflect the relative amorphous structure in the solid state film, which may become a drawback for charge transport in the photovoltaic devices.

Surprisingly on the other hand, the absorbance of SQ/PCBM blend films is similar between these two squaraines. This is likely due to both squaraines shared a similar molecular back bone (D-A-D) and same molecular arms (butyl chain).

For each SQ aggregate, there are two absorption bands, and we still cannot assign these two bands with full confidence. We know each band has clearly observable vibrational structure. This suggests that there are vibronic couplings in the aggregates, and that indeed there may be two separate aggregates – each with strong vibronic coupling. Further investigation of the intermediate state between the solution and the solid states, from monomer to aggregate, is required in order to approve our hypothesis. This intermediate state is obtained through making PMMA solid solutions and with the use of $H_2O$/THF mixed solvents in next chapter.

# Chapter 5 SQUARAINES IN PMMA SOLID SOLUTION AND $H_2O$/THF DISPERSION

## 5.1 Introduction

From chapter 3 and chapter 4, we know that the photophysical properties of SQ vary a lot from solution to solid state. For example, the excited state of SQ in chloroform solution can fluoresce, and the quantum yield for fluorescence is very high (≥ 80%). But the fluorescence of SQ in solid state films is too low to be detected (no fluorescence can be detected for $DBSQ(OH)_2$, and very little fluorescence can be detected for DBSQ neat films). We also know that this phenomenon is closely related to the aggregation property of SQs. The SQ in chloroform solution is in its monomer form. However, once squaraines have been spin-coated as thin films, aggregation occurs readily and the interaction between SQ molecules and aggregates has tremendously changed their photophysical properties. Therefore, we are in a situation where we cannot investigate aggregates in solution or monomers in the solid state. It is hard to build a connection between solution and films, and thus profoundly understand the SQ's properties.

Even though the terms "H-aggregate" and "J-aggregate" have commonly been used to assign the absorbance peaks in dye research, the essential meaning of the aggregate for SQs has not been fully understood by the scientists and researchers. In this chapter, we attempt to use Poly(methyl methacrylate) (PMMA) as an inert media to make solid solutions for our SQs.

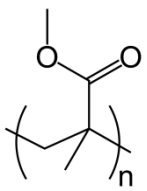


**Figure 0.1** Chemical structure of PMMA polymer.

PMMA (as shown in Figure 5.1) is a transparent thermoplastic, and will not absorb in the UV-Vis spectrum. At the same time, it is inert to interactions with SQs, that would lead to SQ property changes. Its good solubility in chloroform allows it to be easily co-dissolved. The main purpose of using PMMA is to prevent the SQ molecules from aggregating after the spin coating process, because the PMMA acts as a buffer. If we can obtain SQ monomers in PMMA solid solutions, and the SQ monomers will not significantly interact with PMMA, we can study the photophysical properties of SQ monomer in a frozen state. We can also more easily explore an increase in SQ concentration since the films are thin and absorbance can accurately be measured with such a small path length.

Another advantage of this solid solution experiment is that upon annealing, the disrupted monomer SQs will aggregate in PMMA films. The melting point of pure PMMA polymer is known to be 160 $^{0}$C. As annealed at 155 $^{0}$C, the polymer will be "softened". The assumption here is that these molecules can diffuse through the PMMA skeleton and aggregation will occur if and when the SQ molecules combine towards a more thermodynamically stable state. The process of aggregating can be monitored by absorbance spectroscopy, which provides a lot of information on how aggregation affects the excited state of each molecule.

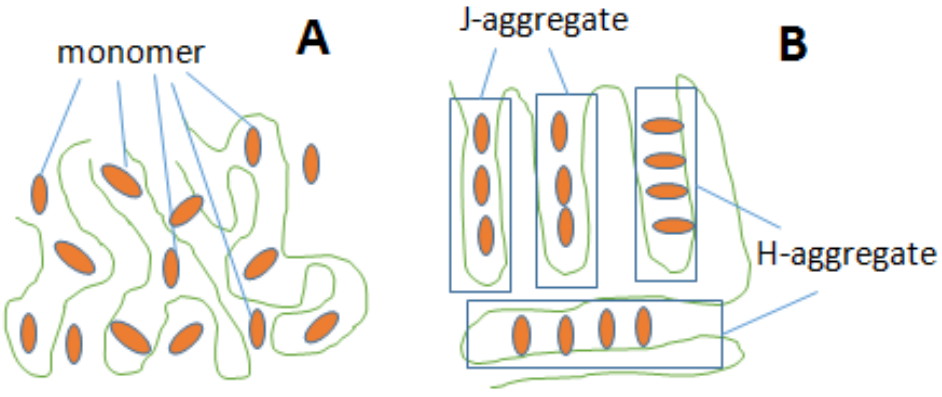


**Figure 0.2** Schematic of morphology showing SQ in PMMA solid solutions. A: before annealing; B: after annealing.

A schematic is shown in Figure 5.2 illustrating the morphology of PMMA solid solutions before and after annealing. In morphology A, the SQs are randomly distributed in the PMMA polymer chains. The relative dipole moment of each SQ molecule is not aligned. There is very little interaction between each individual SQ molecule. Therefore, the SQ in morphology A is assumed to be monomeric. After annealing, the polymer and SQ molecules are highly organized and packed, as illustrated generally by morphology B. Face-to-face packing would yield the H-aggregate, while the head-to-tail packing yields the J-aggregate.

Besides PMMA solid solution, which retains the SQ monomer in a solid state, another experiment is conducted to induce aggregation in solution (or dispersion); a mixed solvent $H_2O$/THF dispersion. THF is an aprotic solvent with a dielectric constant of 7.6. It is a moderately polar solvent (with polarity index of 4.0) and can dissolve a wide range of non-polar and polar chemical compounds, including squaraines. $H_2O$, with polarity index of 10.2 and dielectric constant of 80.10 at 20 °C, is an inorganic solvent which cannot dissolve most of the organic compounds, but is miscible with THF, leading to an ability to vary the solvent quality.

A squaraine stock solution was prepared in THF and rapidly injected into water while sonicating. After the injection, the $H_2O$ molecules quickly mix with THF molecules, resulting in formation of nano-sized aggregates. The water is sonicated during the injection in order to keep the aggregated particle size small. Due to their small size, the aggregation particles are suspended in the mixed solvent to form a quasi-stable dispersion. Therefore, a film-like spectroscopic feature can be obtained in the dispersions.

The steady-state spectroscopic properties of squaraine aggregates that were formed in solutions are characterized. In this way, we can obtain an analog of the thin film by using much less material than that would be required through a conventional spin-coating approach. It can also help us to investigate the aggregation formation process in solutions, which may differ from that in PMMA films. If we have self-consistent results in both PMMA solid solution and $H_2O$/THF

dispersion, it illustrates that the aggregate obtained in dispersion and solid solution is likely to be the same aggregate obtained in the thin film.

## 5.2 Experiment

**PMMA solid solution**. PMMA and SQ were weighed out consecutively into pre-cleaned vials. A certain amount of chloroform was added to each to make different concentrations. The concentration of SQ in the solid solution refers to the weight ratio of SQ/PMMA. The concentration of PMMA in chloroform was fixed at 40 mg $mL^{-1}$, while the concentration of SQ was varied for different weight ratios. Once chloroform was added, the vial was capped, parafilmed and heated at 40 $^0$C for 20 minutes to fully dissolve the polymer. The spin coating was conducted at a spin speed of 3000 RPM for 45 seconds. The films were kept in the plastic film holders.

**$H_2O$/THF dispersion**. The THF monomer solution for each squaraine was first made and sonicated for 5 min. These solutions were further diluted to different concentrations. Then, each THF solution was quickly injected into deionized water during sonication to make dispersions. Once the solutions were prepared, they were tightly capped and were sealed with parafilm to prevent solvent evaporation. A quartz cuvette of 1 cm path length was used for all steady-state measurements. The cuvette was cleaned using THF when finished each solution measurement, and was dried using nitrogen gas. The absorbance and fluorescence were conducted using a Shimadzu UV-2401 PC UV-Vis spectrophotometer and a Horiba Jobin Yvon FluoroMax-4 Spectrofluorometer, respectively. The instrument set up has been described in section 2.2 of the chapter 2.

## 5.3 Results

### 5.3.1 SQ in PMMA solid solution

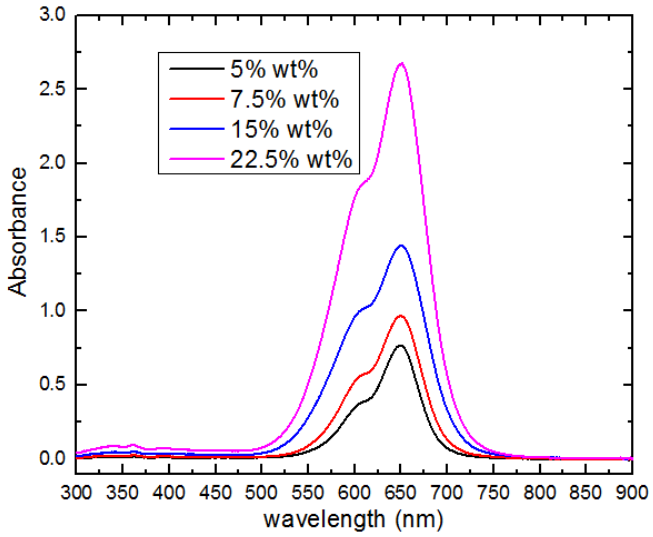


**Figure 0.3** Absorbance of DBSQ(OH)2 in PMMA solid solution.

The absorbance of $DBSQ(OH)_2$ PMMA films is shown in Figure 5.3. The absorption intensity varies with different concentrations of SQ in PMMA. Nevertheless, the absorbance peaks for all four different SQ concentrations were at the same position (650 nm). This peak is consistent with the absorbance of $DBSQ(OH)_2$ in chloroform solution (at 650 nm), suggesting that it is a peak associated with the SQ monomer absorption. From the spectra, we notice that the absorbance of $DBSQ(OH)_2$ in PMMA film is slightly broader than the absorbance in chloroform solution, which can be seen more clearly in the normalized spectra of Figure 5.4.

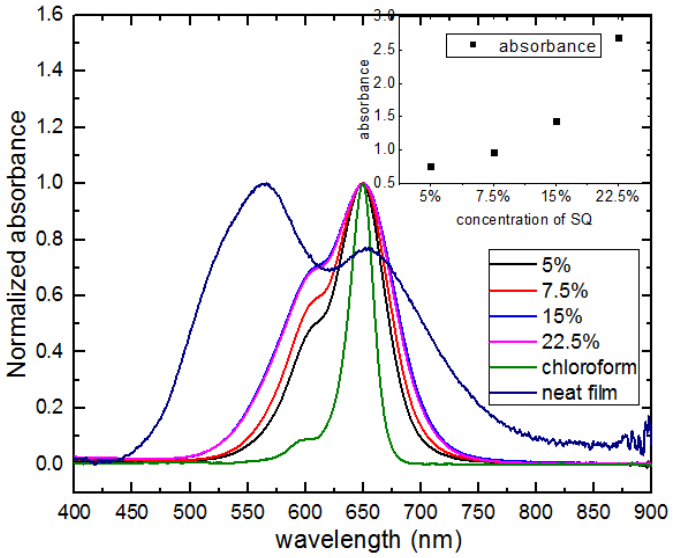


**Figure 0.4** Normalized absorption spectra of $DBSQ(OH)_2$ in PMMA solid solution with a comparison to chloroform liquid solution and neat thin film spectra. Inset shows peak absorbance for the solid solution films as a function of squaraine weight percent (SQ/(SQ+PMMA)) in the original solution used for spin casting.

The normalized absorption spectra of $DBSQ(OH)_2$ in PMMA solid solution are shown in Figure 5.4 with neat film and chloroform solution as comparisons. The absorption peak of the PMMA films and the chloroform solution are all at 650 nm. The two absorption peaks of the neat film are at 562 nm and 652 nm, and the absorption peak in the SQ:PCBM blend films is at 676 nm. The peak absorbance values for the solid solution films, as a function of the weight percent of squaraine relative to PMMA in the original spin casting solution, are shown in the inset. As concentration (wt%) increases, it appears as if a Beer's Law relationship is not followed. This suggests that as the concentration of SQ is changed, it slightly impacts the viscosity of the solution so that the film thickness is thus changed, higher viscosity leads to thicker films in spin coating.

The concentration of the PMMA polymer is still considered as the main factor influencing the viscosity of the solution, and thus the film thickness. Higher the SQ concentrations lead to

higher densities of SQ in thin films, and thus a smaller intermolecular distance. So the intermolecular distance should be inversely proportional to the SQ/PMMA weight ratio, assuming this ratio is not too high. We can calculate the average intermolecular distance to be 2.45 nm at 5% SQ by weight and 1.39 nm at 22.5% by weight given the molarities of 0.11 mol $L^{-1}$ and 0.62 mol $L^{-1}$ respectively. These molarities were estimated based upon the weight ratios of SQ to PMMA and the density of PMMA. These are very different values compared to the ~ $10^{-5}$ mol $L^{-1}$ concentrations used for liquid solution measurements. It is clear that the intermolecular separations are much smaller in PMMA solid solutions than in liquid solutions, but still an order of magnitude higher (~1-2 nm) than the interplanar spacing seen in a crystal structure (3.3 Angstroms).[20] Clearly there are interactions between squaraines that give rise to a broadening and a relative increase in the shoulder height at 600 nm compared to the peak at 650nm.

The broadening of the main peak appears symmetrical. The random interactions between close squaraine neighbors lead to a symmetric broadening associated with stabilization (J-like) and destablilization (H-like) of the excited state caused by long-range SQ orientational disorder. The relative increase in the shoulder is likely a specific electronic interaction between two squaraine transition dipole moments. The symmetric broadening is likely reflective of the fact that all squaraine neighbors are randomly oriented. This would suggest that in a spin-cast film there is a substantial amount of symmetric broadening caused by interaction with randomly aligned neighbors. The broadening can thus indicate the energetic disorder associated with all the states in the film.

From these normalized absorption spectra, we can see that the $DBSQ(OH)_2$ did not aggregate in the as-cast PMMA solid solution. The same peak position in the PMMA film as in chloroform solution suggests the polymer successfully “separates” the SQ monomers. However, the absorption spectra of SQ-PMMA films are different from those of chloroform solution because of their broadening. The FWHM of absorption in chloroform is only 0.073 eV; while the

FWHM are 0.197 eV, 0.246 eV, 0.312 eV and 0.309 eV respectively as the weight ratio of SQ increase from 5% to 22.5%. The FWHM of each SQ-PMMA film corresponds to the SQ ratio linearly at first, but a threshold is reached after the ratio of 15% (Figure 5.5). This change in FWHM is considered to originate from the symmetric broadening of the main peak and the increase in the shoulder height.

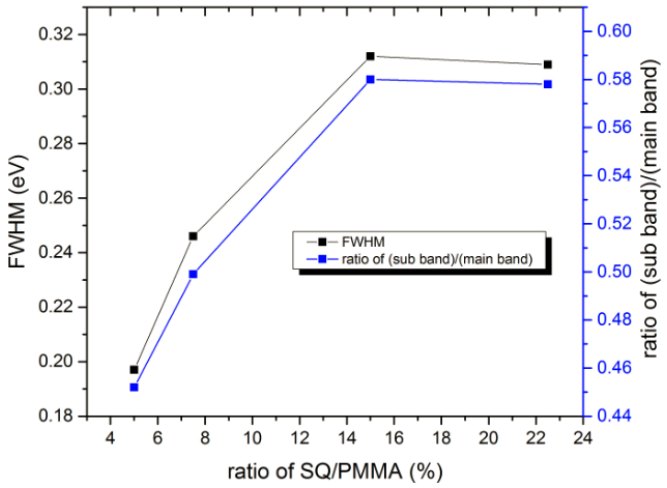


**Figure 0.5** The FWHM of SQ-PMMA film absorbance and the ratio of absorbance shoulder to maximum absorbance as a function of SQ/PMMA ratio.

The correlation of FWHM of the absorbance peak and the ratio between absorbance shoulder (~600 nm) and the absorbance peak (at 650 nm) to SQ/PMMA weight ratio is shown in Figure 5.5. As the SQ/PMMA weight ratio increases, the broadening of the absorbance peak, along with the peak ratio (sub-band to main-band ratios are 0.452, 0.499, 0.58 and 0.578 consecutively), correspondingly increases. This suggests that the broadening comes from the contribution of the sub-band.

The peak ratio relationship with the SQ/PMMA weight ratios almost identical to the FWHM relationship, as shown in Figure 5.5. This is consistent with our assumption that the spectral broadening is partially caused by the growing absorbance “shoulder”.

**Table 0.1** The parameters for Gaussian fitting of normalized absorbance of SQ-PMMA films. For easy comparison, the unit for FWHM is in "nm".

| | Sub-band absorbance | | | Main absorbance | | |
|---|---|---|---|---|---|---|
| SQ/PMMA | Peak position | Peak height | FWHM (nm) | Peak position | Peak height | FWHM (nm) |
| 5% | 604.0 nm | 0.4049 | 54.15 | 651.5 nm | 0.9176 | 46.75 |
| 7.5% | 600.0 nm | 0.4382 | 59.43 | 652.3 nm | 0.9065 | 53.40 |
| 15% | 597.8 nm | 0.5333 | 75.18 | 655.8 nm | 0.8380 | 61.89 |
| 22.5% | 598.9 nm | 0.5375 | 75.59 | 655.6 nm | 0.8248 | 59.80 |

A Gaussian peak fitting is applied for all four normalized SQ-PMMA absorbance spectra; the parameters for two Gaussian functions are listed in table 5.1. From the results, we can see that the main absorbance peak is red-shifted to 655.6 nm, while the FWHM is increased to ~60 nm (For easy comparison, "nm" is the unit used here). The absorbance shoulder increased 42% in height from 0.40 to 0.54, and the FWHM increased 40% from 54 nm to 76 nm as the concentration of SQ increased. It seems that this broadening and the sub-band increasing stopped after the SQ/PMMA reached 15%. The detailed fitting results can be found in Chapter 7 Appendix (Appendix B), along with the fitting graphs.

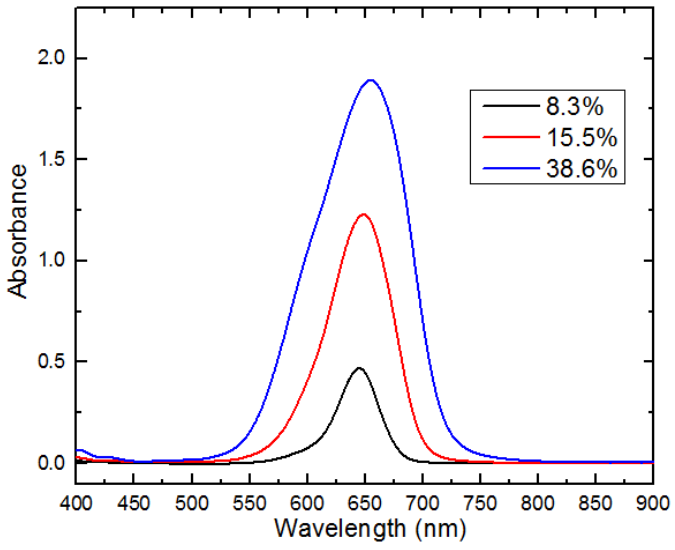


**Figure 0.6** Absorbance of DBSQ in PMMA solid solution.

The absorbance spectra of three samples with different weight ratios of DBSQ in PMMA solid solution are shown in Figure 5.6. The absorbance maximum red shifts from low to high SQ weight ratio (645nm – 8.3%, 649nm – 15.5%, 655nm – 38.6%). Similar to $DBSQ(OH)_2$, the absorbance spectra is gradually broadened (Figure 5.7). However, different from $DBSQ(OH)_2$, no absorbance shoulder appears, the broadening is evenly spread at left and right side of the main peak.

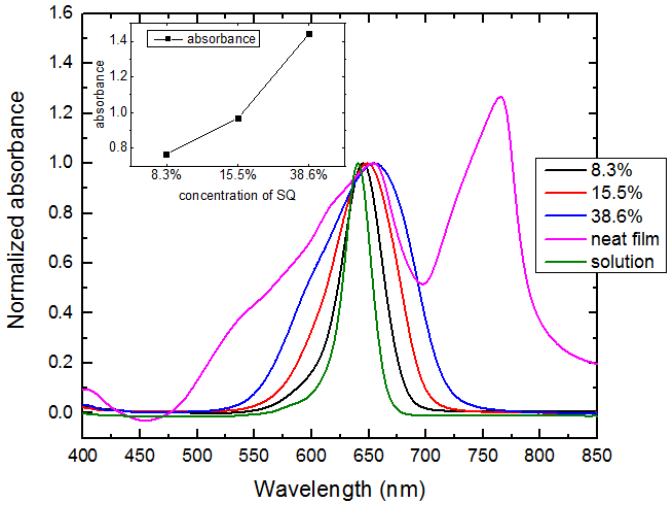


**Figure 0.7** Normalized absorption spectra of DBSQ in PMMA solid solution with a comparison to neat thin film and chloroform liquid solution spectra. Inset shows peak absorbance for the solid solution films as a function of squaraine weight percent relative to PMMA (SQ/(SQ+PMMA)) in the original solution used for spin casting.

The normalized absorbance of DBSQ-PMMA films is shown in Figure 5.7. From the spectra, we can clearly see the broadening of absorbance on both sides of the main peak, when increasing the amount of SQ. Again, the positions of the peak in the range of 600 nm – 700 nm are respectively 640nm (solution), 645 nm (8.3% PMMA film), 649 nm (15.5% PMMA film), 655 nm (38.6% PMMA film), 654 nm (neat film). The FWHM of these peak are respectively 0.081 eV (solution), 0.126 eV (8.3% PMMA film), 0.165 eV (15.5% PMMA film), 0.194 eV (38.6% PMMA film) and 0.422 eV (neat film).

For DBSQ, the broadening of the absorbance spectra never stops at any specific SQ/PMMA weight ratio. The absorbance peak shifting likely arises from the J-aggregate formation of DBSQ in PMMA films. As the intermolecular distance is reduced, the J-character is more dominant in the molecular interaction which leads to a larger red shift.

### 5.3.2 Annealing SQ-PMMA solid solution

In as cast SQ-PMMA films, the SQ seems to remain in its monomer form. These un-annealed films will later be compared with un-annealed blends of SQ with PCBM. These SQ:PMMA blend films were annealed and the results are rather remarkable. The annealing was conducted at 155 $^0$C (5 $^0$C below the melting point of PMMA). Through an incremental annealing, we can monitor the aggregate forming process, which can provide information about the SQ aggregate. For low SQ-PMMA solid solutions, the annealing is hardly able to induce any change in the absorbance spectrum Therefore only the highest SQ/PMMA ratio films are presented and discussed here

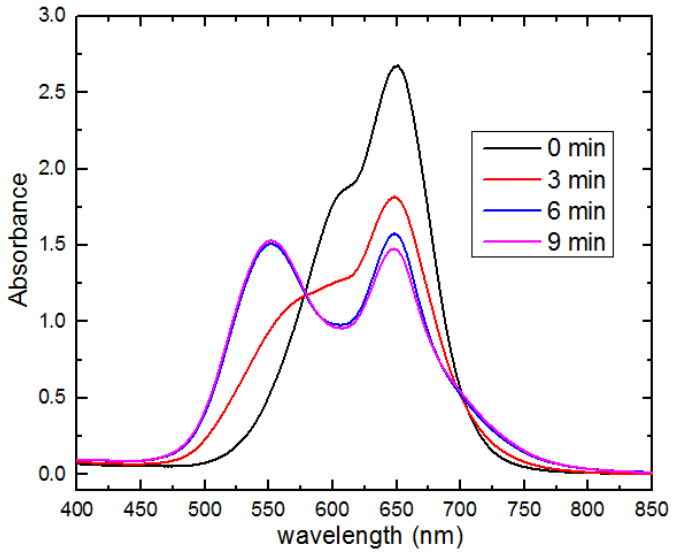


**Figure 0.8** Absorption spectra of DBSQ(OH)$_2$ in PMMA solid solution (22.5% by weight) with a range of annealing times.

The absorbance change as a function of annealing time for 22.5% DBSQ(OH)$_2$-PMMA films are shown in Figure 5.8. At 3 min, the absorbance peak at 650 nm has decreased dramatically compared with the pristine films. In addition, there is an increase in the absorbance at 500 – 575 nm, indicating the growing in the H-aggregate population. After 6 minutes of annealing, a threshold has been reached where a second peak at ~550 nm co-dominates with the peak at 650 nm. At 9 min, the absorbance peak at 552nm has changed very little compared to that at 6 min, indicating that aggregation is nearly complete. These peaks match well in position and relative height with the peaks of ~565 nm and 652 nm seen in the film absorption (where we should also point out that the 652 nm peak overlaps with the 650nm peak associated with the monomer) although the film spectra peaks are slightly more separated (which annealing also encourages for films).

Two Isosbestic Points (IPs) are observed at 578 nm and 590 nm during the spectral change, suggesting the depletion of one species as the second species is formed. In this case, we consider a transformation from SQ monomers to H-aggregates. As a result of observing this isosbestic point we assign the aggregate absorption to contain two peaks, one at ~550 nm and the other at 652 nm, which are more or less equally dominant in the absorption spectrum. We consider it is coincidental that the monomer peak so closely overlaps with the peak at 652 nm in the film / aggregate. Therefore, in the PMMA spectra, we claim an overlap between the SQ aggregate and the monomer absorption. Thus, the spectrum for the annealed PMMA film is made up of both monomer and aggregate, whereas the absorbance for annealed neat SQ film contains just the aggregate (the absorption of annealed neat SQ film is shown in chapter 4).

We also confirm the assignment of the peak at 650 nm to symmetrically broadened transitions because of the neighboring randomly oriented squaraines. The increasing shoulder height is assigned to electronic interactions between neighboring squaraines. This may help elucidate the true origin of the shoulder in the monomer/dilute solution spectrum. Annealing clearly allows for

molecular diffusion and phase separation and may be similarly observed in blends of SQ and acceptor in films targeted for OPV. More comparison between an annealed PMMA film and an annealed neat film is shown in Figure 5.9 below.

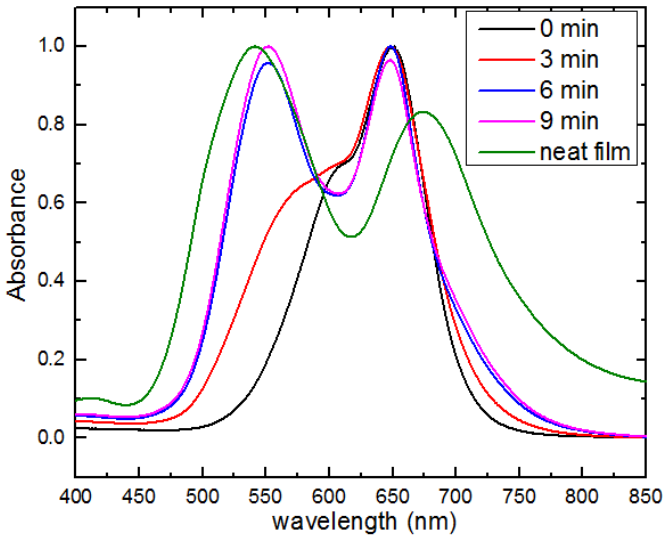


**Figure 0.9** Normalized absorbance spectra of DBSQ(OH)2-PMMA films as annealed (for 3 min, 6 min and 9 min). The absorbance spectrum of annealed neat film at 120 $^{0}$C for 1 minute was shown in green as comparison

The normalized absorbance spectra of DBSQ(OH)$_2$-PMMA films are shown in Figure 5.9. The two peaks for annealed PMMA films are at: 552 nm and 650 nm. The two peaks for annealed neat SQ films are at: 541 nm and 674 nm.

The pleasing match of absorbance at 500 nm – 600 nm between annealed PMMA films and neat SQ films is explained by both samples being dominated by H-aggregate absorption. The neat film has the H-aggregate peak more blue-shifted. This can be result from that the aggregate formation in PMMA films being hindered (through PMMA buffering) as compared to neat film. Hence, the effect of the solvent may be to shift the peak. The solvent for the PMMA films is the PMMA and the solvent for the neat films is the SQ itself. Each "solvent" has a different dielectric constant, and the dielectric constant of the "solvent" will affect the electron delocalization through the SQ molecule, and thus change its "band" gap.

The absorbance in the 620 nm-750 nm range is quite different for PMMA films and neat films. The absorption peak is at 652 nm in PMMA films and at 674 in neat films (the monomer peak in chloroform solution is at 650 nm), and the absorption peak is much narrower in PMMA film. It seems that in the PMMA film, we have SQ monomer, but in neat film, we have something else, such as the Davydov-aggregate species. Before we assign the SQ aggregate in the PMMA film to something different from the aggregate in neat film, we should also notice that this peak is broadened at 700 nm – 750 nm with an isosbestic point at 690 nm as mentioned above (Figure 5.8). I suggest that the broadening and isosbestic point are caused by the overlapping of SQ monomer absorption and Davydov splitting peaks. In PMMA film, the peak at 652 nm is more likely to be dominated by the monomer absorption. In neat film, the absorption at this region is dominated by Davydov absorption of SQ aggregates. This interpretation makes sense given that the SQ aggregates more easily in the neat film than in the PMMA polymer environment (the SQs are still dissolved in the polymer as a solid solution).

In summary, we believe that the annealed PMMA film is made up of both monomer and aggregate populations and the annealed neat film is dominated by aggregates.

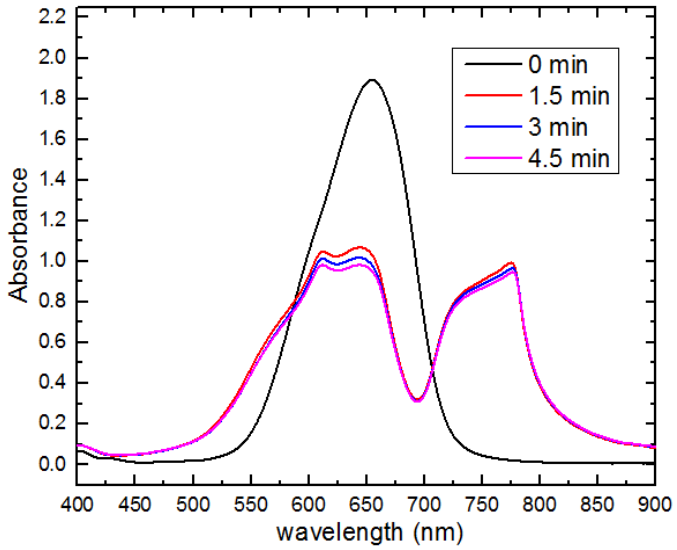


**Figure 0.10** Absorption spectra of DBSQ in PMMA solid solution with a range of annealing times.

Similar experiments were carried out for annealed DBSQ PMMA films. Similar trends are observed with DBSQ except that the aggregation is very fast and a threshold for change is already reached at 1.5 minutes with longer annealing times seemingly only contributing to some degradation (Figure 5.10). Therefore no isosbestic point has been confirmed. There are five absorbance features in the annealed spectrum at 555 nm (shoulder), 614 nm, 644 nm, 731 nm (shoulder), and 775 nm, corresponding respectively to the peaks at 540 nm, 610 nm, 653 nm, 730 nm and 765 nm for the unannealed thin film.

Compared to the $DBSQ(OH)_2$-PMMA film, the spectral change during annealing is much faster. One reason is that the ratio of SQ/PMMA is 38.6%, much higher than the $DBSQ(OH)_2$ in PMMA film. Therefore, the intermolecular distance is smaller in the DBSQ-PMMA film that was tested. Upon annealing, the SQ molecules are able to move a shorter distance, thus requiring shorter time to form the aggregate, thus requiring less time. The peak at 644 nm is interpreted to be the monomer absorbance (the absorption peak of the chloroform solution is at 640 nm). The absorbance at 731 nm and 775 nm is associated to the J-aggregate of DBSQ. The broad shoulder at 731 nm is due to the low molecular coupling in the J-aggregate as described in literature[73]. The irregular absorbance shoulder at 550 and the absorbance peak at 614nm are tentatively assigned to be the H-aggregate of the DBSQ.

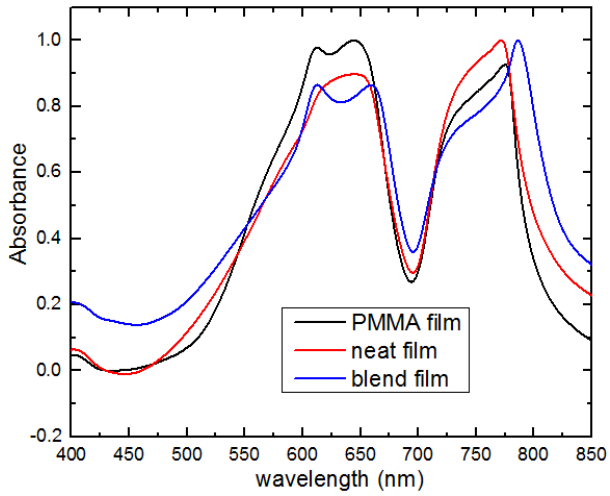


**Figure 0.11** Normalized absorption spectra of DBSQ in neat film (red), in PMMA film (black) and in SQ:PCBM blend film (blue). All these films are annealed before taken the absorption measurements.

The absorption spectra of DBSQ in neat, PCBM blends and PMMA films are shown in Figure 5.11. The good matching suggests that the SQ-aggregate structure are similar in these three types of films. It confirms that the DBSQ aggregates studied in PMMA films are similar to those aggregates in OPV devices (or SQ:PCBM blends).

The absorption of the PMMA film at 640 nm is higher in intensity than that of the neat and blend films. This can be explained by a higher monomer population in the PMMA films than in other types of films (as described above in DBSQ$(OH)_2$ section). The J-aggregate absorption peak of PMMA films (750 – 800 nm) blue-shifted by about 15 nm from the J-aggregate absorption peak.

### 5.3.3 Fluorescence of SQ monomer in PMMA solid solution

We have distinguished different absorbing species in the neat and PMMA films. In annealed neat SQ films, aggregates are the dominant species; while in as-cast PMMA films, monomers are the main absorbing species. The above SQ-PMMA films and SQ neat films pose a problem in that no fluorescence emission is obtained. It seems that the aggregate cannot fluoresce

and/or strong self-quenching is happened in SQ solid state. In this section, we spin coated lower SQ/PMMA ratio (≤5%) films such that the SQ intermolecular distance is large, so that fluorescence quenching would be minimized. The hypothesis is that the fluorescence would thus be coming from the monomer and that after annealing the fluorescence intensity would decrease as the monomer population decreases.

The experimental results did show the fluorescence spectra of low SQ concentration PMMA films in the fluorometer. However, the decrease in fluorescence emission intensity is tremendous, so that the PLQY of any PMMA films with ≥1% SQ is measured to be 0, and the fluorescence spectra are very "noisy" due to the detection limit of the instrument. Therefore these data will not be shown in this section. Nevertheless, the TCSPC system is substantially more sensitive and differentiates between fluorescence and noise because the noise has no time profile. The fluorescence lifetime measurement gives another description of fluorescence. The lifetime is calculated by:

$$\tau = \frac{1}{k_r + k_{nr}} \tag{5.1}$$

where $\tau$ is the fluorescence lifetime, $k_r$ is the radiative decay constant and $k_{nr}$ is the non-radiative decay constant. When quenching happens, the non-radiative decay is favored, thus the fluorescence lifetime $\tau$ is decreased.

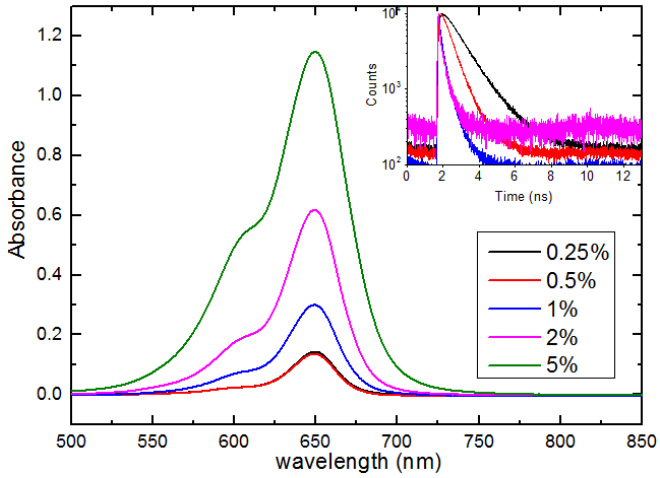


**Figure 0.12** Absorbance for low SQ weight ratio PMMA films; inset: fluorescence decay when excited at 620nm: black: 0.25% PMMA film; red: 0.5% PMMA film; blue: 1% PMMA film; pink: 2% PMMA film.

The low SQ weight ratio PMMA films were spin coated by the similar procedure as the PMMA films described above, but at lower spin speed in order to get a thick enough film. The lowest SQ/PMMA films (0.25%, w/w), were spin coated at 1000 RPM; the rest of the films were spin coated at 1500 RPM. The absorbance spectra of each low concentration SQ/PMMA film were shown in the Figure 5.12. The overlapping of 0.25% and 0.5% PMMA films is because they were spin coated at different spin speed. The inset is the time profile for fluorescence lifetime measured using TCSPC system. The excitation wavelength is at 620nm, while the emission wavelength is set to 695nm. The fluorescence lifetimes are (obtained by the mono-exponential fits of the decay curves) 1.1 ns, 0.6 ns, 0.3 ns and 0.3 ns for a 0.25 % PMMA film, a 0.5 % PMMA film, a 1% PMMA film and a 2% PMMA film respectively. The fluorescence signal for 5% PMMA films is so weak that its lifetime cannot be accurately measured. As a comparison, the fluorescence lifetime of DBSQ(OH)2 in chloroform solution is 2.3 ns.

Here I should state that the spin speed for the 0.25% PMMA film is lower than for the others, but the SQ-to-SQ intermolecular distance is assumed to only correspond to the weight ratio of SQ/PMMA, and not the spin speed. The intermolecular distance is the only factor affects

the fluorescence quenching (thus fluorescence lifetime) as there are no other quenchers present. Therefore, the fluorescence intensity and fluorescence lifetime measurement of the 0.25% PMMA films are consistent with the measurement results of other PMMA films (and the comparison is valid).

The decrease in TCSPC results indicates a decrease in fluorescence lifetime upon only a slightly increase in the SQ concentration. In such a low SQ weight ratio, the aggregate is almost nonexistent since the populations of the SQs are low. Therefore, such a decrease in fluorescence lifetime is interpreted to be associated with SQ self-quenching. Above all such measurements have less values because of the experimental difficulty in measuring fluorescence. The assumption made also contribute to us not taking our interpretation further forward.

### 5.3.4 The SQ aggregate in $H_2O$/THF mixed solvent

SQ is forced to aggregate in $H_2O$/THF mixed solvent as described in the introduction of this chapter. This method was only successfully applied to $DBSQ(OH)_2$, but not DBSQ. However, the absorbance of $DBSQ(OH)_2$ in $H_2O$/THF mixed solvents presents strong evidence for the Davydov peak hypothesis. A Davydov split aggregate is associated with two or more molecules that are arranged in a herringbone-like packing structure such that there is oscillator strength to both a lower energy excitonic state and a higher energy excitonic state resulting from the interaction of the transition dipole moments in that aggregate.

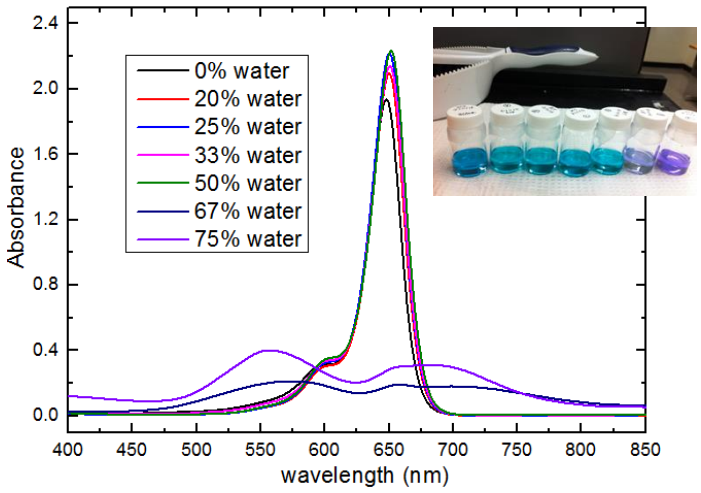


**Figure 0.13** The absorbance spectra of $DBSQ(OH)_2$ in $H_2O$/THF mixed solvent for different water volume percentages. Inset: a photo of the dispersions with an increasing $H_2O$ content from left to right.

The absorbance spectra of each DBSQ(OH)2 dispersion with different volume percentage of water is shown in Figure 5.13. 0% water refers to $DBSQ(OH)_2$ dissolved in pure THF. In the spectra, there is a slight difference in absorption peak heights for each solution. This may indicate that the concentration of individual squaraine molecules is slightly changing, or that the extinction coefficient is changing as the polarity and dielectric constant (polarizability) of the solvent is changing. The last two spectra for solutions of water percentage 66.7% and 75%, respectively, show a great change in absorption spectrum, with a dramatic decrease in absorption intensity. No isosbestic point was observed in the Figure. This is likely because of the high light scattering of the dispersions, which leads to an error in the spectral "intensity" values. Further details are shown after normalization in Figure 5.14.

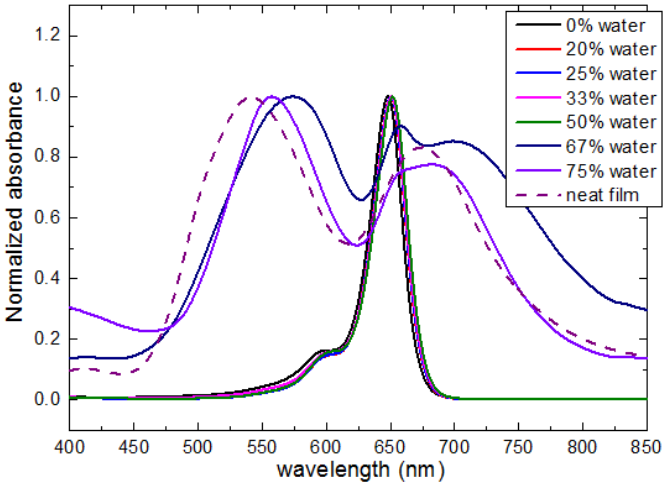


**Figure 0.14** Normalized absorbance spectra of DBSQ(OH)2 in H2O/THF mixed solvent for different water volume percentages; dashed line: normalized absorbance of annealed DBSQ(OH)2 neat film.

All dispersions from this experiment are presented in Figure 5.14, normalized to their peak absorbance. The first five spectra are similar. Nevertheless, there is a small red-shift of the absorption peak from 648nm in the 100% THF solution to 651.5nm in the 50% $H_2O$/THF solution. This is interpreted to be due to the changes in solvent properties, in that the HOMO and LUMO energy levels of the squaraine may be stabilized differently by the higher polarity of H2O. The high absorption at 400 – 450 nm is due to scatter of larger aggregation particles that form in the dispersions.

The absorbance spectra of 67% and 75% dispersions are very similar to the neat film spectrum of $DBSQ(OH)_2$. This therefore provides a strong evidence to prove the existence of the aggregate in the dispersion. The spectra in the 450-600nm region are similar for the THF:H2O suspensions and the neat film, and this peak is therefore assigned to the formation of H-aggregates. We should notice in the 67% dispersion spectrum, the monomer absorbance peak is still identifiable at 658nm. This is the evidence that the peak at ~700nm in the film absorbance spectrum is not associated with the monomer, but with the J-aggregate or Davydov split absorbance peak.

## 5.4 Summary

From SQ-PMMA films, we have monitored a population change from monomer to aggregate through absorbance spectroscopy. In PMMA films, we successfully "froze" the SQ molecule as a monomer form in the solid state. Annealing induces a clear transformation of SQs from monomer to aggregate, but we see an inhibition of Davydov peak formation for $DBSQ(OH)_2$. This inhibition is tentatively explained by a disturbing of the herringbone structure by the PMMA polymer chain.

In PMMA films, we have little phase separation without annealing. We assume that only SQ monomers exist in these as-cast PMMA films. With annealing, we have more phase separation and we can control the domains. In the next chapter, the impact of annealing on device efficiency will be shown. The SQ in general will mix well with the PCBM in blended film and will phase separate upon annealing (as shown in chapter 4). This is beneficial since it will allow control of domain size.

The $DBSQ(OH)_2$ in PMMA solid solutions and $H_2O$/THF dispersions provide valuable and rare information about the excited state of this SQ through fluorescence lifetime measurements. TCSPC showed a rapid reduction in lifetime as SQ concentration increases, perhaps resulting from internal conversion to J-level of the Davydov aggregate. Since the quantum yield of fluorescence is so low, the interpretation from this data are severely limited. Nevertheless, we must also question the formation of a quasi-stable excited state that does not fluoresce in the future. It may be valuable to compare EQE measurement with absorbance to address this hypothesis further.

We have ultimately determined that the $H_2O$/THF dispersion is a good representation of films. It provides a strong evidence for the Davydov peak hypothesis as mixed solvet spectra show absorption features of H-aggregate, monomer and Davydov peak at the same time. From the

previous discussion, a herringbone aggregate has both H-character and J-character, resulting in both H-bands (blue-shifted from monomer) and J-bands (red-shifted from monomer).

# Chapter 6 SQUARAINE-BASED PHOTOVOLTAIC DEVICES

## 6.1 Introduction

Squaraines, with high extinction coefficients and panchromatic absorbance in the solid state, promise to be good donor candidates for OPV. As discussed above, the absorbance of SQs in solution is very sharp, but the panchromaticity of SQ absorbance in the solid state is mainly due to aggregation; formation of H- or J-aggregates. Coexistence of H- and J-bands (this is the property of "Davydov" aggregates, refers to figure 4.3) with monomeric bands would extensively expand the photoactive response of solar cells. For example, as show in Figure 4.1, $DBSQ(OH)_2$ has an intense and narrow absorbance peak in chloroform solution with a full width at half maximum (FWHM) of ~ 0.08 eV . Nevertheless, the absorbance of $DBSQ(OH)_2$ has been broadened with a FWHM of ~ 0.68 eV in thin films. Upon thermal annealing, the FWHM of absorbance has further broadened to ~ 0.82 eV, allowing SQs to capture photons from 500nm to 800nm.

In chapter 4, we demonstrated that in as-cast SQ:PCBM films, the SQ aggregation is disrupted by the PCBM, and that annealing recovers the SQ aggregate, and leads to an phase separation. By controlling the annealing temperature, we can control the domain size (or SQ aggregation size). It is generally considered that aggregates will be observed in crystalline domains, while monomers will be observed in amorphous regions. In chapter 5, the SQ monomers and aggregates are proved to have different photophysical properties, i.e. energy levels and excited state lifetimes. Understanding their individual contributions to OPV performance is an important step to improve device efficiencies and functionalities.

## 6.2 Experiment

**Device making**. The ITO coated glass substrates were consecutively cleaned in Acetone and iso-propyl alcohol (IPA) ultrasonic baths. On top of the ITO, a PEDOT:PSS solution (Cleavios PH 750, $\sigma$ = 10-100 S $cm^{-1}$, diluted 1:1 with deionized water) was spin cast at a spin speed of 5000 RPM for 45 seconds. The PEDOT:PSS films were then baked in an vacuum oven at 160 $^0$C for 30 minutes. The substrates were then immediately transferred into a nitrogen-filled glovebox for deposition of the active layer.

SQ and PCBM were dissolved together in chloroform to achieve the weight ratio of 1:1 SQ to PCBM with a concentration of SQ of 8mg/mL. Before spin casting, the solution was sonicated in an ultrasonic bath for 30 minutes in order to fully dissolve the materials. This solution was then spin coated onto the PEDOT:PSS films at a spin speed of 800 RPM for 18 seconds. After the active layer was deposited, the films were transferred into a high vacuum chamber, where Al (200nm) was evaporated onto the active layer as the top electrode. The spin-casting of the active layer and the aluminum evaporation are conducted in a glovebox where the devices were briefly stored before efficiency testing. The final structure of the devices is summarized as: ITO/PEDOT:PSS/SQ:PCBM/Al.

After the aluminum evaporation process, 6 of 8 films were annealed at different temperatures (80 $^0$C, 120 $^0$C and 150 $^0$C, 2 films for each temperature) for 60 seconds. The other 2 films were to stay "pristine" as a comparison/control.

**EQE measurement**. The spectral response of the squaraine devices was measured on an Optronic Laboratories 750 spectroradiometric system. A high intensity quartz halogen bulb was used as the light source; the lamp was calibrated against an NERL traceable Si standard before the EQE measurements were made.

The experiment was conducted in a dark room to reduce noise from any unwanted light sources although phase sensitive detection was used. Two light confined pads with a 1.25mm-slit width in the center were placed in the front and back of the monochromator, thus further reducing the leakage of unwanted light. The increment of the spectral scan is 10nm from 300nm to 900nm.

**J-V measurement.** The J-V measurements were performed using a Newport 91159 Full Spectrum solar simulator with a power density of 100 mW $cm^{-2}$ (1-sun illumination). The xenon lamp in the solar simulator is calibrated with a Round-Robin InGaAs photovoltaic cell fabricated at NASA. The OPV devices were tested immediately after fabrication by a four-point probe method. The output bias was scanned from -2 Volts to 2 Volts with a 20 mV increment. The current density of the OPV devices (under 1-sun illumination) was thus measured as a function of the output bias. The short-circuit current ($J_{SC}$), open-circuit voltage ($V_{OC}$) and fill factor (FF) were calculated by inserting the raw data into a calculating spreadsheet.

## 6.3 Results and discussions

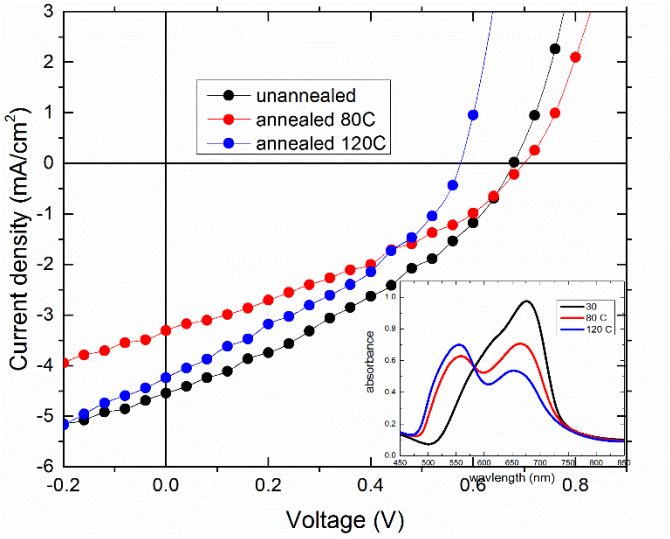


**Figure 0.1** Summarized J-V curve measurement for $DBSQ(OH)_2$:PCBM (1:1 w/w) devices. Inset: absorption spectra of $DBSQ(OH)_2$:PCBM (1:1 w/w) blend films annealed at 80 $^0$C and 120 $^0$C respectively.

Figure 6.1 shows the J-V curve characters of $DBSQ(OH)_2$:PCBM (1:1 w/w) OPV devices under different annealing temperatures, with the inset showing the absorption after annealing. This diode-like J-V curve demonstrates the success of using this SQ as electron donor material in the OPV (with an average efficiency of 1.21% for as-cast devices). It should be reported that these devices are un-optimized (for example, with no electron transporting layer), and this efficiency can be improved through well-known but time-intensive processes. The pre-annealing treatment (at 80 $^0$C, 120 $^0$C and 150 $^0$C) was performed on the devices, and the efficiency dropped to 0.51%. More detailed device parameters are listed in table 6.1 below.

**Table 0.1** Important device parameters of $DBSQ(OH)_2$:PCBM (1:1 w/w) OPV devices before and after thermal treatments. The data in the parentheses are the maximum recorded efficiency that obtained.

| Thermal treatment | $J_{sc}$/mA cm$^{-2}$ | $V_{oc}$/V | FF | η |
|---|---|---|---|---|
| Un-annealed | 4.57 (5.04) | 0.69 (0.72) | 0.33 (0.33) | 1.09% (1.21%) |
| 80 $^0$C-annealed | 3.30 | 0.69 | 0.36 | 0.80% |
| 120 $^0$C-annealed | 4.26 | 0.57 | 0.37 | 0.88% |
| 150 $^0$C-annealed | 2.32 | 0.53 | 0.44 | 0.53% |

The critical parameters of $DBSQ(OH)_2$ solar cell devices are listed in table 6.1. The un-annealed devices have the highest average efficiency of 1.09% (with maximum efficiency of 1.21%). For the devices annealed at 80 $^0$C, the efficiency decreases to 0.80%. The dropped efficiency is mainly caused by the $J_{SC}$ decreasing from 4.6 mA cm$^{-2}$ to 3.3 mA cm$^{-2}$. For the devices annealed at 120 $^0$C, the $J_{SC}$ is recovered back to 4.26 mA cm$^{-2}$ but still lower than the un-annealed devices, and the $V_{OC}$ dropped from 0.69 V to 0.57 V, resulting in an slight increase in overall PCE to 0.88%. The efficiency of the 150 $^0$C-annealed devices have dropped to 0.53% with

both decreased $J_{SC}$ and $V_{OC}$. The FFs increased from 33% (for the un-annealed devices) to 44% (for the 150 $^0$C-annealed devices) after annealing.

The open-circuit voltage reflects the HOMO(D)-LUMO(A) offset at the donor acceptor interface. From the un-annealed devices to the 80 $^0$C-annealed devices, the open-circuit voltage remains the same, suggesting that there is little change in energetics at the heterojunction interface between SQ and PCBM. In turn, the decreased $V_{OC}$ from the 80 $^0$C-annealed to the 120 $^0$C-annealed devices might imply a change of energetics at the interface. The reason for decrease in $V_{OC}$ is interpreted to be resulted from the aggregation which causes an increase in the HOMO energy level for the SQ. This can be understood through a molecular orbital hybridization description as shown in Figure 6.2 below.

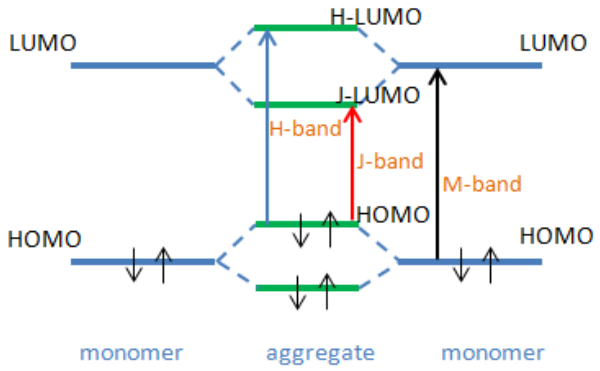


**Figure 0.2** Energetic diagram of SQ monomer and aggregate explained by molecular orbital hybridization theory.

From the simple energetic diagram showed in Figure 6.2, we can see that the HOMO energy level increases in the SQ aggregate because of the splitting that takes place upon overlap of orbitals on adjacent molecules. From the inset spectrum of Figure 6.1, we know that $DBSQ(OH)_2$ has aggregated under the 80 $^0$C-annealing, which means that the aggregates already exist in the 80 $^0$C-annealed devices. However, the devices did not show a reduced $V_{OC}$, as explained by Figure

6.2. This is unexpected and the possible explanation will be proposed below based on both J-V curves and EQE spectra.

The fill factor is a broad measure of active layer morphology. The higher the crystallinity, the better the exciton diffusion and charge transport properties of the active layer. The recombination is thus reduced and a higher fill factor is obtained. From the inset with absorption spectra, we know that the SQs aggregate under annealing, and we believe the morphology of the devices is improved because SQ aggregates are observed in crystalline or semi-crystalline regions whereas SQ monomers are seen in amorphous regions. The increased FFs confirm our assumption, with the FF of the 150 $^0$C-annealed devices being enhanced to 44%. However, the overall efficiency is reduced to only 0.53% due to the decrease in $J_{SC}$ and $V_{OC}$. This may be caused by the significant reduced interfacial area as the active layer materials phase separate. In this way, the aggregate domains become larger than exciton diffusion length.

The change in $J_{SC}$ during annealing is interesting, since it decreases first to 3.30 mA cm$^{-2}$ after 80 $^0$C-annealing, and then increases to 4.26 mA cm$^{-2}$ for the 120 $^0$C-annealed devices. The $J_{SC}$ is sensitive to the active layer morphology, absorbance of the materials, excited state lifetime, and the energetics at the interface, etc. Therefore, we use spectral response (or external quantum efficiency) results to help explain the device behavior.

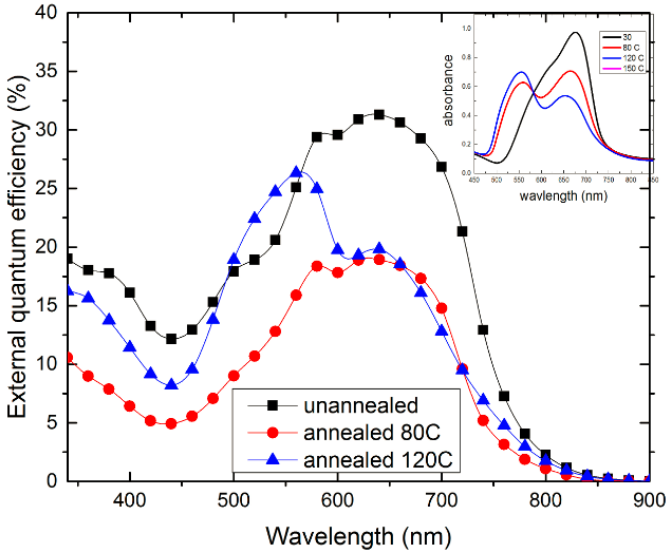


**Figure 0.3** External quantum efficiency of $DBSQ(OH)_2$:PCBM (1:1 w/w) devices with no annealing treatment (black), 80 $^0$C-annealing (red), and 120 $^0$C-annealing treatment (blue).

The external quantum efficiency spectra for $DBSQ(OH)_2$:PCBM devices are shown along with the absorption spectra (inset). The EQE spectrum for un-annealed devices matches well with the corresponding absorption spectrum with a maximum of 32% at 660 nm (absorption maximum is at 675 nm). The EQE spectrum for the 80 $^0$C-annealed devices shows a similar shape as the un-annealed devices but at a lower value (with a maximum at 660 nm). For the 120 $^0$C-annealed devices, the EQE spectrum changes with a new peak at 570 nm.

The experimental set up of EQE is introduced in section 2.4 in Chapter 2. The light was selected before incidence on the device, and the EQE signals (i.e. free carriers) only come from the light (or photons) that can be absorbed by the material. By changing the absorbance of the SQ material (such as by introducing aggregates in the active layer through thermal annealing), we theoretically change the spectral response of the device. Therefore, we would expect the EQE spectrum to be consistent with the absorption of the donor acceptor material blends. Indeed, the EQE spectrum of the un-annealed devices (corresponding to the SQ monomer as an absorber) and the 120 $^0$C-annealed devices (corresponding to the SQ H-aggregate as an absorber) obey this rule,

but the 80 $^0$C-annealed devices do not. If we believe that the SQ monomer is the main absorber in the un-annealed devices, the similar black and the red EQE spectra suggest that the main absorber in the 80 $^0$C-annealed devices is still SQ monomer. This conclusion conflicts with the absorption spectrum of the 80 $^0$C-annealed blend films, which indicate a considerable amount of H-aggregate formed in the films.

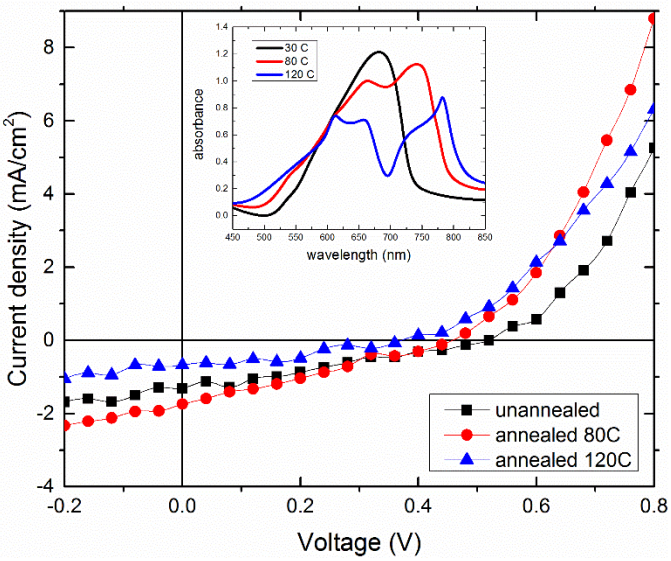


**Figure 0.4** Summarized J-V curve measurement for DBSQ:PCBM (1:1 w/w) devices. Inset: absorption spectra of DBSQ:PCBM (1:1 w/w) blend films annealed at 80 $^0$C and 120 $^0$C. Inset: absorption spectrum of annealed blend films.

The J-V characters of DBSQ:PCBM (1:1 w/w) devices are shown in Figure 6.3, along with the absorption spectra under different thermal treatments. More detailed parameters of the OPV devices are listed in table 6.2 below.

**Table 0.2** Important device parameters of DBSQ:PCBM (1:1 w/w) OPV devices before and after thermal treatments. The J-V measurement for 150 $^0$C-annealed DBSQ:PCBM devices are unsuccessful, and is not provided here.

| Thermal treatment | $J_{sc}$/mA cm-$^2$ | $V_{oc}$/V | FF | η |
|---|---|---|---|---|
| Un-annealed | 1.37 | 0.51 | 0.45 | 0.23% |
| 80 $^0$C-annealed | 1.89 | 0.45 | 0.28 | 0.22% |
| 120 $^0$C-annealed | 0.62 | 0.38 | 0.42 | 0.11% |

From table 6.2, we know that the efficiency of DBSQ:PCBM devices are much lower than $DBSQ(OH)_2$. The un-annealed devices only have 0.23% efficiency. The low efficiency is due to the low short-circuit current (only 1.37 mA cm$^{-2}$) and the low open-circuit voltage (only 0.51 V). After annealing, the $J_{SC}$ increased to 1.89 mA cm-2 (at 80 $^0$C) and then further decreased to 0.62 mA cm$^{-2}$ (at 120 $^0$C). The $V_{OC}$ continuously decreased to 0.38 V upon annealing leading to a device efficiency of only 0.11%. The 150 $^0$C-annealed devices have even lower efficiencies and were hard to measure, and thus will not be provided.

The efficiency of the DBSQ:PCBM devices are lower than that of the $DBSQ(OH)_2$ based devices. However, the trend upon thermal treatment is similar; the device efficiency drops after annealing. This indicates that the thermal annealing might not be an effective way to improve the performance of the OPV devices, based on these two SQs. It is very odd that the improved $J_{SC}$ and the decrease in fill factor happened at the same time in the 80 $^0$C-annealed devices.

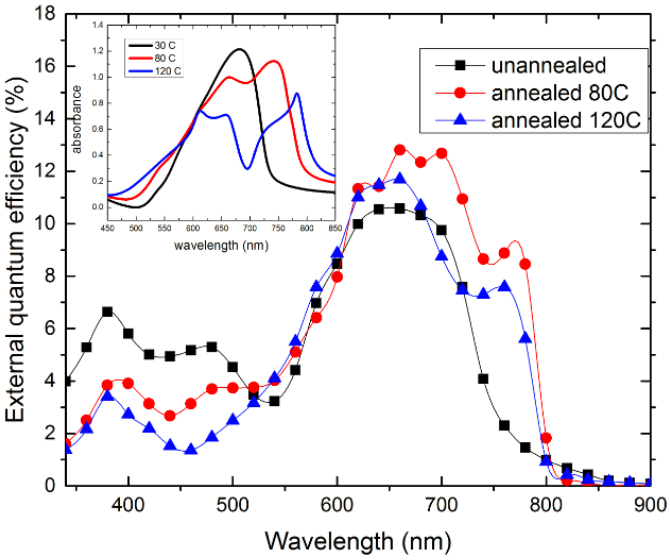


**Figure 0.5** External quantum efficiency of DBSQ:PCBM (1:1 w/w) devices with no annealing treatment (black), 80 $^0$C-annealing (red), and 120 $^0$C-annealing treatment (blue). Inset: absorption spectrum of annealed blend films.

The external quantum efficiency spectra of DBSQ:PCBM devices are shown in Figure 6.5. In this case, the EQE changes immediately after 80 $^0$C annealing. A shoulder at 770 nm is observed in the EQE spectra of 80 $^0$C and 120 $^0$C annealed devices. This shoulder represents that the J-aggregate, as an absorber in active layer, starts to contribute to the photo-charge generation in the 80 $^0$C and 120 $^0$C annealed devices. In 80 $^0$C annealed devices, we clearly see five characteristic peaks at 560 nm (shoulder), 620 nm, 660 nm, 700 nm and 770 nm, corresponding to the absorption features at 550nm (shoulder), 613 nm, 658 nm, 740 nm and 786 nm in SQ:PCBM blend films.

## 6.4 Summary

When comparing the photovoltaic efficiencies of these two SQ-based OPV devices, we can clearly see a better performance for the DBSQ(OH)$_2$ devices. In order to interpret this result and make a comprehensive comparison between these two materials, we need to look at the equation 1.1 for OPV efficiency as introduced in section 1.1.3 in chapter 1:

$$\eta_{OPV} = \eta_{Abs} \cdot \eta_{ED} \cdot \eta_{E-H} \cdot \eta_{CT} \cdot \eta_{CC}$$

From Figure 4.9 (section 4.3.3, chapter 4), we note that the absorption spectra of SQ:PCBM blend films (as-cast) are very similar to each other for these two SQs. This suggests that the $\boldsymbol{\eta_{Abs}}$ terms are similar for both DBSQ and DBSQ(OH)$_2$ un-annealed devices. In these devices, the SQs are mainly in the monomer form. The morphology of the active layer can be regarded as amorphous and there is no phase separation between SQ and PCBM. Therefore, the $\boldsymbol{\eta_{CT}}$ terms for these two types of SQ-based devices are similar in value. In both cases, we have ITO as the device anode, PEDOT:PSS as the hole transporting layer, and aluminum as the cathode, so the $\boldsymbol{\eta_{CC}}$ should stay the same for both SQ-based deices. The remaining terms of $\boldsymbol{\eta_{E-H}}$ and $\boldsymbol{\eta_{ED}}$ are then interpreted to be the main reasons for the difference in device performance.

From chapter 3, we know that DBSQ(OH)$_2$ has a similar PLQY as DBSQ, both of which are considered as high values, as compared to other materials such as P3HT.[74,75] Thus, the non-radiative decay rate is small for these two SQ materials. Any limitation on non-radiative coupling between the excited state and ground state will aid in terms of the exciton diffusion length. However, DBSQ(OH)$_2$ exhibits a stronger tendency to crystalize/aggregate than DBSQ in the solid state films. The exciton diffusion rate is proportional to the crystallinity of the material regions where the excited is located at. Therefore, we have reason to believe that the exciton diffusion efficiency in DBSQ(OH)$_2$-based devices is higher than in DBSQ-based devices. In order to address the electron-hole pair separation efficiency ($\boldsymbol{\eta_{E-H}}$), we need to know the HOMO and LUMO energy levels of these SQ, which would drive the next steps in this research.

The device efficiencies of annealed devices are unexpectedly decreased as compared to the un-annealed devices. According to the absorption spectrum of SQ aggregates, we predicted that the SQ aggregates would broaden the spectral response of the device. Indeed, we saw the broadening of the EQE spectra in Figure 6.5 and Figure 6.3. However, the overall power conversion efficiency of the devices decreased after thermal annealing mainly due to the decrease in

open-circuit voltage. We also predicted that SQ aggregates would be observed in crystalline-like domains and SQ monomers in amorphous regions, so we expected a better exciton diffusion and charge transport when SQ aggregates dominate over monomers. Thus, we should see an increase in short-circuit current and fill factor after annealing the device. Indeed, we saw an increase in fill factor upon annealing, indicating a better morphology. However the short-circuit current in annealed $DBSQ(OH)_2$-based devices never exceeds the un-annealed devices. The domain size and the interfacial area may cause this decrease in short circuit current. If the domain size significantly exceeds the exciton diffusion length (typically < 10 nm), the exciton generated in the center of the pure donor or acceptor domain cannot reach the interface, and therefore cannot be converted to free carriers. In addition, the larger the domain size, the smaller the interfacial area, and this is where the exciton dissociation takes place. Therefore, the interfacial area is very important for the photo-induced charge generation process in OPV. However, it's hard to quantify the domain size or the interfacial area in the film, so it's hard to explain the decrease in short-circuit current for annealed devices.

# Chapter 7 CONCLUSIONS AND OUTLOOKS

This thesis has focused on characterizing two SQ materials (i.e. $DBSQ(OH)_2$ and DBSQ) and evaluating their potentials in OPV application. This helps to understand the influence of the hydroxy substituents on the photophysical properties, aggregation behaviors and subsequently photovoltaic performances of aniline-squaraines. The goal of this work (thesis) is to provide a useful relationship between molecular structure and solar cell performance, and thus to help to design new SQ donor materials to improve the device efficiency.

In chapter 3 and chapter 4, two SQ materials, in chloroform solution and as neat films, were characterized. The conclusion was that both $DBSQ(OH)_2$ and DBSQ have similar photophysical properties in solution with the hydroxy groups having a limited impact on the excited states of the individual molecules. However, drastic differences are observed in solid state films; $DBSQ(OH)_2$, possessing hydroxyl groups, forms H-aggregates, while des-hydroxy DBSQ forms predominantly J-aggregates after spin casting. This phenomenon is explained in that the intramolecular H-bonds "lock" the two phenyl moieties in the same plane as the squarylium ring, and thus enhance the planarity and rigidity of the molecular backbone for $DBSQ(OH)_2$. This enhanced planarity favors face-to-face packing, and therefore produces H-aggregates in the condensed solid state. The DBSQ, on the other hand, lacks this molecular rigidity and possesses more rotational freedom of the benzene rings. In this situation, the intermolecular force is dominated by the steric hindrance of the butyl side chains, which prevents the H-aggregate formation and favors head-to-tail packing (i.e. J-aggregates). Therefore, the absorption spectra of two SQs are similar in chloroform solution but significantly different as solid state films. DBSQ, forming J-aggregates in films, extends its absorption further to the near-infrared, while $DBSQ(OH)_2$ has a relatively blue-shifted peak in its film absorption spectrum. From the absorption point of view, aggregation

is considered beneficial for OPV because it broadens the spectral response of SQ materials in devices, and DBSQ J-aggregates perform better than $DBSQ(OH)_2$ H-aggregates due to NIR absorption and a more favorable overlap with a high-photon region of the solar spectrum. It should be noted that besides the absorption, the efficiency of the OPV also depends on many other properties, such as exciton diffusion[76–78] and charge transport[9,13,79].

It is difficult to study the excited state changes upon aggregation because of the non-fluorescent nature of the SQ films. Therefore, in chapter 5, we comprehensively study the SQ aggregation process in PMMA solid solutions and in THF/H2O mixtures. In PMMA solid solutions, we have observed the spectral broadening due to intermolecular interactions of SQ monomers with random dipole orientations. In subsequent annealing studies, we have monitored the population change from monomers to aggregates, which is accompanied by a decrease in fluorescence quantum yield. This self-quenching phenomenon is confirmed by the fluorescence lifetime measurements made through a time correlated single photon counting (TCSPC) setup. The fluorescence lifetime decreases from 1.1 ns to 0.3 ns as the weight ratio of SQ in PMMA solid solution increases from 0.25 % to 2%. This decrease in fluorescence lifetime may reflect the excited state lifetime, and thus would be detrimental to the exciton diffusion length and the solar cell performance. In solutions, we successfully tune the population of SQ monomers and aggregates by changing the solvent quality in THF/H2O solvent mixtures. The results show that the double "humps" in absorption spectra of $DBSQ(OH)_2$ films originate from the same aggregate species. We assign this species as the Davydov aggregates with an oblique transition dipole alignment. The well-defined absorption spectra of $DBSQ(OH)_2$ Davydov aggregates may suggest a high extent of crystalline order. This is consistent with the strong intermolecular interaction due to a more planar and rigid molecular backbone.

In chapter 6, we used these two SQ donors in OPV devices with PCBM as the acceptor material. Spin casting was used to make uniform, thin organic films with a SQ:PCBM bulk heterojunction structure. The comparison of the efficiencies of the devices can be separated into two aspects. For un-annealed devices, $DBSQ(OH)_2$ clearly outperformed DBSQ with higher short circuit current (4.57 mA $cm^{-2}$ compares to 1.37 mA $cm^{-2}$) and open circuit voltage (0.69 V compares to 0.51 V). This may due to the higher crystalline order of $DBSQ(OH)_2$ (than DBSQ), leading to a larger exciton diffusion length, and a better charge transport property. For annealed devices, the efficiency drops for both SQs-based solar cells. This is counterintuitive to our expectation because aggregates are considered to exist in crystalline or semi-crystalline domains while monomers exist in amorphous domains. Therefore, the increase in aggregate population was expected to improve the crystallinity of the active layer, and thus improve the solar cell performance. One explanation consistent with the observation is that the annealing induces a large extent of phase separation and reduces the interfacial area between SQ and PCBM. The domain size exceeds the exciton diffusion length after annealing. As a result, the charge dissociation yield decreases significantly, leading to energy losses in the active layer. Further investigations will be carried out to evaluate the phase separation and thus to build upon the work described in this thesis.

# REFERENCES


1. Bastasch, M. CBO: Most energy tax subsidies go toward green energy, energy efficiency. *The Daily Caller* (2013). at <http://dailycaller.com/2013/03/14/cbo-most-energy-tax-subsidies-go-toward-green-energy-energy-efficiency/>
2. Agency, I. E. World Energy Outlook 2004. (2004).
3. Ohl, R. S. Light-sensitive electric device. (1946). at <http://www.google.com/patents/US2402662>
4. Darling, S. B. & You, F. The case for organic photovoltaics. *RSC Adv.* **3,** 17633–17648 (2013).
5. Smestad, G. P. *et al.* Reporting solar cell efficiencies in Solar Energy Materials and Solar Cells. *Sol. Energy Mater. Sol. Cells* **92,** 371–373 (2008).
6. Gupta, V. *et al.* Barium: An Efficient Cathode Layer for Bulk-heterojunction Solar Cells. *Sci Rep* **3,** (2013).
7. Wang, X. *et al.* Highly efficient unsymmetrical squaraines for panchromatic dye-sensitized solar cells: A computational study. *RSC Adv.* **3,** 5227–5237 (2013).
8. Dennler, G., Scharber, M. C. & Brabec, C. J. Polymer-fullerene bulk-heterojunction solar cells. *Adv. Mater. Weinh. Ger.* **21,** 1323–1338 (2009).
9. Günes, S., Neugebauer, H. & Sariciftci, N. S. Conjugated Polymer-Based Organic Solar Cells. *Chem. Rev.* **107,** 1324–1338 (2007).
10. Xu, Z. *et al.* Vertical Phase Separation in Poly(3-hexylthiophene): Fullerene Derivative Blends and its Advantage for Inverted Structure Solar Cells. *Adv. Funct. Mater.* **19,** 1227–1234 (2009).
11. Wudl, F. The chemical properties of buckminsterfullerene (C60) and the birth and infancy of fulleroids. *Acc. Chem. Res.* **25,** 157–161 (1992).
12. Allemand, P. M. *et al.* Two different fullerenes have the same cyclic voltammetry. *J. Am. Chem. Soc.* **113,** 1050–1051 (1991).
13. Li, G. *et al.* High-efficiency solution processable polymer photovoltaic cells by self-organization of polymer blends. *Nat. Mater.* **4,** 864–868 (2005).
14. Jamieson, F. C. *et al.* Fullerene crystallisation as a key driver of charge separation in polymer/fullerene bulk heterojunction solar cells. *Chem. Sci.* **3,** 485–492 (2012).
15. Shaheen, S. E. *et al.* 2.5% efficient organic plastic solar cells. *Appl. Phys. Lett.* **78,** 841–843 (2001).

16. Park, S. H. *et al.* Bulk heterojunction solar cells with internal quantum efficiency approaching 100%. *Nat Photon* **3,** 297–302 (2009).
17. He, Z. *et al.* Simultaneous Enhancement of Open-Circuit Voltage, Short-Circuit Current Density, and Fill Factor in Polymer Solar Cells. *Adv. Mater.* **23,** 4636–4643 (2011).
18. Bruck, S. *et al.* Structure-property relationship of anilino-squaraines in organic solar cells. *Phys. Chem. Chem. Phys.* **16,** 1067–1077 (2014).
19. Chen, G. *et al.* Solution-processed organic photovoltaic cells based on a squaraine dye. *Phys. Chem. Chem. Phys.* **14,** 14661–14666 (2012).
20. Chen, G. *et al.* A Series of Squaraine Dyes: Effects of Side Chain and the Number of Hydroxyl Groups on Material Properties and Photovoltaic Performance. *Chem. Mater.* **26,** 1356–1364 (2014).
21. Cho, Y. J., Lee, J. Y., Chin, B. D. & Forrest, S. R. Polymer bulk heterojunction photovoltaics employing a squaraine donor additive. *Org. Electron.* **14,** 1081–1085 (2013).
22. Deing, K. C., Mayerhoffer, U., Wurthner, F. & Meerholz, K. Aggregation-dependent photovoltaic properties of squaraine/PC61BM bulk heterojunctions. *Phys. Chem. Chem. Phys.* **14,** 8328–8334 (2012).
23. Silvestri, F. *et al.* Efficient Squaraine-Based Solution Processable Bulk-Heterojunction Solar Cells. *J. Am. Chem. Soc.* **130,** 17640–17641 (2008).
24. Walker, B. *et al.* Nanoscale Phase Separation and High Photovoltaic Efficiency in Solution-Processed, Small-Molecule Bulk Heterojunction Solar Cells. *Adv. Funct. Mater.* **19,** 3063–3069 (2009).
25. Bronstein, H. A. & Luscombe, C. K. Externally Initiated Regioregular P3HT with Controlled Molecular Weight and Narrow Polydispersity. *J. Am. Chem. Soc.* **131,** 12894–12895 (2009).
26. Panzer, F., Bässler, H., Lohwasser, R., Thelakkat, M. & Köhler, A. The Impact of Polydispersity and Molecular Weight on the Order–Disorder Transition in Poly(3-hexylthiophene). *J. Phys. Chem. Lett.* **5,** 2742–2747 (2014).
27. Peumans, P., Yakimov, A. & Forrest, S. R. Small molecular weight organic thin-film photodetectors and solar cells. *J. Appl. Phys.* **93,** 3693–3723 (2003).
28. Peumans, P., Uchida, S. & Forrest, S. R. Efficient bulk heterojunction photovoltaic cells using small-molecular-weight organic thin films. *Nature* **425,** 158–162 (2003).
29. Sun, Y. *et al.* Solution-processed small-molecule solar cells with 6.7% efficiency. *Nat. Mater.* **11,** 44–48 (2012).
30. Zhang, Q. *et al.* Small-molecule solar cells with efficiency over 9%. *Nat. Photonics* **9,** 35–41 (2015).

31. Wong, C. Y., Cotts, B. L., Wu, H. & Ginsberg, N. S. Exciton dynamics reveal aggregates with intermolecular order at hidden interfaces in solution-cast organic semiconducting films. *Nat. Commun.* **6,** 5946 (2015).
32. Marcus, R. A. Electron transfer reactions in chemistry. Theory and experiment. *Rev. Mod. Phys.* **65,** 599–610 (1993).
33. Huang, J.-S. *et al.* Polymer bulk heterojunction solar cells employing Forster resonance energy transfer. *Nat Photon* **7,** 479–485 (2013).
34. Zheng, J. Spectroscopy-based quantitative fluorescence resonance energy transfer analysis. *Methods Mol. Biol. Clifton NJ* **337,** 65–77 (2006).
35. Shockley, W. & Queisser, H. J. Detailed Balance Limit of Efficiency of p-n Junction Solar Cells. *J. Appl. Phys.* **32,** 510–519 (1961).
36. Servaites, J. D., Ratner, M. A. & Marks, T. J. Practical efficiency limits in organic photovoltaic cells: Functional dependence of fill factor and external quantum efficiency. *Appl. Phys. Lett.* **95,** 163302 (2009).
37. Servaites, J. D., Yeganeh, S., Marks, T. J. & Ratner, M. A. Efficiency Enhancement in Organic Photovoltaic Cells: Consequences of Optimizing Series Resistance. *Adv. Funct. Mater.* **20,** 97–104 (2010).
38. Godovsky, D. Modeling the ultimate efficiency of polymer solar cell using Marcus theory of electron transfer. *Org. Electron.* **12,** 190–194 (2011).
39. Koster, L. J. A., Mihailetchi, V. D. & Blom, P. W. M. Ultimate efficiency of polymer/fullerene bulk heterojunction solar cells. *Appl. Phys. Lett.* **88,** 093511 (2006).
40. Research Cell Efficiency Records (http://www.nrel.gov/ncpv/images/efficiency_chart.jpg).
41. Fermi, E. *Nuclear Physics. University of Chicago Press.*
42. Nau, W. Modern Molecular Photochemistry of Organic Molecules. by N. J. Turro, V. Ramamurthy, J. C. Scaiano. *ChemPhysChem* **12,** 2496–2497 (2011).
43. Brabec, C. J., Heeney, M., McCulloch, I. & Nelson, J. Influence of blend microstructure on bulk heterojunction organic photovoltaic performance. *Chem. Soc. Rev.* **40,** 1185–1199 (2011).
44. Wei, G., Wang, S., Sun, K., Thompson, M. E. & Forrest, S. R. Solvent-Annealed Crystalline Squaraine: PC70BM (1:6) Solar Cells. *Adv. Energy Mater.* **1,** 184–187 (2011).
45. Salim, T. *et al.* Solvent additives and their effects on blend morphologies of bulk heterojunctions. *J. Mater. Chem.* **21,** 242–250 (2010).
46. Wei, G. *et al.* Efficient, Ordered Bulk Heterojunction Nanocrystalline Solar Cells by Annealing of Ultrathin Squaraine Thin Films. *Nano Lett.* **10,** 3555–3559 (2010).

47. Treibs, A. & Jacob, K. Cyclotrimethine Dyes Derived from Squaric Acid. *Angew. Chem. Int. Ed. Engl.* **4,** 694–694 (1965).
48. Law, K. Y. Squaraine chemistry. A study of the solute-solvent complexation of squaraine in solvents by proton NMR spectroscopy. *J. Phys. Chem.* **93,** 5925–5930 (1989).
49. Park, J. D., Cohen, S. & Lacher, J. R. Hydrolysis Reactions of Halogenated Cyclobutene Ethers: Synthesis of Diketocyclobutenediol. *J. Am. Chem. Soc.* **84,** 2919–2922 (1962).
50. Arunkumar, E., Sudeep, P. K., Kamat, P. V., Noll, B. C. & Smith, B. D. Singlet oxygen generation using iodinated squaraine and squaraine-rotaxane dyes. *New J. Chem. Nouv. J. Chim.* **31,** 677–683 (2007).
51. Tong, X., Wang, N., Slootsky, M., Yu, J. & Forrest, S. R. Intrinsic burn-in efficiency loss of small-molecule organic photovoltaic cells due to exciton-induced trap formation. *Sol. Energy Mater. Sol. Cells* **118,** 116–123 (2013).
52. Dirk, C. W. *et al.* Squarylium Dyes: Structural Factors Pertaining to the Negative Third-Order Nonlinear Optical Response. *J. Am. Chem. Soc.* **117,** 2214–2225 (1995).
53. Gräf, K., Rahim, M. A., Das, S. & Thelakkat, M. Complementary co-sensitization of an aggregating squaraine dye in solid-state dye-sensitized solar cells. *Dyes Pigments* **99,** 1101–1106 (2013).
54. Paek, S. *et al.* Efficient and stable panchromatic squaraine dyes for dye-sensitized solar cells. *Chem. Commun.* **47,** 2874–2876 (2011).
55. Yum, J.-H. *et al.* Efficient Far Red Sensitization of Nanocrystalline TiO2 Films by an Unsymmetrical Squaraine Dye. *J. Am. Chem. Soc.* **129,** 10320–10321 (2007).
56. Law, K.-Y. Squaraine Chemistry. Absorption, Fluorescence Emission, and Photophysics of Unsymmetrical Squaraines. *J. Phys. Chem.* **99,** 9818–9824 (1995).
57. Das, S., Thomas, K. G., Kamat, P. V. & George, M. V. Photosensitizing properties of squaraine dyes. *J. Chem. Sci.* **105,** 513–525 (1993).
58. Shafeekh, K. M., Das, S., Sissa, C. & Painelli, A. Asymmetric Squaraine Dyes: Spectroscopic and Theoretical Investigation. *J. Phys. Chem. B* **117,** 8536–8546 (2013).
59. Terenziani, F., Painelli, A., Katan, C., Charlot, M. & Blanchard-Desce, M. Charge Instability in Quadrupolar Chromophores: Symmetry Breaking and Solvatochromism. *J. Am. Chem. Soc.* **128,** 15742–15755 (2006).
60. Kasha, M., Rawls, H. & El-Bayoumi, A. The exciton model in molecular spectroscopy. *Pure Appl. Chem.* **11,** 371–392 (1965).
61. Spano, F. C. The Spectral Signatures of Frenkel Polarons in H- and J-Aggregates. *Acc. Chem. Res.* **43,** 429–439 (2010).

62. Spano, F. C. Analysis of the UV/Vis and CD Spectral Line Shapes of Carotenoid Assemblies: Spectral Signatures of Chiral H-Aggregates. *J. Am. Chem. Soc.* **131,** 4267–4278 (2009).
63. Emerson, E. S. *et al.* The geometrical structure and absorption spectrum of a cyanine dye aggregate. *J. Phys. Chem.* **71,** 2396–2403 (1967).
64. Zheng, C. *et al.* Contribution of Aggregate States and Energetic Disorder to a Squaraine System Targeted for Organic Photovoltaic Devices. *Langmuir* **31,** 7717–7726 (2015).
65. Tian, M. *et al.* Search for Squaraine Derivatives That Can Be Sublimed without Thermal Decomposition. *J. Phys. Chem. B* **106,** 4370–4376 (2002).
66. HORIBA Jobin Yvon IBH Ltd. A Guide to Recording Fluorescence Quantum Yields.
67. Wahl, M. Time-Correlated Single Photon Counting, PicoQuant GmbH.
68. Scofield, J. H. Frequency-domain description of a lock-in amplifier. *Am. J. Phys.* **62,** 129–133 (1994).
69. S. M. Sze. *Physics of Semiconductor Devices*. at <http://archive.org/details/PhysicsOfSemiconductorDevices>
70. Lakowicz, J. *Principles of Fluorescence Spectroscopy*. (Kluwer Academic/Plenum Publishers, 1999).
71. Larsson, T., Wedborg, M. & Turner, D. Correction of inner-filter effect in fluorescence excitation-emission matrix spectrometry using Raman scatter. *Anal. Chim. Acta* **583,** 357–363 (2007).
72. Hestand, N. J. *et al.* Confirmation of the Origins of Panchromatic Spectra in Squaraine Thin Films Targeted for Organic Photovoltaic Devices. *J. Phys. Chem. C* **119,** 18964–18974 (2015).
73. Chen, G. *et al.* J-aggregation of a squaraine dye and its application in organic photovoltaic cells. *J. Mater. Chem. C* **1,** 6547–6552 (2013).
74. Ferreira, B., da Silva, P. F., Seixas de Melo, J. S., Pina, J. & Maçanita, A. Excited-State Dynamics and Self-Organization of Poly(3-hexylthiophene) (P3HT) in Solution and Thin Films. *J. Phys. Chem. B* **116,** 2347–2355 (2012).
75. Cook, S., Furube, A. & Katoh, R. Analysis of the excited states of regioregular polythiophene P3HT. *Energy Environ. Sci.* **1,** 294–299 (2008).
76. Wei, G., Wang, S., Renshaw, K., Thompson, M. E. & Forrest, S. R. Solution-Processed Squaraine Bulk Heterojunction Photovoltaic Cells. *ACS Nano* **4,** 1927–1934 (2010).
77. Mikhnenko, O. V., Blom, P. W. M. & Nguyen, T.-Q. Exciton diffusion in organic semiconductors. *Energy Environ. Sci.* **8,** 1867–1888 (2015).

78. Menke, S. M. & Holmes, R. J. Exciton diffusion in organic photovoltaic cells. *Energy Environ. Sci.* **7,** 499–512 (2014).
79. Clarke, T. M. & Durrant, J. R. Charge Photogeneration in Organic Solar Cells. *Chem. Rev.* **110,** 6736–6767 (2010).

# Appendix A Standard operation procedures for device making

**Prepare ITO glass substrates and donor acceptor mix**

1) **Clean ITO substrates using acetone.** Place 9-10 slides into the acetone solution, and make sure that the solvent is CLEAN (no visual residues suspended in the bottom). The ITO slides must no longer be touched by fingers or gloves once they enter the acetone. Make sure the sonicator is set to 20 minutes with no heat at a power level of 9. At this point, check to make sure the water is at the correct level in the sonication bath (the indents in the corners toward the top). Once the sonicator is turned on, adjust the positioning of the jar until you see bubbles suspended in solution coming off of the ITO slides. This means that the cavitation effect used to clean the slides is functioning properly.
2) **Clean vials.** Obtain 4 glass vials for the PEDOT:PSS solution, active layer solution, DI water and pure CHCl3. Rinse each vial by shaking with the CHCl3. This removes any residue left in the bottom of the vial from the manufacturing processes. One rinsed, dry each vial using clean air gun, and put them into the vacuum oven for 5 minutes at temperature setting 7 to evaporate off any residual solvent, sans caps, and cool for 3 minutes afterwards. Label them.

   Find out the squaraine materials that you are going to use. Squaraine and PCBM materials are stored in the glove box. Set them ready for step 4.
3) **Further clean ITO substrates using IPA.** When the sonication in acetone solution finished, remove the slides from the acetone one at a time, and set them onto one smaller kimwipes, folded over, and scrub both sides of each slide with kimwipes. Blow off the

lint using clean air gun. Then, put them into IPA solution bottle, make sure the IPA solution is CLEAN. Sonicate them with the same specifications as with the acetone sonication.

4) **Prepare SQ:PCBM solution.** While this is sonicating, prepare your active layer solution. Make sure the balance is calibrated. Weigh out X mg SQ and X mg PCBM into the cleaned vials, add necessary amount of CHCl3. Parafilm the bottle and sonicate for 5 min.
5) **Tape the slides.** By this point, the glass slides with the ITO substrate should be finished sonicating in the IPA. Take them out one by one and scrub each one like you did in step 4 with kimwipes. Blow off excess lint. Place them onto large kimwipes. Use a multimeter (set to "Ω") to determine which side is coated with ITO (the resistance of ITO side is about 15-20 Ω; the resistance of glass is unreadable). Affix a thin strip of Kapton tape onto the ITO side of the substrate, as the red rectangular shown in the Figure below. This tape will be teared down when testing the devices to expose the ITO contact.

6) **Put SQ:PCBM solution into glovebox.** Once finished the sonication of SQ:PCBM blend solution, move the bottle into glovebox for spin casting.
7) **Bake the substrates.** Blow off the lint after taped the substrates. Place the taped substrates on a larger thick glass plate, which has been cleaned and wiped down, blown off until clean. Move the plate with the slides on it into vacuum oven and leave to bake for 10 minutes, to remove any residual solvent.

**Spin coat PEDOT:PSS**

8) **Make PEDOT:PSS solution.** PEDOT:PSS bottle is kept in the small fridge to prevent its aggregation or crystal formation. Obtain a 5mL-syringe and a 0.45um-PTFE filter (if not PTFE, PSS will stick to it), and attach the two. Put about 2.5mL of the PEDOT:PSS solution, and about 2.5mL of de-ionized $H_2O$ into the syringe (use the mark on the syringe to scale). Force the solution through the filter into the clean vial prepared in step 2. Keep this in the fridge until you are ready for spin-coating (PEDOT:PSS is readily to aggregate in room temperature).
9) **Prepare enough film holders.** Use kimwipes wetted by ethanol or isopropanol to clean the inside of the holders, DO NOT use CHCl3 or Acetone (Try it if you don't know why). Dry them with clean air gun. Film holders should be labeled with squaraine name, batch number, film number, date and your name.
10) **Prepare spin-casting PEDOT:PSS.** Take out all the cleaned substrates and set them aside the spin-coater. When spin coating, place ITO substrates on the spin coater, set time to 30 seconds and speed to 5000 rpm. Use a test slide prior to depositing the PEDOT in order to adjust the RPM. Thereafter, take out PEDOT:PSS solution from the fridge.
11) **Spin coating PEDOT:PSS.** To start the PEDOT spin-coating process, turn on the spin-coater and the vacuum pump linked to the spin-coater. Gently place the slide at the center of the spin-coater. Turn on the vacuum (if a hissing sound is produced at this point). Suck up some of the PEDOT:PSS solution into a pipette, and QUICKLY spread it out over the slide, and press start.
    - Suck most of the PEDOT:PSS solution back in the pipette before hit the start button, or PEDOT solution won't be coated evenly.
    - Use new glass pipette every time spin coating PEDOT:PSS (old PEDOT:PSS left in the pipette will aggregate).
    - DO IT AS QUICK AS POSSIBLE

12) **Bake substrates.** Once the spin-coating process has been finished, dry the PEDOT slides in the vacuum oven for 20 minutes.
13) **Transfer substrates into glovebox.** Open and line up the film holders. Open the vacuum oven, and slide the films into their holders. Once the all films have been placed in their cases, take all film holders to entry port of the glove box. The transfer of the PEDOT:PSS from the vacuum oven to the glove box must be finished in minimum of time. This prevents any water or other contaminants from sticking on the films.

**Spin coat SQ:PCBM solution**

14) **Prepare the spin coater.** When working in the glove box, keep in mind rubber gloves must be protected by plastic gloves. Turn on the vacuum pump located under the glovebox. Open the vacuum pump valve inside the glovebox. Turn on the spin coater inside the glove box.
15) **Set up spin coater.** Take out the film holders from the entry port, and line them up. Use test substrates to set the spin coater at 800 rpm for 18 seconds.
16) **Spin coat SQ:PCBM solution.** Use the Pipette in the glove box to suck the SQ:PCBM solution. Set the volume of the pipette for 90 μL. Hold a pipette in one hand and the vial of SQ:PCBM on the other, quickly suck some of the solution into the pipette. Spread the solution over the entirety of the film and immediately press the start button. Cap the bottle immediately after pressed start button to prevent solvent evaporation in the glove box.
17) **Transfer device into second glove box.** When finished, put each slide into film holders. Open the latch of the antechamber, and pull the tray out. Set the films on the tray. Close the latch, and screw down to only hand-tight. Pump-down for 30 minutes, then refill. Clean the first glove box.

**Aluminum deposition**

18) **Install devices.** When devices arrived in the second glove box, find the device holders which are two pieces of steel pads. Place devices one by one into the rectangular gap of one steel pad. Anchor the two using screw spikes with hand. Pay attention on front and back, right and left. Twist tight using back end of the tweezers. The holder can install 8 devices at one time. Once finished one side, tape the edge of this side of the device holder to prevent devices falling off.

19) **Put the device holder into aluminum chamber.** Before open the aluminum chamber, make sure it is pressure over. Open the chamber cap and carefully anchor the device holder onto the inside of chamber cap. Stop rotating when you feel the strength against your hands.

20) **Check the aluminum.** Find the aluminum "boat" in the chamber. Remove the remaining aluminum residue in the "boat" if there is any and place three aluminum patches on it. Close the chamber cap, and clean all the rubbish in the second glove box. Clean the second glove box.

21) **Evacuate chamber.** Press "start" button on the right operational pad. Then the pressure inside the chamber is going down. You can see that the power value is going up as you can hear the turbo sound. The power value will steadily increase to ~98W, and then go back and stay as 8W. The frequency will stay at 1350Hz. Wait for 12 hours.

## Deposit aluminum

22) **Inspect the aluminum chamber.** By the time you come back, the pressure in the aluminum chamber should be $10^{-6}$~$10^{-7}$ torr. Record starting temperature, pressure, current and voltage (should be unchanged 0.2A and 36V) from the right operational pad. Record crystal life from the left operational pad (Next Menu→Sensor Info→Life).

23) **Deposit aluminum.** Make sure the instrument is on "manual" mode. When the recording is done, press "start layer" button on the left operational pad. Increase the power level

"0→1→2→3…→30" by rotating the knob in every 5 seconds. Record "pressure" and "deposition rate" in each power level. Stay 30 seconds in power level of 30, then return back to 5 second in each power level of "31→32…→47". "47" is enough for aluminum evaporation. The maximum power level is "55". When it reached 47, stay at 47 until the end of the deposition process. The system will automatically shut down and pressure inside the chamber will return back to ambient level.

24) **Take out devices.** Wait around 10 minutes and the right operational pad displays "pressure over". Prepare the film holders, line them up. Open the chamber and take off the device holder. Carefully take off the tape and use tweezers transport device into its corresponding film holder one by one. <u>When the transportation is finished, put everything where it originally belongs and take out the rubbish (tapes and gloves).</u>

# Appendix B Peak fitting for PMMA film absorptions

Here we have the detailed peak fitting results for $DBSQ(OH)_2$ in PMMA solid solution. The black curve is the original absorption spectrum; the green curve is the Gaussian function that used to fit the original peak; the red curve is the sum of the Gaussian functions as a comparison to original absorption spectrum. The baseline method for these fitting is End Points Weighted Baseline. The R-Square for all peak-fittings are all above 0.995.

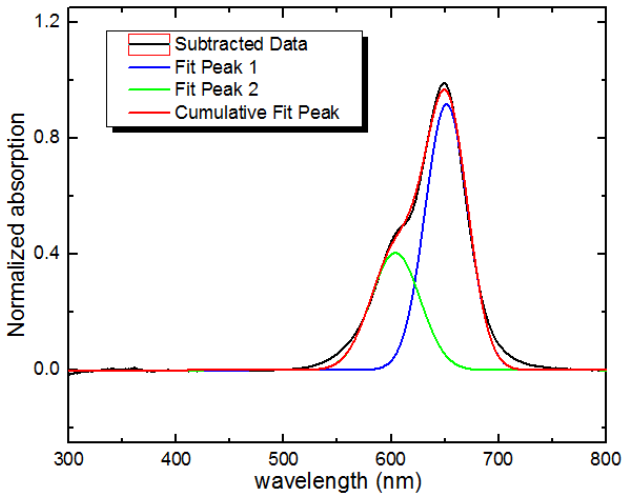


Fitting Results

| Peak Index | Peak Type | Area Intg | FWHM | Max Height |
|---|---|---|---|---|
| 1. | Gaussian | 45.66053 | 46.74728 | 0.9176 |
| 2. | Gaussian | 23.33967 | 54.15 | 0.40492 |

**Figure B.1** Peak fitting results for $DBSQ(OH)_2$ absorption in 5% (SQ/(SQ+PMMA) by weight) PMMA films.

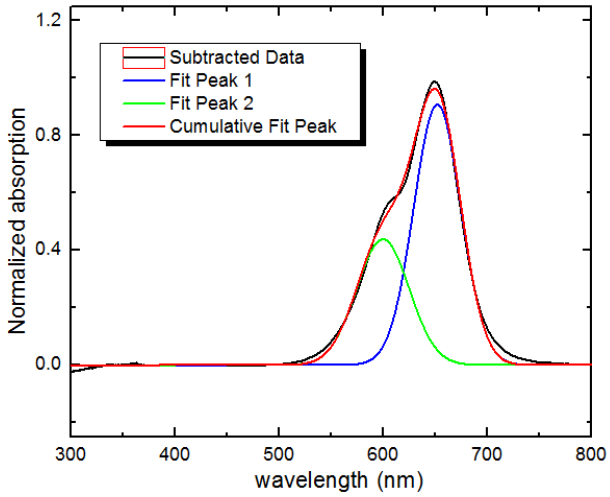


**Fitting Results**

| Peak Index | Peak Type | Area Intg | FWHM | Max Height |
|---|---|---|---|---|
| 1. | Gaussian | 51.5346 | 53.40496 | 0.90654 |
| 2. | Gaussian | 27.72516 | 59.43382 | 0.43824 |

**Figure B.2** Peak fitting results for DBSQ(OH)$_2$ absorption in 7.5% (SQ/(SQ+PMMA) by weight) PMMA films.

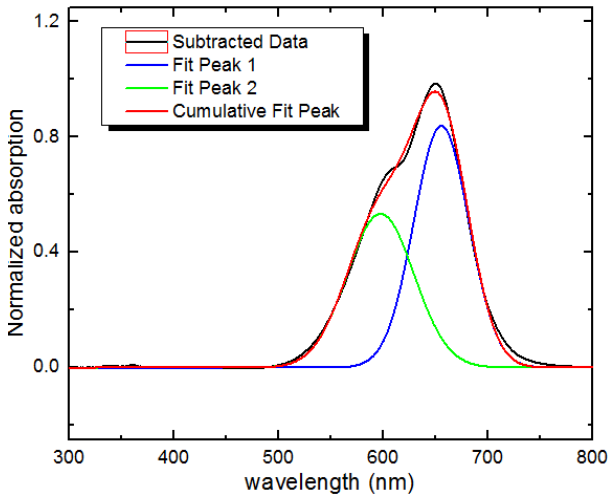


**Fitting Results**

| Peak Index | Peak Type | Area Intg | FWHM | Max Height |
|---|---|---|---|---|
| 1. | Gaussian | 55.20431 | 61.88567 | 0.83801 |
| 2. | Gaussian | 42.67644 | 75.17648 | 0.5333 |

**Figure B.3** Peak fitting results for DBSQ(OH)$_2$ absorption in 15% (SQ/(SQ+PMMA) by weight) PMMA films.

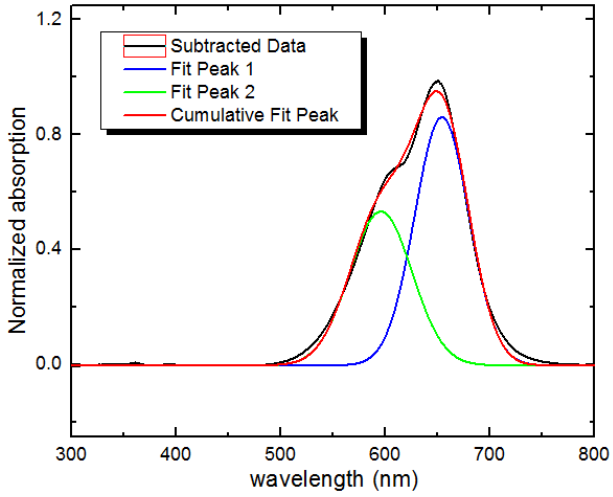


**Fitting Results**

| Peak Index | Peak Type | Area Intg | FWHM | Max Height |
|---|---|---|---|---|
| 1. | Gaussian | 52.50474 | 59.79951 | 0.82484 |
| 2. | Gaussian | 43.24978 | 75.59079 | 0.53751 |

**Figure B.4** Peak fitting results for DBSQ(OH)$_2$ absorption in 22.5% (SQ/(SQ+PMMA) by weight) PMMA films.

# Appendix C List of Publications and Conference Presentations

## PUBLICATIONS

1. Chenyu Zheng, Anirudh Raju Penmetcha, Brandon Cona, Susan D. Spencer, Bi Zhu, Patrick Heaphy, Jeremy A. Cody, and Christopher J. Collison, *Contribution of Aggregate States and Energetic Disorder to a Squaraine System Targeted for Organic Photovoltaic Devices*, **Langmuir 2015** 31 (28), 7717-7726, DOI: 10.1021/acs.langmuir.5b01045
2. Anirudh R. Penmetcha, Chenyu Zheng and Christopher J. Collison. Water Based Inkjet Material Deposition of Donor-Acceptor Nanocomposites for Usage in Organic Photovoltaics. **MRS Proceedings** (**2015**), (1761), DOI:10.1557/opl.2015.681.

## CONFERENCE PRESENTATIONS

1. Chenyu Zheng, Susan Spencer, Brad Conrad, Jeremy A. Cody and Christopher J. Collison, *Self-Assembling Squaraine Aggregates' Impact on Photovoltaic Performance*, **55th Electronic Materials Conference (2013)**, University of Notre Dame, South Bend, IN.
2. Chenyu Zheng, Guy Wolfe, Victor Murcia, Susan Spencer and Cristopher J. Collison, *Chemical Modification of Squaraines and their Photophysical Properties Targeted for Mechanistic Study of Organic Photovoltaics*, **MRS 2013 Fall meeting**, Symposium Y: Joint Poster Session: Physics of OPV, Boston, MA.
3. Guy Wolfe, Chenyu Zheng, Victor Murcia, Susan Spencer, Jeremy A. Cody and Christopher J. Collison, *Use of Photophysical Properties of Novel Squaraines to Screen for Their Viability in Organic Solar Cells*, **MRS 2013 Fall meeting**, Symposium Y: Joint Poster Session: Physics of OPV, Boston, MA.

4. Chenyu Zheng, Nicholas Hestand, Anirudh Raju Penmetcha, Jeremy A. Cody, Frank Spano and Christopher J. Collison, *Relating Molecular Structure to Squaraine Aggregation and Device Performance through Optoelectronic Experiment and Theory*, **MRS 2014 Fall meeting**, Symposium U: Organic Photovoltaics – Fundamentals, Materials and Devices, Boston, MA.
5. Christopher J. Collison, Susan Spencer, Chenyu Zheng, Jeremy A. Cody, Nicholas Hestand and Frank Spano, *Predictive Modeling of Excited States in Squaraine Crystals and Their Effect on Exciton Dissociation Rate at Bulk Heterojunction Interface*. **MRS 2014 Fall meeting**, Symposium U: Organic Photovoltaics – Fundamentals, Materials and Devices, Boston, MA.
6. Patrick Cost, Chenyu Zheng, Guy Wolfe, Darina Vassileva Jeremy A. Cody and Christopher Collison, *Synthesis and Characterization of Novel Squaraines Targeted for Organic Photovoltaic Devices*. **MRS 2014 Fall meeting**, Symposium Q: Fundamentals of Organic Semiconductors – Synthesis, Morphology, Devices and Theory, Boston, MA.
7. Anirudh Raju Penmetcha, Chenyu Zheng, James Sinka, Brandon Cona, Jeremy A. Cody and Christopher J Collison, *H- and J-Aggregates and Their Photophysical Properties of Squaraine Donor Materials*. Symposium A: Embedded Nanoparticles and Rare-earth Materials in III-V Semiconductors, **57th Electronic Materials Conference (2015)**, Columbus, OH.
8. Brandon Cona, Anirudh Raju, Chenyu Zheng, Patrick Cost, Patrick Heaphy, Jeremy A. Cody and Christopher J. Collison, *Comprehensive Study of the Effect of Functionalization on the Aggregation Properties of Squaraines Targeted for Organic Photovoltaic Devices*, **57th Electronic Materials Conference (2015)**, Columbus, OH.
9. Chenyu Zheng, Anirudh Raju, Brandon Cona, Susan Spencer, James Sinka, Jeremy A. Cody, and Christopher J. Collison, *Correlation between Panchromaticity and Power Conversion Efficiencies in Small Molecule Organic Photovoltaic Devices.* Symposium R: Organic and Hybrid Photovoltaics, **57th Electronic Materials Conference (2015)**, Columbus, OH.

10. Christopher J. Collison, Nicholas Hestand, Chenyu Zheng, Anirudh Raju, Brandon Cona, Jeremy A. Cody and Frank Spano, *Modeling and Assignment of Intermolecular Charge Transfer States in Squaraines and Their Impact on Charge Generation in Bulk Heterojunction Solar Cells*, **57th Electronic Materials Conference (2015)**, Columbus, OH.
11. Christopher J. Collison, Chenyu Zheng, Nicholas Hestand, Brandon Cona, Anirudh Raju Penmetcha, Susan Spencer, Jeremy Cody and Frank Spano. *Theory and assignment of intermolecular charge transfer states in squaraines and their impact on efficiency in bulk heterojunction solar cells*. **SPIE Organic Photonics+ Electronics** (pp. 95670R-95670R), August 2015, San Diego, CA.